Dynamics of Time-Varying and Nonlinear Phononic Lattices

Thesis by
Brian Lee Kiwon Kim

In Partial Fulfillment of the Requirements for the
Degree of
Doctor of Philosophy in Mechanical Engineering

CALIFORNIA INSTITUTE OF TECHNOLOGY
Pasadena, California

2023
Defended March 1, 2023

Brian Lee Kiwon Kim
ORCID: 0000-0002-2403-8703

ACKNOWLEDGEMENTS

First, I would like to thank my advisor, Prof. Chiara Daraio. Her guidance over the last four years helped me navigate the long, circuitous path through deceptively complex problems that led us to places we did not expect. The astonishing diversity of ideas and projects she can cultivate and manage makes for the most eclectic and interesting research group of which I have ever had the pleasure of being a member. Thanks to her, the Wild West of bench space and disappearing 3/16" hex keys in the sub-basement is always full of exciting ideas and creative, curious people.

Equally, I must thank Prof. Christopher Chong from Bowdoin College, for becoming like a second advisor to me in the last few years. We would be lost without his deep understanding of mathematical physics and analytical thinking. He has been gracious through countless video calls and is an excellent teacher with the intuition (and patience) to let me learn by working through problems that he could probably solve in his sleep. I can never thank him enough for his mentorship, and I hope I can visit him soon in person in beautiful Maine.

I thank my thesis committee members, Prof. Austin Minnich and Prof. Domniki Asimaki, for serving in this capacity and providing valuable feedback on this thesis. I also thank my undergraduate research advisors, Prof. Scott Bunch and Prof. Keith Brown at Boston University, for introducing me to and starting my career in research.

I am grateful to the many members of the Daraio group who are all always supportive and helpful. I immensely enjoyed working with our Italian visitors and friends, Pietro Maria Santucci and Fabrizio Aloschi, and I look forward to seeing them again in the future. I would especially like to thank Dr. Setare Hajarolasvadi, a truly exceptional scientist and collaborator. It was a pleasure to work alongside her and I look forward to following her career and future work. I also thank Dr. Brittany Kamai for the many wonderful conversations about science and life. Her love for science is second only to her love for her fellow humans, and she has inspired me in many ways.

To all my friends from MCE, thank you for helping me survive the first year and qualifying exams, and, more importantly, we make a damn good softball team.

I also thank the department and research staff, Carolina Oseguera, Lynn Seymour, Jenni Campbell, Sonya Lincoln, Holly Golcher, Mikaela Laite, Stacie Takase, and Petros Arakelian. They are superheroes, and without them, MCE would both figuratively and literally fall apart.

My appreciation for and gratitude to my family is immeasurable. I owe everything to my parents, Ruth and Lee, who, even now, have never stopped working to provide my brother and me with opportunities to succeed and grow. My mom gave us everything and continues to give everything to care for our family. Anything I accomplish also belongs to her. I will never match my dad's work ethic, but I will never stop striving to live up to it because he showed me that the real goal of all that work is to make time to be with family. My brother Andrew has always been an amazing role model, and while I sometimes wonder if my wanting to pursue a PhD was an attempt to outdo him, I know I can always count on him when I need support. I also thank my aunt Jane and my uncle David for being inspirations in pursuing higher academic goals.

Finally, I thank my fiancée, and soon-to-be wife, Lynne Cherchia. My journey through my graduate studies has been our journey, and I am grateful for the support she has provided in so many ways. I am also so proud of the work she is doing in her own studies, and I think her research is far more exciting and impactful than mine. I hope to provide the same support for her, and I can't wait to help complete her journey, and many more, together.

ABSTRACT

The control of waves and vibrations in materials and structures underpins both the most common and the most advanced technologies. Spatially structured and periodic media have been widely studied and applied to signal processing, vibration mitigation, focusing, and other applications beyond the capabilities of bulk materials. Recently, interest has grown in the effects of temporal variation of material and medium properties on wave propagation. Temporal variations serve as an additional dimension for the design and structure of materials, further expanding potential functionalities and performance. Many of the concepts of waves in time-varying media have been developed in photonics and other electromagnetic systems, but the same fundamental dynamics govern acoustic and elastic systems, which provide alternative opportunities for implementation and new applications of time-varying media. In this thesis, we employ a one-dimensional phononic lattice composed of repelling ring magnets with electromagnetic coils that act as time-dependent grounding stiffness. The lattice provides an excellent platform for studying waves in time-varying media, with implementation and modeling of time-variation of elastic properties made simple by its discreteness. In addition, the repelling force between the magnets allows not only for the study of the linear dynamics of time-varying systems for small displacements but also for the exploration of the interaction between time-variation and nonlinear effects. We first present novel demonstrations of two types of time-varying wave phenomena in acoustic or elastic systems. First, the measurement of the propagation of waves across a temporal discontinuity in elastic properties demonstrates the temporal analog to refraction across a spatial boundary. Second, the experimental reconstruction of the dispersion relation of a time-periodic periodic medium shows the opening of wavenumber band gaps. We then characterize the dynamic stability of the time-periodic lattice and consider the role of nonlinearity. Finally, we investigate the possible existence of wavenumber gap breathers, temporally localized solutions of the discrete, nonlinear system.

PUBLISHED CONTENT AND CONTRIBUTIONS

[1] C. Chong, B. L. Kim, E. Wallace, and C. Daraio. Modulation instability and wavenumber gap breathers in a temporally layered lattice. *In preparation*, 2023.
B.L.K. participated in the design of the experiments and numerical simulation, prepared the data, and participated in the preparation of the manuscript.

[2] B. L. Kim, C. Chong, and C. Daraio. Temporal refraction in an acoustic phononic lattice. *In preparation*, 2023.
B.L.K. conceived the project, designed the experiments and numerical simulation, prepared and analyzed the data, and participated in the writing of the manuscript.

[3] B. L. Kim, C. Chong, S. Hajarolasvadi, Y. Wang, and C. Daraio. Dynamics of time-modulated, nonlinear phononic lattices. *Physical Review E*, 107:034211, Mar. 2023. https://doi.org/10.1103/PhysRevE.107.034211
B.L.K. participated in the conception of the project, contributed to the design of experiments, developed the numerical simulation, prepared and analyzed the data, and participated in the writing of the manuscript.

TABLE OF CONTENTS

LIST OF ILLUSTRATIONS

LIST OF TABLES

Chapter 1

INTRODUCTION

The goal of the works presented here is to investigate theoretically and experimentally the dynamics of discrete one-dimensional media with time-varying elastic properties, providing novel demonstrations of time-varying wave phenomena for acoustic waves. We utilize a spring-mass lattice composed of repelling magnets with time-varying grounding stiffnesses to study both wave propagation in and dynamic stability of the lattice for several types of time-variations. Additionally, we investigate the role of nonlinearity in the stability of time-periodic systems.

1.1 Motivation

Waves and vibrations form the foundation of many crucial technologies and fields of study from telecommunications and quantum mechanics to structural health monitoring and medical imaging. Across all these applications, the dynamics of these systems share fundamental similarities, and frequently, the control of waves depends on controlling the speed at which they propagate through or between media. The speed of wave propagation depends first on the properties of the medium (e.g., permeability or bulk modulus) but can secondarily depend on structure and the effective properties thereof. Utility arises from the contrast between two or more materials, and this ultimately underlies the extraordinary or exotic behaviors of structured media, including as forbidden frequency ranges [62], focusing of waves [71], and even breaking reciprocity [88].

The control of propagating waves by structured media, whether electromagnetic, acoustic, or elastic, is conventionally achieved by designing the spatial structure of the medium. Specifically, by varying the speed of propagation of the medium in space, it is possible to achieve a range of functionalities including waveguiding, filtering, or focusing. Fiber optics and other waveguides confine waves by the contrast in refractive index between a core and the surrounding cladding [82]. Photonic or phononic crystals leverage spatially periodic structures at the wavelength scale, such as layers or lattices of alternating propagation speeds, to create and tune frequency band gaps, which are ranges of frequencies that cannot propagate [51, 62]. Such periodic structures themselves may then be used as one of the media in constructing waveguides [49], and graded variations in the parameters of periodic

structures can enable a gradient of propagation speed, which can be used for focusing or even trapping waves [71, 144].

If instead of varying in space, the properties of the medium vary in time, then new behaviors and functionalities arise. For example, it is possible to have discontinuities or interfaces in time that behave analogously to spatial interfaces between regions of differing propagation speed [80]. Likewise, instead of the strong attenuation or reflectivity associated with the band gaps of spatially periodic structures, temporally periodic media tend to amplify signals in a selective range of wavelengths [16, 17]. Such time-varying media have gained significant attention over the past decade and are continuing to see advancements in both concept and realization. Time-varying media, by adding a new dimension of control, promise a wide range of functionalities such as broadband amplification, frequency conversion, pulse shaping, and nonreciprocal propagation [5, 41, 118, 136], which have potential applications from radio-frequency acoustic devices [136] to energy harvesting [138]. Temporal variations have even been used to realize so-called synthetic dimensions, permitting the study of higher-dimensional physics in lower-dimensional systems [137].

In this thesis, we study these two simple but fundamental types of time-variation—discontinuities and periodic variations—in a discrete, one-dimensional phononic lattice. The phononic lattice provides two distinct advantages. First, the spatial periodicity leads to dispersion and phononic band gaps in the homogeneous case, which lead to several more general observable phenomena when the time-variation is applied compared to, for example, a homogenous, linear elastic bulk medium. Second, the discrete system allows for straightforward implementation of time-varying propagation speed since the control of elastic properties occurs only at the nodes, as opposed to applying a variation uniformly to a bulk medium. Since time-periodic variations of propagation speed lead to amplification and large amplitude response, we also study the dynamic stability of the system and investigate the role of the nonlinearity of the magnetic repulsive force that comprises the "springs" of the lattice.

1.2 Significance

Waves in time-varying systems have previously been studied almost exclusively for electromagnetic waves, so our work here aims to show both the successful implementation and potential utility of acoustic or elastic wave propagation in time-varying media. We present here the novel experimental demonstration of two

important wave phenomena in time-varying acoustic or elastic media. First, we measure the temporal refraction of waves across a temporal boundary in elastic properties, which is shown to be a close analog to the classical notion of refraction across a spatial boundary. Second, we study time-periodic variations, demonstrating the opening of so-called wavenumber band gaps, and then studying the stability of these systems. We show that the material nonlinearity of the experimental phononic lattice can serve to balance the linear instability of the time-periodic systems with the existence of additional stable states. We also explore the possible existence of temporally localized solutions inside the wavenumber band gap. The additional aspect of nonlinearity expands the possible applications of time-periodic systems with multistability and dynamics analogous to nonlinear optics. Since the dynamics of media with time-varying properties are limited neither by scale nor domain, we expect the principles demonstrated here to apply broadly to other acoustic or elastic systems, other types of time-variations, and more complex structures.

1.3 Waves in Discrete and Spatially Periodic Media

Wave propagation in discrete and periodic media has been studied extensively over the past several decades, beginning with Brillouin [10] and then photonic structures [52, 129], and quickly spreading and advancing in phononic systems [62, 77] as well. Two key features of periodic structures underpinning the majority of their functionalities are dispersion, and the existence of band gaps.

Dispersion of waves occurs when the propagation speed through a medium is not uniform for all frequencies. This is most clearly illustrated by the canonical example of the spring-mass chain, for which the equation of motion of the n^{th} mass is given by

$$m\frac{\partial^2 u_n(x,t)}{\partial t^2} + \beta\left(2u_n(x,t) - u_{n-1}(x,t) - u_{n+1}(x,t)\right) = 0, \tag{1.1}$$

where m is the mass of each discrete mass in the chain, and β is the spring constant of the linear stiffness connecting adjacent masses. We take a plane wave ansatz of the form

$$u_n(x,t) = Ue^{i(kx-\omega t)}, \tag{1.2}$$

where k is the wavenumber and ω is the frequency. Since the equilibrium position of the n^{th} may be determined by $x = na$, where a is the lattice constant. Substituting Eq. (1.2) into Eq. (1.1)

$$m\omega^2 Ue^{i(kna-\omega t)} = \beta U\left(e^{i(k(n-1)a-\omega t)} - 2e^{i(kna-\omega t)} + e^{i(k(n+1)a-\omega t)}\right), \tag{1.3}$$

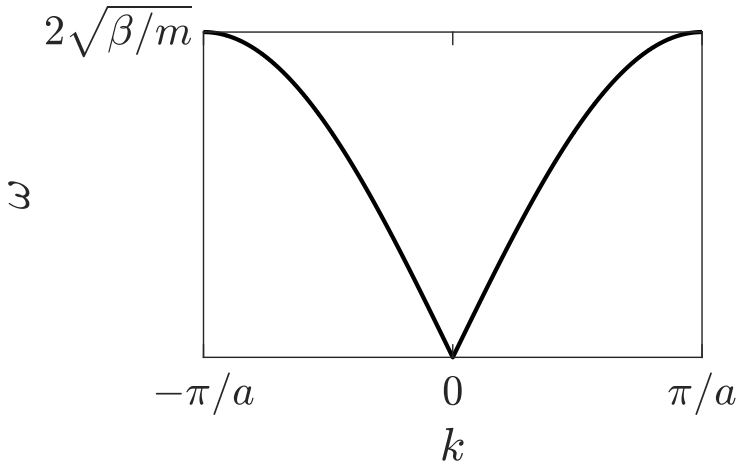

Figure 1.1: Monatomic dispersion relation (Eq. (1.4)).

simplifies to

$$m\omega^2 = \beta\left(e^{-ika} - 2 + e^{ika}\right) = \beta\left(e^{i\frac{ka}{2}} - e^{-i\frac{ka}{2}}\right)^2 = 4\beta\sin^2\frac{ka}{2},$$

and we therefore can write the frequency as a function of the wavelentgh $\omega = \omega(k)$, that is

$$\omega(k) = 2\sqrt{\frac{\beta}{m}}\left|\sin\frac{ka}{2}\right|. \tag{1.4}$$

The periodicity of $\omega(k) = \omega(k + 2\pi/a)$ means that solutions outside of the range of $-\pi/a \leq k \leq \pi/a$ are indistinguishable from and can be mapped onto the solutions inside this range, which is known as the first Brillouin zone. The first Brillouin zone is plotted in Fig. 1.1.

The function $\omega(k)$ of Eq. (1.4), termed the dispersion relation, provides useful information about the dynamics of the lattice. Not only does $\omega(k)$ relate frequency to wavenumber (or wavelength, since $\lambda = 2\pi/k$), but also its derivative $\partial\omega(k)/\partial k$ gives the propagation speed (or group velocity). Since it gives the group velocity of different frequencies at a given location on the dispersion branch, it describes how different frequency components of a wavepacket will disperse (become less spatially and temporally compact) as it propagates. This is contrast to a nondispersive medium, such as a homongenous, linear elastic solid, in which longitudinal waves of all frequencies propagate at the same speed c, a constant dependent on the material's properties in the wave equation $\partial_{tt}u = c^2\partial_{xx}u$. Thus, the dispersion relation is a crucial tool for designing structures for the control and manipulation of propagating waves, which always relies on controlling the velocity of propagation.

In addition, Eq. (1.4) for a dicrete lattice of identical springs and masses indicates that there is a maximum permissible frequency for propagating waves, or a cutoff frequency, above which no real solutions exist and waves cannot propagate. More generally, such a range is termed a frequency band gap, and for more complex structures, such as a diatomic chain of contrasting masses or contrasting stiffnesses, where an additional solution, or branch, arises, the range between real frequency branches are referred to as band gaps. In this sense, the monatomic lattice is essentially a low-pass filter, and diatomic lattices and more complex arrangements may act as band-stop filters, with the location and width of band gaps dependent on material constants (mass, stiffness). Moreover, the spectra of discrete systems, in contrast to continuous elastic systems such as phononic crystals, have a finite upper bounds.

It is observed that even this simplest possible example of a monatomic lattice leads to extraordinary dynamics compared to conventional bulk engineering materials, and the nature of wave propagation in acoustic and elastic spatially periodic phononic structures has been studied and applied extensively. First, the phononic band structures of these media were developed, often with the goal of discovering and designing "complete" phononic band gaps spanning one-, two-, and three-dimensional periodic media [13, 33, 50, 53, 62, 105, 122]. Two- and three-dimensional crystals with band structures containing directions with negative group velocities may be used to achieve effects such as negative refraction under certain conditions [98, 130].

Beyond the functionalities arising directly from the band structures of homogeneous periodic media, systems composed of multiple different phononic crystals [65, 132, 135], different phases or orientations of the same phononic crystal [119, 141], or phononic crystals with defects [75] can achieve additional control of transmission and waveguiding. Phononic crystal waveguides [56, 57] have also been successfully demonstrated utilizing designs inspired by their photonic counterparts [79, 84].

Apart from interfaces and boundaries, the parameters of a periodic medium can be varied smoothly (approximately), in order to achieve a spatial gradient of propagation speeds. The first application of this is the design of lens-like structures, where, in place of the geometry of a classical lens, a spatial profile of index of refraction (that is, group velocity) in a phononic medium focuses beams with a significant degree of tunability [30, 71]. Aside from focusing or guiding [44], gradient-index phononic media have been used to implement rainbow traps [116] or broadband absorbers [23, 140].

Beyond basic periodic structures, acoustic and elastic metamaterials can typically be distinguished from phononic crystals by the classification of its unit cells as "meta-atoms," especially including some kind of locally resonant effect [26, 72, 142]. These differ from phononic crystals in that they need not have periodicity on the scale of the propagating wavelengths of interest. Another key example of discrete, periodic structures is granular media, although most of the extraordinary properties of these systems arise from their nonlinear interaction forces (see Section 1.5 for more).

1.4 Wave Propagation in Time-Varying Media

Recently, waves in time-varying media have rapidly developed into a complementary sub-field to the study of photonic, phononic, and other spatially periodic media. Although not all time-varying phenomena are new, such as parametric amplification [25, 117], their contextualization as the temporal analog to spatially structured media has greatly accelerated interest and inspired new discoveries and applications. The field has largely been driven by interest nonreciprocity [88] and topological effects [1], but time-varying media as a whole spans a wide range of concepts [11]. To connect the concepts of time variation to their spatial predecessors, an illustration of typical (periodic) medium variations is shown in Fig. 1.2. The white and shaded regions represent a modulation of medium properties that affect propagation speed, such as stiffness or mass, of a form like

$$A(x,t) = A_0 + \Delta A f(x,t).$$

When f is Λ periodic in x, $f(x,t) = f(x+\Lambda,t)$, the modulation, shown in panel (a), takes the form of a prototypical spatially periodic medium, such as a phononic crystal, as discussed in Section 1.3. Panels (b) and (c), on the other hand, each have a temporal component, (b) portraying a purely time-periodic medium, that is $f(x,t) = f(x,t+T)$, and (c) a spatiotemporally periodic medium with a traveling-wave-like modulation, $f(x,t) = f(x+\Lambda,t+T)$. The latter two cases are discussed in this section.

Temporal discontinuities

The simplest concept (although not the simplest realization) of time-varying media is the temporal boundary. Like a perfect spatial boundary, a temporal boundary is an interface between two media with different properties, and most importantly, different propagation speeds. Unlike a spatial boundary, however, a temporal boundary is a spatially uniform (i.e., everywhere), temporally discontinuous change of the

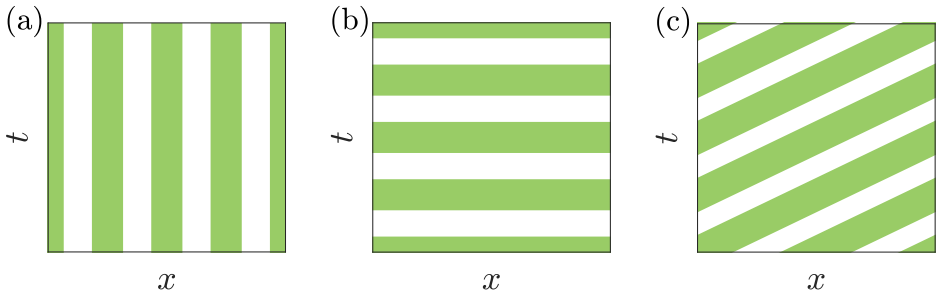

Figure 1.2: Periodic medium property variation. **(a)** Spatially periodic modulation. **(b)** Temporally periodic modulation. **(c)** Spatiotemporally periodic modulation.

properties of the medium. This was first proposed in 1958 by Morgenthaler [85], and has since been contextualized as the space-time dual to the refraction of waves across a spatial interface [80]. The following example adapted from [80] most clearly illustrates this.

Consider a one-dimensional, non-dispersive medium with a spatial boundary at $x = 0$ with propagation speeds c_0 and c_1 for $x < 0$ and $x > 0$, respectively. For a plane wave incident on the boundary, we will have incident and reflect waves

$$u(x,t) = U_i e^{i(k_i x - \omega_i t)} + U_r e^{i(k_r x - \omega_r t)}, \ x < 0, \tag{1.5}$$

and a transmitted wave

$$u(x,t) = U_t e^{i(k_t x - \omega_t t)}, \ x > 0, \tag{1.6}$$

where $\omega_i = c_0 k_i$, $\omega_r = c_0 k_r$, and $\omega_t = c_1 k_t$. At the boundary $x = 0$, $U_i e^{-i\omega_i t} + U_r e^{-i\omega_r t} = U_t e^{-i\omega_t t}$, which will be true for all t only if $\omega_i = \omega_r = \omega_t = \omega$. Therefore, frequency is conserved and, from the dispersion relations on either side of the spatial boundary, we have $k_i = k_r = \omega/c_0$ and $k_t = \omega/c_1$, and our relation for the change in wavelength across the boundary

$$\frac{k_t}{k_i} = \frac{c_0}{c_1}. \tag{1.7}$$

We now consider a temporal boundary at time $t = 0$ with a change in propagation speed from c_0 to c_1, beginning with the same plane wave solutions, but instead of for $x < 0$ and $x > 0$, Eqs. (1.5) and (1.6) become

$$u(x,t) = U_i e^{i(k_i x - \omega_i t)}, \ t < 0,$$

and

$$u(x,t) = U_t e^{i(k_t x - \omega_t t)} + U_r e^{i(k_r x - \omega_r t)}, \ t > 0,$$

respectively. Now we find that at the boundary, $U_i e^{ik_i x} = U_r e^{ik_r x} + U_t e^{ik_t x}$ for all x, and so now $k_i = k_r = k_t = k$, the wavenumber or wavelength, is conserved. Now, $\omega_i = c_0 k$ and $\omega_r = \omega_t = c_1 k$. Thus, like of a change in wavenumber across a spatial boundary, there is a change in frequency across the temporal boundary, that is

$$\frac{\omega_t}{\omega_i} = \frac{c_1}{c_0}. \tag{1.8}$$

The intuitive spatial reasoning behind Eq. (1.8) is valuable [85]. Let us consider a plane wave in an infinite medium of temporal frequency ω_i, spatial frequency (i.e., wavenumber) k_i, and speed c_0 ($\omega_i = c_0 k_i$), which encounters the temporal boundary at time $t = 0$. Then at the instant $t = 0$ when the propagation speed of the medium changes everywhere (for all x) from c_0 to c_1, the spatial profile of the wave does not change, but the whole spatial profile of the plane wave must now propagate at the new speed c_1. In other words, the wavenumber has been conserved $k_i = k_t = k$, and the frequency must change to maintain the relationships $\omega_r = \omega_t = c_1 k$, and we can again obtain the result in Eq. (1.8).

The utility of such frequency conversion is readily apparent, and proposed implementation schemes include various types of systems such as graphene plasmons [81] or optical waves in a parallel plate waveguide with rapidly changing boundary conditions [110]. A handful of experimental demonstrations have been made in optics, plasmas, and water waves [3, 64, 92, 143], but temporal refraction has not been shown before in acoustic or elastic systems.

The sharpness (and lack thereof) of imperfect step-like temporal boundaries has also been considered and can have a significant impact on the reflectivity and transmissivity [54, 139], which could, in some cases, be used to control backscattering. The concept of temporal boundaries is, in theory, general to all domains, but implementation of perfect, step-like jumps in propagation speed, poses potential challenges depending on the necessary speed and depth of the modulation. This is one of the primary advantages of implementing time-variation of any kind in discrete media. For example, a temporal boundary, even in a finite continuous system, may require a strong, uniform external field, which must span the entire system spatially. In contrast, a temporal boundary in a finite, discrete medium requires modulation of properties only at a finite number of discrete elements of the system.

Just as in the case of spatial boundaries, two or more temporal boundaries can be combined to achieve additional functionalities. Temporal layers and slabs have the advantage of being finite in duration (a single temporal boundary is semi-infinite

in time), and by tuning the "thickness" and amplitude of the change in propagation speed, it is possible to realize systems and devices such as anti-reflection "temporal coatings" [93], absorbers [69], and phase conjugation [133]. In general, it is mostly straightforward to conceive of temporal multi-layer structures, whose parameters can be tuned to exert extraordinary control over transmission and reflection [11, 12, 99, 100].

Time-periodic media

Just as temporal boundaries serve as an analog to spatial interfaces, so too do time-periodic media relate to spatially periodic structures. The concept of time-period modulations of medium properties is not a new one and has been widely utilized since its development its initial development in parametric amplification in transmission lines [25, 117]. The understanding of wave porpagation in time-periodic media has also been around for over half of a century [16], but it has been revitalized by the recent study of waves in time-varying media. Transmission lines [101], time-varying photonic crystals [66], and phononic systems [58] specifically have been employed in the study of pure wavenumber band gaps, which, like with temporal and spatial refraction, serve as a temporal analog for spatial periodicity. Unlike frequency band gaps, which strongly attenuate propagating waves in a range of the dispersion relation that has no real frequency solutions, wavenumber band gaps are a range of wavenumbers for which there is a frequency solution with a constant real and positive imaginary part, representing a standing wave with nonzero gain [121]. Although this seems contrary to the notion of a typical band gap, the zero group velocity of the wavenumber band gap does indeed correspond to a lack of propagating waves.

Because the parametric amplification inherent to harmonically modulated systems may lead to time exponentially growing response, an understanding of stability is required. In the simplest case, particularly when a system may be modeled by a system of linear ordinary differential equations with time-periodic coefficients, Floquet theory can be employed to determine stability conditions of the modulation and system parameters [58, 68]. A detail of note is that in finite discrete systems, since oscillations are composed of a finite number of discrete modes, it is possible for the system to avoid instability at parameters that would otherwise lead to exponential growth in an system of infinite length [68].

Spatiotemporal media

It is also possible to combine spatial and temporal variations in the properties of a medium, and such systems exhibit some of the most extraordinary behaviors of any structured wave media. Perhaps the first logical step is a combination of spatial and temporal boundaries, which by repeated cycles of alternating spatial and temporal refraction, can achieve large blue- or red-shifting of signals [3]. General space-time media can convert frequency, shape pulses, or amplify or filter signals [5, 11, 12].

One of the most studied applications of simultaneously space- and time-varying media is to achieve nonreciprocal wave propagation. Although directional transmission or filtering can be achieved via nonlinearity or asymmetry [9, 70], spatiotemporal nonreciprocal systems promise the same functionalities without common limitations such as distortion or attenuation. Typically, a traveling-wave-like modulation, which is spatially and temporally periodic, imparts a Doppler-like effect onto signals traveling in the medium, biasing the Bragg-like scattering or reflection and leading to one-way band gaps [19, 43, 48, 76, 86, 113, 120, 124]. Most often the modulation is of the constitutive properties of the medium, but alternative approaches exist, such as a wave-like modulation of boundary conditions [127]. Large amplitude modulations can also lead to more exotic effects, such as Willis coupling [87].

Spatiotemporal media may also be used to realize topological effects. The refers to the topology of the phase and band structure of a medium, and certain features or quantities which may be invariants, leading to dynamics that are robust, or protected, against defects or the geometry of the medium [1, 31]. Topological materials do not necessarily require time-variation [18, 135], but time-varying components [28], rotating components [123], or components with bias velocities [38] are often employed to achieve an elastic or acoustic analog of quantum spin. This can enable the confinement waves outside the bulk of a finite medium (ends in one, edges in two, and surfaces in three dimensions), where they will propagate along around sharp corners and arbitrary boundaries without in only one direction nonreciprocally, since theses spin-like components break time reversal symmetry [1, 88].

Closely related to topology is the concept of synthetic dimensions, by which the number of dimensions in a system can be extended beyond its real spatial dimensions. Inducing a coupling of states of a system, achieved for example by a dynamic modulation, may form a lattice of states, acting as a synthetic lattice of states through which energy in the system may travel [137]. This synthetic dimension can be used to demonstrate higher dimensional topological effects, such as topological

insulators, in lower dimensional systems [73, 131]. Like the various strategies for implementing topological effects using an analog of quantum spin, synthetic dimensions offer an avenue for exploring physics that are often not available in classical systems, including acoustic systems [20, 34, 91, 128].

Once again, dispersion relations offer an excellent tool to understand the dynamics periodic systems. Wave porpagation in a medium with a traveling-wave-like modulation can roughly be understood by the interaction between incident and scattered fields. The incident field on a dispersion diagram is simply the dispersion relation of the unmodulated medium. For a traveling-wave modulation, with modulation frequency Ω and wavenumber g, the scattered fields are copies of the unmodulated dispersion relation which have been translated by $(+\Omega, +g)$ and $(-\Omega, -g)$ in the inverse space. There is coupling between the incident and scattered fields only where they intersect, and it is at these intersections that band gaps emerge [86].

Fig. 1.3 illustrates the effect of the modulation wave speed on the dispersion relation of a medium. For a zero velocity modulation, the medium is only spatially periodic, and the familiar structure of a Bragg reflector is found. Likewise, the limit of an infinite velocity modulation is a purely time-periodic medium, with parametrically amplified wavenumber band gaps. Purely space- and time-periodic media are reciprocal; for finite velocities, three nonreciprocal cases emerge. In the first special case, where the modulation velocity matches the propagation velocity of the medium, broadband nonreciprocal amplification is possible [41, 61]. Then, modulation speeds less than the propagation speed (subsonic) open nonreciprocal frequency band gaps, and modulation speeds greater than the propagation speed (supersonic) open nonreciprocal wavenumber band gaps. A example of a spatiotemporally modulated phononic lattice and the construction of its modulated dispersion relation is shown in Fig. 1.3.

Spatiotemporal media are another case in which discrete materials offer a significant advantage here over continuous media, because a traveling wave like modulation can be achieved simply by modulating discrete elements harmonically in time, then adding an appropriate phase shift in each element's modulation along the spatial direction. Not only does this eliminate the need for a large externally applied field [2], but its also readily enables traveling wave-like modulations with velocities much larger than the speed of sound (or light) in the medium. Moreover, the non-trivial dispersive band-structure of discrete media provides a additional design tool, such

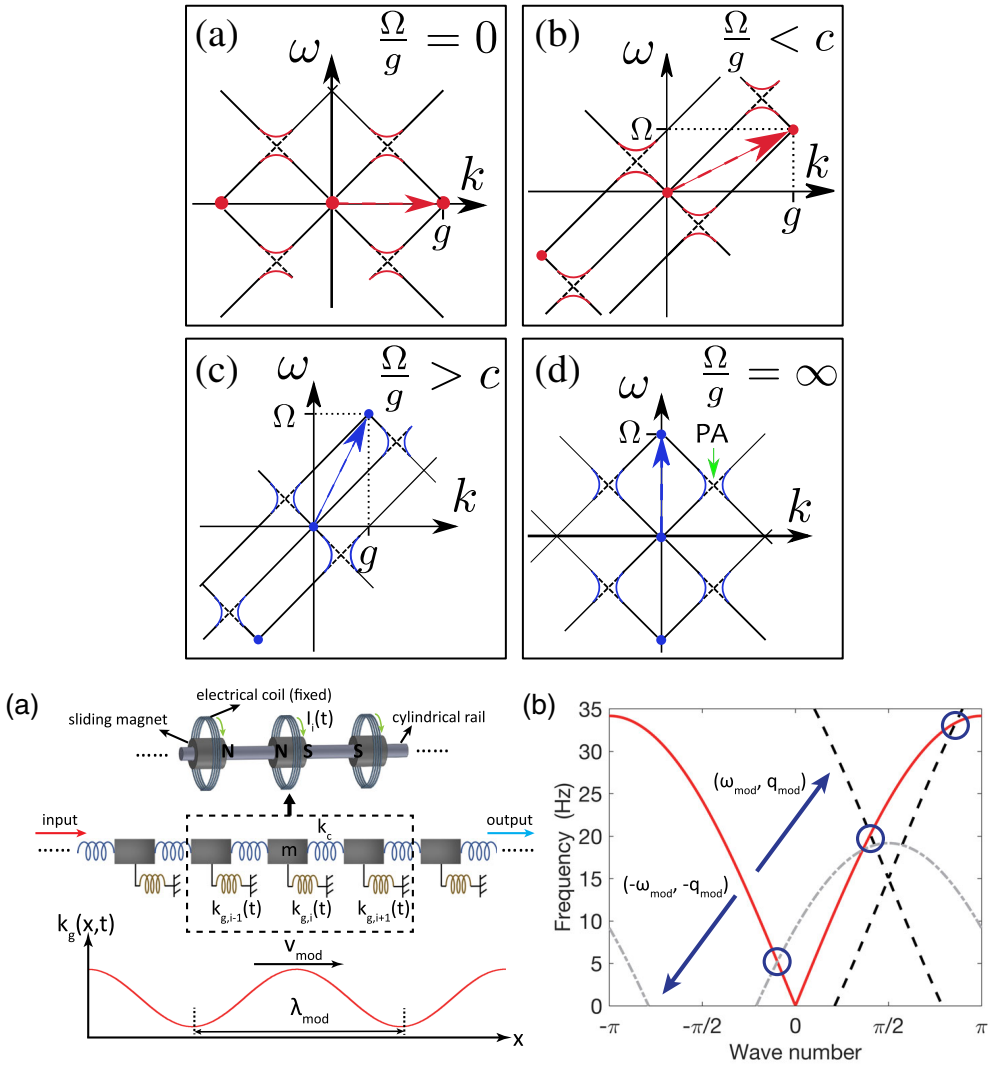

Figure 1.3: Spatiotemporally modulated media. Top panels (a)-(d): Formation of band gaps in a non-dispersive spatiotemporal medium with propagation speed c for different cases of modulation wave speed, given by the ratio of modulation temporal frequency Ω and modulation wavenumber g. Reprinted figure with permission from [41]. Copyright 2019 by the American Physical Society.
Lower panels: (a) Schematic of magnet-based acoustic phononic lattice with traveling-wave-like modulation of grounding stiffness. (b) Depiction of modulated dispersion relation, with circles indicating intersections between the homogeneous (red) and modulation scattered (dashed) dispersion curves. Reprinted figure with permission from [124]. Copyright 2018 by the American Physical Society.

that an appropriate modulation may be selected to make use of the multiple available modes [87].

1.5 Dynamics of Nonlinear, Discrete Systems

Nonlinear and granular media

The systems and examples so far have all been based on the linear dynamics of space- and time-varying media, but the dynamics of and control of waves in nonlinear media have also been widely studied. As in the case of the experimental phononic lattice presented in this thesis, while the small displacement regime is often described well by a linear model, the full dynamics of many engineering and real-world systems are actually nonlinear. Since the first insights into discrete nonlinear systems discovered in the Fermi-Pasta-Ulam-Tsingou problem [35], waves in discrete nonlinear media have been investigated in a variety of contexts, especially granular media [90, 111], where solitary waves [24, 63, 104, 111], shock waves [45, 83], and localization or breathers [8, 14, 55, 103, 112, 114, 115] have been studied and demonstrated. Such nonlinear wave phenomena have proposed applications including focusing [109] or energy trapping and absorption [29, 39, 47].

Discrete breathers, also known as intrinsic localized modes, are a well-studied type of nonlinear coherent structure, which are localized in space, and periodic in time [22, 36, 37]. In linear discrete systems, one primary strategy for achieving localized vibrations is the introductions of defects to a lattice or periodic structure, breaking the transnational symmetry [37]. Defects in linear phononic and photonic systems have been applied to the design of devices such as filters, waveguides, acoustic flatbands, energy harvesting, or acoustic devices for coupling to quantum systems [4, 32, 74, 75, 102]. Discrete nonlinear systems, on the other hand, have been shown to support (sometimes strongly) spatially localized and temporally periodic modes, which generally exist outside the linear spectrum of the discrete structure, without breaking transnational symmetry [36, 37].

Another important feature of nonlinear systems is the possible existence of bistability of output amplitude or power with respect to the input. This phenomenon has been demonstrated in spatially periodic or discrete optical systems including superlattices and photonic crystals, usually with Kerr nonlinearities [27, 107, 108, 125, 126]. The classical hysteresis loop [89] that is typical to these examples may be used to implement memory and switching behavior optically [7, 94, 108]. Bistable

behavior has also been observed in transmission lines [96] and in mechanical discrete nonlinear media, in particular, granular chains [21].

Nonlinear time-varying systems

The propagation of waves in nonlinear media with time-varying or time-periodic properties has received far less attention than any of the previously discussed spatial, temporal, or discrete nonlinear structures. Indeed, other than general [40, 106], only a handful of examples in literature examine nonlinear media with time-periodic variation [60, 97]. In a nonlinear transmission line, which had been shown previously to exhibit multistability [96], parametric amplification is observed, including for signal frequencies within the stop band [97]. Parametric generation is also observed, occurring after the pump amplitude reaches a threshold, overcoming damping [59, 60].

Other recent work has focused on exploring modes within wavenumber band gaps, similar to the notion of discrete breathers in the gaps of the linear spectra of nonlinear spatially discrete or periodic media. These k-gap, or momentum gap, solitons have been explored in nonlinear photonic time crystals [6, 95], showing the existence of temporally localized solutions inside the wavenumber band gaps of nonlinear, time-periodic meida. Such systems are closely related to microresonators [46, 78, 134] and optical cavities [67] aimed at frequency comb generation, which is essential to metrology and high frequency technologies. Although phononic frequency combs have been studied [15, 42], temporally localized wavenumber gap solutions in acoustic and elastic systems have received less attention than their optical counterparts.

References

[1] A. Alù, C. Daraio, P. A. Deymier, and M. Ruzzene. Topological Acoustics. *Acoustics Today*, 17(3):13, 2021. ISSN 15570215. doi: 10.1121/AT.2021.17.3.13. URL https://acousticstoday.org/issues/2021AT/Fall2021/index.html#p=13.

[2] M. H. Ansari, M. A. Attarzadeh, M. Nouh, and M. A. Karami. Application of magnetoelastic materials in spatiotemporally modulated phononic crystals for nonreciprocal wave propagation. *Smart Materials and Structures*, 27(1): 015030, Dec. 2017. ISSN 0964-1726. doi: 10.1088/1361-665X/aa9d3d. URL https://doi.org/10.1088%2F1361-665x%2Faa9d3d.

[3] B. Apffel and E. Fort. Frequency conversion cascade by crossing multiple space and time interfaces. *Physical Review Letters*, 128(6):064501, Feb. 2022. ISSN 0031-9007, 1079-7114. doi: 10.1103/PhysRevLett.128.064501. URL https://link.aps.org/doi/10.1103/PhysRevLett.128.064501.

[4] P. Arrangoiz-Arriola, E. A. Wollack, M. Pechal, J. D. Witmer, J. T. Hill, and A. H. Safavi-Naeini. Coupling a superconducting quantum circuit to a phononic crystal defect cavity. *Physical Review X*, 8(3):031007, July 2018. doi: 10.1103/PhysRevX.8.031007. URL https://link.aps.org/doi/10.1103/PhysRevX.8.031007.

[5] F. Biancalana, A. Amann, A. V. Uskov, and E. P. O'Reilly. Dynamics of light propagation in spatiotemporal dielectric structures. *Physical Review E*, 75(4): 046607, Apr. 2007. ISSN 1539-3755, 1550-2376. doi: 10.1103/PhysRevE.75.046607. URL https://link.aps.org/doi/10.1103/PhysRevE.75.046607.

[6] F. Biancalana, A. Amann, and E. P. O'Reilly. Gap solitons in spatiotemporal photonic crystals. *Physical Review A*, 77(1):011801, Jan. 2008. doi: 10.1103/PhysRevA.77.011801. URL https://link.aps.org/doi/10.1103/PhysRevA.77.011801.

[7] L. D. Bino, N. Moroney, and P. Del'Haye. Optical memories and switching dynamics of counterpropagating light states in microresonators. *Optics Express*, 29(2):2193–2203, Jan. 2021. ISSN 1094-4087. doi: 10.1364/OE.417951. URL https://opg.optica.org/oe/abstract.cfm?uri=oe-29-2-2193.

[8] N. Boechler, G. Theocharis, S. Job, P. G. Kevrekidis, M. A. Porter, and C. Daraio. Discrete breathers in one-dimensional diatomic granular crystals. *Physical Review Letters*, 104(24):244302, June 2010. doi: 10.1103/PhysRevLett.104.244302. URL https://link.aps.org/doi/10.1103/PhysRevLett.104.244302.

[9] N. Boechler, G. Theocharis, and C. Daraio. Bifurcation-based acoustic switching and rectification. *Nature Materials*, 10(9):665–668, Sept. 2011. ISSN 1476-4660. doi: 10.1038/nmat3072. URL https://www.nature.com/articles/nmat3072.

[10] L. Brillouin. Wave propagation in periodic structures : Electric filters and crystal lattices, 1953. URL https://cds.cern.ch/record/106186.

[11] C. Caloz and Z.-L. Deck-Léger. Spacetime metamaterials—Part II: Theory and applications. *IEEE Transactions on Antennas and Propagation*, 68(3): 1583–1598, Mar. 2020. ISSN 1558-2221. doi: 10.1109/TAP.2019.2944216.

[12] C. Caloz and Z.-L. Deck-Léger. Spacetime metamaterials—Part I: General concepts. *IEEE Transactions on Antennas and Propagation*, 68(3):1569–1582, Mar. 2020. ISSN 1558-2221. doi: 10.1109/TAP.2019.2944225.

[13] R. E. Camley, B. Djafari-Rouhani, L. Dobrzynski, and A. A. Maradudin. Transverse elastic waves in periodically layered infinite and semi-infinite media. *Physical Review B*, 27(12):7318–7329, June 1983. ISSN 0163-1829. doi: 10.1103/PhysRevB.27.7318. URL https://link.aps.org/doi/10.1103/PhysRevB.27.7318.

[14] D. K. Campbell, S. Flach, and Y. S. Kivshar. Localizing energy through nonlinearity and discreteness. *Physics Today*, 57(1):43–49, Jan. 2004. ISSN 0031-9228. doi: 10.1063/1.1650069. URL https://physicstoday-scitation-org.caltech.idm.oclc.org/doi/10.1063/1.1650069.

[15] L. S. Cao, D. X. Qi, R. W. Peng, M. Wang, and P. Schmelcher. Phononic frequency combs through nonlinear resonances. *Physical Review Letters*, 112(7):075505, Feb. 2014. doi: 10.1103/PhysRevLett.112.075505. URL https://link.aps.org/doi/10.1103/PhysRevLett.112.075505.

[16] E. S. Cassedy. Dispersion relations in time-space periodic media part II—Unstable interactions. *Proceedings of the IEEE*, 55(7):1154–1168, July 1967. ISSN 0018-9219. doi: 10.1109/PROC.1967.5775.

[17] E. S. Cassedy and A. A. Oliner. Dispersion relations in time-space periodic media: Part I—Stable interactions. *Proceedings of the IEEE*, 51(10):1342–1359, Oct. 1963. ISSN 0018-9219. doi: 10.1109/PROC.1963.2566.

[18] J. Cha, K. W. Kim, and C. Daraio. Experimental realization of on-chip topological nanoelectromechanical metamaterials. *Nature*, 564(7735):229–233, Dec. 2018. ISSN 1476-4687. doi: 10.1038/s41586-018-0764-0. URL https://www.nature.com/articles/s41586-018-0764-0.

[19] Y. Chen, X. Li, H. Nassar, A. N. Norris, C. Daraio, and G. Huang. Nonreciprocal wave propagation in a continuum-based metamaterial with space-time modulated resonators. *Physical Review Applied*, 11(6):064052, June 2019. ISSN 2331-7019. doi: 10.1103/PhysRevApplied.11.064052. URL https://link.aps.org/doi/10.1103/PhysRevApplied.11.064052.

[20] Z.-G. Chen, W. Zhu, Y. Tan, L. Wang, and G. Ma. Acoustic realization of a four-dimensional higher-order Chern insulator and boundary-modes engineering. *Physical Review X*, 11(1):011016, Jan. 2021. doi: 10.1103/PhysRevX.11.011016. URL https://link.aps.org/doi/10.1103/PhysRevX.11.011016.

[21] C. Chong, F. Li, J. Yang, M. O. Williams, I. G. Kevrekidis, P. G. Kevrekidis, and C. Daraio. Damped-driven granular chains: An ideal playground for dark breathers and multibreathers. *Physical Review E*, 89(3):032924, Mar. 2014. doi: 10.1103/PhysRevE.89.032924. URL https://link.aps.org/doi/10.1103/PhysRevE.89.032924.

[22] C. Chong, M. A. Porter, P. G. Kevrekidis, and C. Daraio. Nonlinear coherent structures in granular crystals. *Journal of Physics: Condensed Matter*, 29(41):413003, Sept. 2017. ISSN 0953-8984. doi: 10.1088/1361-648X/aa7672. URL https://dx.doi.org/10.1088/1361-648X/aa7672.

[23] A. Climente, D. Torrent, and J. Sánchez-Dehesa. Omnidirectional broadband acoustic absorber based on metamaterials. *Applied Physics Letters*, 100 (14):144103, Apr. 2012. ISSN 0003-6951. doi: 10.1063/1.3701611. URL https://aip.scitation.org/doi/10.1063/1.3701611.

[24] C. Coste, E. Falcon, and S. Fauve. Solitary waves in a chain of beads under Hertz contact. *Physical Review E*, 56(5):6104–6117, Nov. 1997. doi: 10.1103/PhysRevE.56.6104. URL https://link.aps.org/doi/10.1103/PhysRevE.56.6104.

[25] A. L. Cullen. A travelling-wave parametric amplifier. *Nature*, 181(4605): 332–332, Feb. 1958. ISSN 1476-4687. doi: 10.1038/181332a0. URL https://www.nature.com/articles/181332a0.

[26] S. A. Cummer, J. Christensen, and A. Alù. Controlling sound with acoustic metamaterials. *Nature Reviews Materials*, 1(3):1–13, Feb. 2016. ISSN 2058-8437. doi: 10.1038/natrevmats.2016.1. URL https://www.nature.com/articles/natrevmats20161.

[27] J. Danckaert, K. Fobelets, I. Veretennicoff, G. Vitrant, and R. Reinisch. Dispersive optical bistability in stratified structures. *Physical Review B*, 44 (15):8214–8225, Oct. 1991. doi: 10.1103/PhysRevB.44.8214. URL https://link.aps.org/doi/10.1103/PhysRevB.44.8214.

[28] A. Darabi, X. Ni, M. Leamy, and A. Alù. Reconfigurable Floquet elastodynamic topological insulator based on synthetic angular momentum bias. *Science Advances*, 6(29):eaba8656, July 2020. doi: 10.1126/sciadv.aba8656. URL https://www.science.org/doi/10.1126/sciadv.aba8656.

[29] C. Daraio, V. F. Nesterenko, E. B. Herbold, and S. Jin. Energy trapping and shock disintegration in a composite granular medium. *Physical Review Letters*, 96(5):058002, Feb. 2006. doi: 10.1103/PhysRevLett.96.058002. URL https://link.aps.org/doi/10.1103/PhysRevLett.96.058002.

[30] K. Deng, Y. Ding, Z. He, H. Zhao, J. Shi, and Z. Liu. Graded negative index lens with designable focal length by phononic crystal. *Journal of Physics D: Applied Physics*, 42(18):185505, Sept. 2009. ISSN 0022-3727. doi: 10.1088/0022-3727/42/18/185505. URL https://dx.doi.org/10.1088/0022-3727/42/18/185505.

[31] P. Deymier and K. Runge. *Sound Topology, Duality, Coherence and Wave-Mixing*, volume 188 of *Springer Series in Solid-State Sciences*. Springer

International Publishing, Cham, 2017. ISBN 978-3-319-62379-5 978-3-319-62380-1. doi: 10.1007/978-3-319-62380-1. URL http://link.springer.com/10.1007/978-3-319-62380-1.

[32] H.-W. Dong, Y.-S. Wang, and C. Zhang. Inverse design of high-Q wave filters in two-dimensional phononic crystals by topology optimization. *Ultrasonics*, 76:109–124, Apr. 2017. ISSN 0041-624X. doi: 10.1016/j.ultras.2016.12.018. URL https://www.sciencedirect.com/science/article/pii/S0041624X16304279.

[33] R. Esquivel-Sirvent and G. H. Cocoletzi. Band structure for the propagation of elastic waves in superlattices. *The Journal of the Acoustical Society of America*, 95(1):86–90, Jan. 1994. ISSN 0001-4966. doi: 10.1121/1.408301. URL http://asa.scitation.org/doi/10.1121/1.408301.

[34] X. Fan, C. Qiu, Y. Shen, H. He, M. Xiao, M. Ke, and Z. Liu. Probing Weyl physics with one-dimensional sonic crystals. *Physical Review Letters*, 122(13):136802, Apr. 2019. doi: 10.1103/PhysRevLett.122.136802. URL https://link.aps.org/doi/10.1103/PhysRevLett.122.136802.

[35] E. Fermi, J. Pasta, S. Ulam, and M. Tsingou. Studies of the nonlinear problems. doi: 10.2172/4376203. URL https://www.osti.gov/biblio/4376203.

[36] S. Flach and A. V. Gorbach. Discrete breathers — Advances in theory and applications. *Physics Reports*, 467(1):1–116, Oct. 2008. ISSN 0370-1573. doi: 10.1016/j.physrep.2008.05.002. URL https://www.sciencedirect.com/science/article/pii/S0370157308001580.

[37] S. Flach and C. R. Willis. Discrete breathers. *Physics Reports*, 295(5):181–264, Mar. 1998. ISSN 0370-1573. doi: 10.1016/S0370-1573(97)00068-9. URL https://www.sciencedirect.com/science/article/pii/S0370157397000689.

[38] R. Fleury, D. L. Sounas, C. F. Sieck, M. R. Haberman, and A. Alù. Sound isolation and giant linear nonreciprocity in a compact acoustic circulator. *Science*, 343(6170):516–519, Jan. 2014. doi: 10.1126/science.1246957. URL https://www-science-org.caltech.idm.oclc.org/doi/10.1126/science.1246957.

[39] F. Fraternali, M. A. Porter, and C. Daraio. Optimal design of composite granular protectors. *Mechanics of Advanced Materials and Structures*, 17 (1):1–19, Dec. 2009. ISSN 1537-6494. doi: 10.1080/15376490802710779. URL https://doi.org/10.1080/15376490802710779.

[40] A. P. Gabale and S. C. Sinha. A direct analysis of nonlinear systems with external periodic excitations via normal forms. *Nonlinear Dynamics*, 55(1):79–93, Jan. 2009. ISSN 1573-269X. doi: 10.1007/s11071-008-9346-2. URL https://doi.org/10.1007/s11071-008-9346-2.

[41] E. Galiffi, P. A. Huidobro, and J. B. Pendry. Broadband nonreciprocal amplification in luminal metamaterials. *Physical Review Letters*, 123 (20):206101, Nov. 2019. doi: 10.1103/PhysRevLett.123.206101. URL https://link.aps.org/doi/10.1103/PhysRevLett.123.206101.

[42] A. Ganesan, C. Do, and A. Seshia. Phononic frequency comb via intrinsic three-wave mixing. *Physical Review Letters*, 118(3):033903, Jan. 2017. doi: 10.1103/PhysRevLett.118.033903. URL https://link.aps.org/doi/10.1103/PhysRevLett.118.033903.

[43] B. M. Goldsberry, S. P. Wallen, and M. R. Haberman. Non-reciprocal wave propagation in mechanically-modulated continuous elastic metamaterials. *The Journal of the Acoustical Society of America*, 146(1):782–788, July 2019. ISSN 0001-4966. doi: 10.1121/1.5115019. URL http://asa.scitation.org/doi/10.1121/1.5115019.

[44] Z. He, F. Cai, and Z. Liu. Guiding acoustic waves with graded phononic crystals. *Solid State Communications*, 148(1):74–77, Oct. 2008. ISSN 0038-1098. doi: 10.1016/j.ssc.2008.07.007. URL https://www.sciencedirect.com/science/article/pii/S0038109808003906.

[45] E. B. Herbold and V. F. Nesterenko. Solitary and shock waves in discrete strongly nonlinear double power-law materials. *Applied Physics Letters*, 90(26):261902, June 2007. ISSN 0003-6951. doi: 10.1063/1.2751592. URL https://aip-scitation-org.caltech.idm.oclc.org/doi/10.1063/1.2751592.

[46] T. Herr, V. Brasch, J. D. Jost, C. Y. Wang, N. M. Kondratiev, M. L. Gorodetsky, and T. J. Kippenberg. Temporal solitons in optical microresonators. *Nature Photonics*, 8(2):145–152, Feb. 2014. ISSN 1749-4893. doi: 10.1038/nphoton.2013.343. URL https://www.nature.com/articles/nphoton.2013.343.

[47] J. Hong. Universal power-law decay of the impulse energy in granular protectors. *Physical Review Letters*, 94(10):108001, Mar. 2005. doi: 10.1103/PhysRevLett.94.108001. URL https://link.aps.org/doi/10.1103/PhysRevLett.94.108001.

[48] J. Huang and X. Zhou. Non-reciprocal metamaterials with simultaneously time-varying stiffness and mass. *Journal of Applied Mechanics*, 87(071003), Apr. 2020. ISSN 0021-8936. doi: 10.1115/1.4046844. URL https://doi.org/10.1115/1.4046844.

[49] C. Jamois, R. B. Wehrspohn, L. C. Andreani, C. Hermann, O. Hess, and U. Gösele. Silicon-based two-dimensional photonic crystal waveguides. *Photonics and Nanostructures - Fundamentals and Applications*, 1 (1):1–13, Dec. 2003. ISSN 1569-4410. doi: 10.1016/j.photonics.2003.10.

001. URL https://www.sciencedirect.com/science/article/pii/S1569441003000099.

[50] J. S. Jensen. Phononic band gaps and vibrations in one- and two-dimensional mass–spring structures. *Journal of Sound and Vibration*, 266(5):1053–1078, Oct. 2003. ISSN 0022-460X. doi: 10.1016/S0022-460X(02)01629-2. URL https://www.sciencedirect.com/science/article/pii/S0022460X02016292.

[51] J. D. Joannopoulos, P. R. Villeneuve, and S. Fan. Photonic crystals: Putting a new twist on light. *Nature*, 386(6621):143–149, Mar. 1997. ISSN 1476-4687. doi: 10.1038/386143a0. URL https://www.nature.com/articles/386143a0.

[52] S. John. Strong localization of photons in certain disordered dielectric superlattices. *Physical Review Letters*, 58(23):2486–2489, June 1987. doi: 10.1103/PhysRevLett.58.2486. URL https://link.aps.org/doi/10.1103/PhysRevLett.58.2486.

[53] M. Kafesaki, M. M. Sigalas, and E. N. Economou. Elastic wave band gaps in 3-D periodic polymer matrix composites. *Solid State Communications*, 96(5):285–289, Nov. 1995. ISSN 0038-1098. doi: 10.1016/0038-1098(95)00444-0. URL https://www.sciencedirect.com/science/article/pii/0038109895004440.

[54] D. Kalluri and T. Huang. Longitudinal propagation in a magnetized time-varying plasma: Development of Green's function. *IEEE Transactions on Plasma Science*, 26(3):1022–1030, June 1998. ISSN 1939-9375. doi: 10.1109/27.700884.

[55] P. G. Kevrekidis. Non-linear waves in lattices: Past, present, future. *IMA Journal of Applied Mathematics*, 76(3):389–423, 2011. doi: 10.1093/imamat/hxr015.

[56] A. Khelif, B. Djafari-Rouhani, J. O. Vasseur, and P. A. Deymier. Transmission and dispersion relations of perfect and defect-containing waveguide structures in phononic band gap materials. *Physical Review B*, 68(2):024302, July 2003. ISSN 0163-1829, 1095-3795. doi: 10.1103/PhysRevB.68.024302. URL https://link.aps.org/doi/10.1103/PhysRevB.68.024302.

[57] A. Khelif, A. Choujaa, S. Benchabane, B. Djafari-Rouhani, and V. Laude. Guiding and bending of acoustic waves in highly confined phononic crystal waveguides. *Applied Physics Letters*, 84(22):4400–4402, May 2004. ISSN 0003-6951. doi: 10.1063/1.1757642. URL https://aip-scitation-org.caltech.idm.oclc.org/doi/10.1063/1.1757642.

[58] B. L. Kim, C. Chong, S. Hajarolasvadi, Y. Wang, and C. Daraio. Dynamics of time-modulated, nonlinear phononic lattices. *Physical Review E*, 107(3):

034211, Mar. 2023. doi: 10.1103/PhysRevE.107.034211. URL https://link.aps.org/doi/10.1103/PhysRevE.107.034211.

[59] A. Kozyrev and D. van der Weide. Nonlinear wave propagation phenomena in left-handed transmission-line media. *IEEE Transactions on Microwave Theory and Techniques*, 53(1):238–245, Jan. 2005. ISSN 1557-9670. doi: 10.1109/TMTT.2004.839305.

[60] A. B. Kozyrev, H. Kim, and D. W. van der Weide. Parametric amplification in left-handed transmission line media. *Applied Physics Letters*, 88(26):264101, June 2006. ISSN 0003-6951. doi: 10.1063/1.2214136. URL https://aip-scitation-org.caltech.idm.oclc.org/doi/10.1063/1.2214136.

[61] N. Kruss and J. Paulose. Nondispersive one-way signal amplification in sonic metamaterials. *Physical Review Applied*, 17(2):024020, Feb. 2022. ISSN 2331-7019. doi: 10.1103/PhysRevApplied.17.024020. URL https://link.aps.org/doi/10.1103/PhysRevApplied.17.024020.

[62] M. S. Kushwaha, P. Halevi, L. Dobrzynski, and B. Djafari-Rouhani. Acoustic band structure of periodic elastic composites. *Physical Review Letters*, 71(13):2022–2025, Sept. 1993. doi: 10.1103/PhysRevLett.71.2022. URL https://link.aps.org/doi/10.1103/PhysRevLett.71.2022.

[63] A. N. Lazaridi and V. F. Nesterenko. Observation of a new type of solitary waves in a one-dimensional granular medium. *Journal of Applied Mechanics and Technical Physics*, 26(3):405–408, May 1985. ISSN 1573-8620. doi: 10.1007/BF00910379. URL https://doi.org/10.1007/BF00910379.

[64] K. Lee, J. Son, J. Park, B. Kang, W. Jeon, F. Rotermund, and B. Min. Linear frequency conversion via sudden merging of meta-atoms in time-variant metasurfaces. *Nature Photonics*, 12(12):765–773, Dec. 2018. ISSN 1749-4893. doi: 10.1038/s41566-018-0259-4. URL http://www.nature.com/articles/s41566-018-0259-4.

[65] K. Y. Lee and W. Jeon. Hierarchical phononic crystals for filtering multiple target frequencies of ultrasound. *Scientific Reports*, 10(1):8070, May 2020. ISSN 2045-2322. doi: 10.1038/s41598-020-64234-7. URL https://www.nature.com/articles/s41598-020-64234-7.

[66] S. Lee, J. Park, H. Cho, Y. Wang, B. Kim, C. Daraio, and B. Min. Parametric oscillation of electromagnetic waves in momentum band gaps of a spatiotemporal crystal. *Photonics Research*, 9(2):142, Feb. 2021. ISSN 2327-9125. doi: 10.1364/PRJ.406215. URL https://www.osapublishing.org/abstract.cfm?URI=prj-9-2-142.

[67] F. Leo, S. Coen, P. Kockaert, S.-P. Gorza, P. Emplit, and M. Haelterman. Temporal cavity solitons in one-dimensional Kerr media as bits in an all-optical buffer. *Nature Photonics*, 4(7):471–476, July 2010. ISSN 1749-

4893. doi: 10.1038/nphoton.2010.120. URL https://www.nature.com/articles/nphoton.2010.120.

[68] F. Li, C. Chong, J. Yang, P. G. Kevrekidis, and C. Daraio. Wave transmission in time- and space-variant helicoidal phononic crystals. *Physical Review E*, 90(5):053201, Nov. 2014. doi: 10.1103/PhysRevE.90.053201. URL https://link.aps.org/doi/10.1103/PhysRevE.90.053201.

[69] H. Li, A. Alù, and A. Alù. Temporal switching to extend the bandwidth of thin absorbers. *Optica*, 8(1):24–29, Jan. 2021. ISSN 2334-2536. doi: 10.1364/OPTICA.408399. URL https://www.osapublishing.org/optica/abstract.cfm?uri=optica-8-1-24.

[70] B. Liang, X. S. Guo, J. Tu, D. Zhang, and J. C. Cheng. An acoustic rectifier. *Nature Materials*, 9(12):989–992, Dec. 2010. ISSN 1476-4660. doi: 10.1038/nmat2881. URL https://www.nature.com/articles/nmat2881.

[71] S.-C. S. Lin, T. J. Huang, J.-H. Sun, and T.-T. Wu. Gradient-index phononic crystals. *Physical Review B*, 79(9):094302, Mar. 2009. ISSN 1098-0121, 1550-235X. doi: 10.1103/PhysRevB.79.094302. URL https://link.aps.org/doi/10.1103/PhysRevB.79.094302.

[72] Z. Liu, X. Zhang, Y. Mao, Y. Y. Zhu, Z. Yang, C. T. Chan, and P. Sheng. Locally resonant sonic materials. *Science*, 289 (5485):1734–1736, Sept. 2000. doi: 10.1126/science.289.5485.1734. URL https://www-science-org.caltech.idm.oclc.org/doi/full/10.1126/science.289.5485.1734.

[73] E. Lustig, S. Weimann, Y. Plotnik, Y. Lumer, M. A. Bandres, A. Szameit, and M. Segev. Photonic topological insulator in synthetic dimensions. *Nature*, 567(7748):356–360, Mar. 2019. ISSN 1476-4687. doi: 10.1038/s41586-019-0943-7. URL https://www.nature.com/articles/s41586-019-0943-7.

[74] H. Lv, X. Tian, M. Y. Wang, and D. Li. Vibration energy harvesting using a phononic crystal with point defect states. *Applied Physics Letters*, 102 (3):034103, Jan. 2013. ISSN 0003-6951. doi: 10.1063/1.4788810. URL https://aip.scitation.org/doi/full/10.1063/1.4788810.

[75] T.-X. Ma, Q.-S. Fan, C. Zhang, and Y.-S. Wang. Acoustic flatbands in phononic crystal defect lattices. *Journal of Applied Physics*, 129(14):145104, Apr. 2021. ISSN 0021-8979. doi: 10.1063/5.0040804. URL https://aip.scitation.org/doi/10.1063/5.0040804.

[76] J. Marconi, E. Riva, M. Di Ronco, G. Cazzulani, F. Braghin, and M. Ruzzene. Experimental observation of nonreciprocal band gaps in a space-time-modulated beam using a shunted piezoelectric array. *Physical Review Applied*, 13(3):031001, Mar. 2020. doi: 10.1103/

PhysRevApplied.13.031001. URL https://link.aps.org/doi/10.1103/PhysRevApplied.13.031001.

[77] R. Martínez-Sala, J. Sancho, J. V. Sánchez, V. Gómez, J. Llinares, and F. Meseguer. Sound attenuation by sculpture. *Nature*, 378(6554):241–241, Nov. 1995. ISSN 1476-4687. doi: 10.1038/378241a0. URL https://www.nature.com/articles/378241a0.

[78] A. B. Matsko, A. A. Savchenkov, and L. Maleki. On excitation of breather solitons in an optical microresonator. *Optics Letters*, 37(23):4856–4858, Dec. 2012. ISSN 1539-4794. doi: 10.1364/OL.37.004856. URL https://opg.optica.org/ol/abstract.cfm?uri=ol-37-23-4856.

[79] A. Mekis, S. Fan, and J. D. Joannopoulos. Bound states in photonic crystal waveguides and waveguide bends. *Physical Review B*, 58(8):4809–4817, Aug. 1998. ISSN 0163-1829, 1095-3795. doi: 10.1103/PhysRevB.58.4809. URL https://link.aps.org/doi/10.1103/PhysRevB.58.4809.

[80] J. T. Mendonça and P. K. Shukla. Time refraction and time reflection: Two basic concepts. *Physica Scripta*, 65(2):160–163, Jan. 2002. ISSN 0031-8949, 1402-4896. doi: 10.1238/Physica.Regular.065a00160. URL https://iopscience.iop.org/article/10.1238/Physica.Regular.065a00160.

[81] G. A. Menendez and B. Maes. Time reflection and refraction of graphene plasmons at a temporal discontinuity. *Optics Letters*, 42(23):5006, Dec. 2017. ISSN 0146-9592, 1539-4794. doi: 10.1364/OL.42.005006. URL https://www.osapublishing.org/abstract.cfm?URI=ol-42-23-5006.

[82] F. Mitschke. Treatment with Ray Optics. In F. Mitschke, editor, *Fiber Optics: Physics and Technology*, pages 17–28. Springer, Berlin, Heidelberg, 2016. ISBN 978-3-662-52764-1. doi: 10.1007/978-3-662-52764-1_2. URL https://doi.org/10.1007/978-3-662-52764-1_2.

[83] A. Molinari and C. Daraio. Stationary shocks in periodic highly nonlinear granular chains. *Physical Review E*, 80(5):056602, Nov. 2009. doi: 10.1103/PhysRevE.80.056602. URL https://link.aps.org/doi/10.1103/PhysRevE.80.056602.

[84] J. Moosburger, M. Kamp, A. Forchel, S. Olivier, H. Benisty, C. Weisbuch, and U. Oesterle. Enhanced transmission through photonic-crystal-based bent waveguides by bend engineering. *Applied Physics Letters*, 79(22):3579–3581, Nov. 2001. ISSN 0003-6951, 1077-3118. doi: 10.1063/1.1421087. URL http://aip.scitation.org/doi/10.1063/1.1421087.

[85] F. Morgenthaler. Velocity modulation of electromagnetic waves. *IRE Transactions on Microwave Theory and Techniques*, 6(2):167–172, Apr. 1958. ISSN 2331-088X. doi: 10.1109/TMTT.1958.1124533.

[86] H. Nassar, H. Chen, A. N. Norris, M. R. Haberman, and G. L. Huang. Non-reciprocal wave propagation in modulated elastic metamaterials. *Proceedings of the Royal Society A: Mathematical, Physical and Engineering Science*, 473(2202):20170188, June 2017. ISSN 1364-5021, 1471-2946. doi: 10.1098/rspa.2017.0188. URL http://rspa.royalsocietypublishing.org/lookup/doi/10.1098/rspa.2017.0188.

[87] H. Nassar, X. C. Xu, A. N. Norris, and G. L. Huang. Modulated phononic crystals: Non-reciprocal wave propagation and Willis materials. *Journal of the Mechanics and Physics of Solids*, 101:10–29, Jan. 2017. ISSN 0022-5096. doi: 10.1016/j.jmps.2017.01.010. URL http://www.sciencedirect.com/science/article/pii/S0022509616308997.

[88] H. Nassar, B. Yousefzadeh, R. Fleury, M. Ruzzene, A. Alù, C. Daraio, A. N. Norris, G. Huang, and M. R. Haberman. Nonreciprocity in acoustic and elastic materials. *Nature Reviews Materials*, pages 1–19, July 2020. ISSN 2058-8437. doi: 10.1038/s41578-020-0206-0. URL https://www.nature.com/articles/s41578-020-0206-0.

[89] A. H. Nayfeh and D. T. Mook. *Nonlinear Oscillations*. Wiley and Sons, Weihheim, Germany, 2004.

[90] V. F. Nesterenko. Propagation of nonlinear compression pulses in granular media. *Journal of Applied Mechanics and Technical Physics*, 24(5):733–743, Sept. 1983. ISSN 1573-8620. doi: 10.1007/BF00905892. URL https://doi.org/10.1007/BF00905892.

[91] X. Ni, K. Chen, M. Weiner, D. J. Apigo, C. Prodan, A. Alù, E. Prodan, and A. B. Khanikaev. Observation of Hofstadter butterfly and topological edge states in reconfigurable quasi-periodic acoustic crystals. *Communications Physics*, 2(1):1–7, June 2019. ISSN 2399-3650. doi: 10.1038/s42005-019-0151-7. URL https://www.nature.com/articles/s42005-019-0151-7.

[92] A. Nishida, N. Yugami, T. Higashiguchi, T. Otsuka, F. Suzuki, M. Nakata, Y. Sentoku, and R. Kodama. Experimental observation of frequency up-conversion by flash ionization. *Applied Physics Letters*, 101(16):161118, Oct. 2012. ISSN 0003-6951, 1077-3118. doi: 10.1063/1.4755843. URL http://aip.scitation.org/doi/10.1063/1.4755843.

[93] V. Pacheco-Peña and N. Engheta. Antireflection temporal coatings. *Optica*, 7(4):323–331, Apr. 2020. ISSN 2334-2536. doi: 10.1364/OPTICA.381175. URL https://www-osapublishing-org.caltech.idm.oclc.org/optica/abstract.cfm?uri=optica-7-4-323.

[94] R. Paghousi and K. Fasihi. High-contrast controllable switching based on polystyrene nonlinear cavities in 2D hole-type photonic crystals. *Optics Communications*, 415:101–106, May 2018. ISSN 0030-4018. doi: 10.

1016/j.optcom.2018.01.035. URL https://www.sciencedirect.com/science/article/pii/S0030401818300488.

[95] Y. Pan, M.-I. Cohen, and M. Segev. Superluminal k-gap solitons in nonlinear photonic time-crystals, Aug. 2022. URL http://arxiv.org/abs/2208.09220.

[96] D. A. Powell, I. V. Shadrivov, and Y. S. Kivshar. Multistability in nonlinear left-handed transmission lines. *Applied Physics Letters*, 92(26):264104, June 2008. ISSN 0003-6951. doi: 10.1063/1.2955531. URL https://aip-scitation-org.caltech.idm.oclc.org/doi/10.1063/1.2955531.

[97] D. A. Powell, I. V. Shadrivov, and Y. S. Kivshar. Asymmetric parametric amplification in nonlinear left-handed transmission lines. *Applied Physics Letters*, 94(8):084105, Feb. 2009. ISSN 0003-6951. doi: 10.1063/1.3089842. URL https://aip-scitation-org.caltech.idm.oclc.org/doi/10.1063/1.3089842.

[98] C. Qiu, X. Zhang, and Z. Liu. Far-field imaging of acoustic waves by a two-dimensional sonic crystal. *Physical Review B*, 71(5):054302, Feb. 2005. ISSN 1098-0121, 1550-235X. doi: 10.1103/PhysRevB.71.054302. URL https://link.aps.org/doi/10.1103/PhysRevB.71.054302.

[99] D. Ramaccia, A. Toscano, and F. Bilotti. Light propagation through metamaterial temporal slabs: Reflection, refraction, and special cases. *Optics Letters*, 45(20):5836, Oct. 2020. ISSN 0146-9592, 1539-4794. doi: 10.1364/OL.402856. URL https://www.osapublishing.org/abstract.cfm?URI=ol-45-20-5836.

[100] D. Ramaccia, A. Alù, A. Toscano, and F. Bilotti. Temporal multilayer structures for designing higher-order transfer functions using time-varying metamaterials. *Applied Physics Letters*, 118(10):101901, Mar. 2021. ISSN 0003-6951, 1077-3118. doi: 10.1063/5.0042567. URL https://aip.scitation.org/doi/10.1063/5.0042567.

[101] J. R. Reyes-Ayona and P. Halevi. Observation of genuine wave vector (k or β) gap in a dynamic transmission line and temporal photonic crystals. *Applied Physics Letters*, 107(7):074101, Aug. 2015. ISSN 0003-6951, 1077-3118. doi: 10.1063/1.4928659. URL http://aip.scitation.org/doi/10.1063/1.4928659.

[102] B. Rostami-Dogolsara, M. K. Moravvej-Farshi, and F. Nazari. Acoustic add-drop filters based on phononic crystal ring resonators. *Physical Review B*, 93(1):014304, Jan. 2016. doi: 10.1103/PhysRevB.93.014304. URL https://link.aps.org/doi/10.1103/PhysRevB.93.014304.

[103] K. W. Sandusky, J. B. Page, and K. E. Schmidt. Stability and motion of intrinsic localized modes in nonlinear periodic lattices. *Physical Review*

B, 46(10):6161–6168, Sept. 1992. doi: 10.1103/PhysRevB.46.6161. URL https://link.aps.org/doi/10.1103/PhysRevB.46.6161.

[104] F. Santibanez, R. Munoz, A. Caussarieu, S. Job, and F. Melo. Experimental evidence of solitary wave interaction in Hertzian chains. *Physical Review E*, 84(2):026604, Aug. 2011. doi: 10.1103/PhysRevE.84.026604. URL https://link.aps.org/doi/10.1103/PhysRevE.84.026604.

[105] M. Sigalas and E. Economou. Elastic and acoustic wave band structure. *Journal of Sound and Vibration*, 158(2):377–382, Oct. 1992. ISSN 0022460X. doi: 10.1016/0022-460X(92)90059-7. URL https://linkinghub.elsevier.com/retrieve/pii/0022460X92900597.

[106] S. C. Sinha. On the analysis of time-periodic nonlinear dynamical systems. *Sadhana*, 22(3):411–434, June 1997. ISSN 0973-7677. doi: 10.1007/BF02744481. URL https://doi.org/10.1007/BF02744481.

[107] M. SoljaČiĆ and J. D. Joannopoulos. Enhancement of nonlinear effects using photonic crystals. *Nature Materials*, 3(4):211–219, Apr. 2004. ISSN 1476-4660. doi: 10.1038/nmat1097. URL https://www.nature.com/articles/nmat1097.

[108] M. Soljačić, M. Ibanescu, S. G. Johnson, and Y. Fink. Optimal bistable switching in nonlinear photonic crystals. *Physical Review E*, 66(5):055601, Nov. 2002. doi: 10.1103/PhysRevE.66.055601. URL https://link.aps.org/doi/10.1103/PhysRevE.66.055601.

[109] A. Spadoni and C. Daraio. Generation and control of sound bullets with a nonlinear acoustic lens. *Proceedings of the National Academy of Sciences*, 107(16):7230–7234, Apr. 2010. doi: 10.1073/pnas.1001514107. URL https://www.pnas.org/doi/full/10.1073/pnas.1001514107.

[110] L. Stefanini, S. Yin, D. Ramaccia, A. Alù, A. Toscano, and F. Bilotti. Temporal interfaces by instantaneously varying boundary conditions. *Physical Review B*, 106(9):094312, Sept. 2022. ISSN 2469-9950, 2469-9969. doi: 10.1103/PhysRevB.106.094312. URL https://link.aps.org/doi/10.1103/PhysRevB.106.094312.

[111] W. P. Su, J. R. Schrieffer, and A. J. Heeger. Solitons in polyacetylene. *Physical Review Letters*, 42(25):1698–1701, June 1979. doi: 10.1103/PhysRevLett.42.1698. URL https://link.aps.org/doi/10.1103/PhysRevLett.42.1698.

[112] B. I. Swanson, J. A. Brozik, S. P. Love, G. F. Strouse, A. P. Shreve, A. R. Bishop, W.-Z. Wang, and M. I. Salkola. Observation of intrinsically localized modes in a discrete low-dimensional material. *Physical Review Letters*, 82(16):3288–3291, Apr. 1999. doi: 10.1103/PhysRevLett.82.3288. URL https://link.aps.org/doi/10.1103/PhysRevLett.82.3288.

[113] N. Swinteck, S. Matsuo, K. Runge, J. O. Vasseur, P. Lucas, and P. A. Deymier. Bulk elastic waves with unidirectional backscattering-immune topological states in a time-dependent superlattice. *Journal of Applied Physics*, 118(6): 063103, Aug. 2015. ISSN 0021-8979, 1089-7550. doi: 10.1063/1.4928619. URL http://aip.scitation.org/doi/10.1063/1.4928619.

[114] G. Theocharis, M. Kavousanakis, P. G. Kevrekidis, C. Daraio, M. A. Porter, and I. G. Kevrekidis. Localized breathing modes in granular crystals with defects. *Physical Review E*, 80(6):066601, Dec. 2009. doi: 10.1103/PhysRevE.80.066601. URL https://link.aps.org/doi/10.1103/PhysRevE.80.066601.

[115] G. Theocharis, N. Boechler, P. G. Kevrekidis, S. Job, M. A. Porter, and C. Daraio. Intrinsic energy localization through discrete gap breathers in one-dimensional diatomic granular crystals. *Physical Review E*, 82(5):056604, Nov. 2010. doi: 10.1103/PhysRevE.82.056604. URL https://link.aps.org/doi/10.1103/PhysRevE.82.056604.

[116] Z. Tian and L. Yu. Rainbow trapping of ultrasonic guided waves in chirped phononic crystal plates. *Scientific Reports*, 7(1):40004, Jan. 2017. ISSN 2045-2322. doi: 10.1038/srep40004. URL https://www.nature.com/articles/srep40004.

[117] P. K. Tien and H. Suhl. A traveling-wave ferromagnetic amplifier. *Proceedings of the IRE*, 46(4):700–706, Apr. 1958. ISSN 2162-6634. doi: 10.1109/JRPROC.1958.286770.

[118] D. Torrent, W. J. Parnell, and A. N. Norris. Loss compensation in time-dependent elastic metamaterials. *Physical Review B*, 97(1):014105, Jan. 2018. ISSN 2469-9950, 2469-9969. doi: 10.1103/PhysRevB.97.014105. URL https://link.aps.org/doi/10.1103/PhysRevB.97.014105.

[119] M. Torres, F. R. Montero de Espinosa, and J. L. Aragón. Ultrasonic wedges for elastic wave bending and splitting without requiring a full band gap. *Physical Review Letters*, 86(19):4282–4285, May 2001. ISSN 0031-9007, 1079-7114. doi: 10.1103/PhysRevLett.86.4282. URL https://link.aps.org/doi/10.1103/PhysRevLett.86.4282.

[120] G. Trainiti and M. Ruzzene. Non-reciprocal elastic wave propagation in spatiotemporal periodic structures. *New Journal of Physics*, 18(8):083047, Aug. 2016. ISSN 1367-2630. doi: 10.1088/1367-2630/18/8/083047. URL https://iopscience.iop.org/article/10.1088/1367-2630/18/8/083047/meta.

[121] G. Trainiti, Y. Xia, J. Marconi, G. Cazzulani, A. Erturk, and M. Ruzzene. Time-periodic stiffness modulation in elastic metamaterials for selective wave filtering: Theory and experiment. *Physical Review Letters*, 122(12):124301, Mar. 2019. ISSN 0031-9007, 1079-7114. doi: 10.1103/PhysRevLett.122.

124301. URL https://link.aps.org/doi/10.1103/PhysRevLett.122.124301.

[122] J. O. Vasseur, P. A. Deymier, B. Chenni, B. Djafari-Rouhani, L. Dobrzynski, and D. Prevost. Experimental and theoretical evidence for the existence of absolute acoustic band gaps in two-dimensional solid phononic crystals. *Physical Review Letters*, 86(14):3012–3015, Apr. 2001. doi: 10.1103/PhysRevLett.86.3012. URL https://link.aps.org/doi/10.1103/PhysRevLett.86.3012.

[123] P. Wang, L. Lu, and K. Bertoldi. Topological phononic crystals with one-way elastic edge waves. *Physical Review Letters*, 115(10):104302, Sept. 2015. doi: 10.1103/PhysRevLett.115.104302. URL https://link.aps.org/doi/10.1103/PhysRevLett.115.104302.

[124] Y. Wang, B. Yousefzadeh, H. Chen, H. Nassar, G. Huang, and C. Daraio. Observation of nonreciprocal wave propagation in a dynamic phononic lattice. *Physical Review Letters*, 121(19):194301, Nov. 2018. ISSN 0031-9007, 1079-7114. doi: 10.1103/PhysRevLett.121.194301. URL https://link.aps.org/doi/10.1103/PhysRevLett.121.194301.

[125] H. G. Winful, J. H. Marburger, and E. Garmire. Theory of bistability in nonlinear distributed feedback structures. *Applied Physics Letters*, 35(5):379–381, Sept. 1979. ISSN 0003-6951. doi: 10.1063/1.91131. URL https://aip-scitation-org.caltech.idm.oclc.org/doi/10.1063/1.91131.

[126] B. Xu and N.-B. Ming. Experimental observations of bistability and instability in a two-dimensional nonlinear optical superlattice. *Physical Review Letters*, 71(24):3959–3962, Dec. 1993. doi: 10.1103/PhysRevLett.71.3959. URL https://link.aps.org/doi/10.1103/PhysRevLett.71.3959.

[127] X. Xu, Q. Wu, H. Chen, H. Nassar, Y. Chen, A. Norris, M. R. Haberman, and G. Huang. Physical observation of a robust acoustic pumping in waveguides with dynamic boundary. *Physical Review Letters*, 125(25):253901, Dec. 2020. doi: 10.1103/PhysRevLett.125.253901. URL https://link.aps.org/doi/10.1103/PhysRevLett.125.253901.

[128] H. Xue, Y. Yang, and B. Zhang. Topological acoustics. *Nature Reviews Materials*, 7(12):974–990, Dec. 2022. ISSN 2058-8437. doi: 10.1038/s41578-022-00465-6. URL https://www.nature.com/articles/s41578-022-00465-6.

[129] E. Yablonovitch. Inhibited spontaneous emission in solid-state physics and electronics. *Physical Review Letters*, 58(20):2059–2062, May 1987. doi: 10.1103/PhysRevLett.58.2059. URL https://link.aps.org/doi/10.1103/PhysRevLett.58.2059.

[130] S. Yang, J. H. Page, Z. Liu, M. L. Cowan, C. T. Chan, and P. Sheng. Focusing of sound in a 3D phononic crystal. *Physical Review Letters*, 93(2): 024301, July 2004. ISSN 0031-9007, 1079-7114. doi: 10.1103/PhysRevLett.93.024301. URL https://link.aps.org/doi/10.1103/PhysRevLett.93.024301.

[131] Z. Yang, E. Lustig, G. Harari, Y. Plotnik, Y. Lumer, M. A. Bandres, and M. Segev. Mode-locked topological insulator laser utilizing synthetic dimensions. *Physical Review X*, 10(1):011059, Mar. 2020. doi: 10.1103/PhysRevX.10.011059. URL https://link.aps.org/doi/10.1103/PhysRevX.10.011059.

[132] J. Yin, M. Ruzzene, J. Wen, D. Yu, L. Cai, and L. Yue. Band transition and topological interface modes in 1D elastic phononic crystals. *Scientific Reports*, 8(1):6806, May 2018. ISSN 2045-2322. doi: 10.1038/s41598-018-24952-5. URL https://www.nature.com/articles/s41598-018-24952-5.

[133] S. Yin and A. Alù. Efficient phase conjugation in a space-time leaky waveguide. *ACS Photonics*, page acsphotonics.1c01836, Feb. 2022. ISSN 2330-4022, 2330-4022. doi: 10.1021/acsphotonics.1c01836. URL https://pubs.acs.org/doi/10.1021/acsphotonics.1c01836.

[134] M. Yu, J. K. Jang, Y. Okawachi, A. G. Griffith, K. Luke, S. A. Miller, X. Ji, M. Lipson, and A. L. Gaeta. Breather soliton dynamics in microresonators. *Nature Communications*, 8(1):14569, Feb. 2017. ISSN 2041-1723. doi: 10.1038/ncomms14569. URL https://www.nature.com/articles/ncomms14569.

[135] S.-Y. Yu, C. He, Z. Wang, F.-K. Liu, X.-C. Sun, Z. Li, H.-Z. Lu, M.-H. Lu, X.-P. Liu, and Y.-F. Chen. Elastic pseudospin transport for integratable topological phononic circuits. *Nature Communications*, 9(1):3072, Aug. 2018. ISSN 2041-1723. doi: 10.1038/s41467-018-05461-5. URL https://www.nature.com/articles/s41467-018-05461-5.

[136] Y. Yu, G. Michetti, M. Pirro, A. Kord, D. L. Sounas, Z. Xiao, C. Cassella, A. Alù, and M. Rinaldi. Radio frequency magnet-free circulators based on spatiotemporal modulation of surface acoustic wave filters. *IEEE Transactions on Microwave Theory and Techniques*, 67(12):4773–4782, Dec. 2019. ISSN 1557-9670. doi: 10.1109/TMTT.2019.2943291.

[137] L. Yuan, Q. Lin, M. Xiao, and S. Fan. Synthetic dimension in photonics. *Optica*, 5(11):1396, Nov. 2018. ISSN 2334-2536. doi: 10.1364/OPTICA.5.001396. URL https://www.osapublishing.org/abstract.cfm?URI=optica-5-11-1396.

[138] B. Zaghari, E. Rustighi, and M. G. Tehrani. An experimentally validated parametrically excited vibration energy harvester with time-varying stiffness.

In N. G. Meyendorf, editor, *Smart Materials and Nondestructive Evaluation for Energy Systems 2015*, volume 9439, page 94390S. International Society for Optics and Photonics, SPIE, 2015. doi: 10.1117/12.2084219. URL https://doi.org/10.1117/12.2084219.

[139] J. Zhang, W. R. Donaldson, and G. P. Agrawal. Impact of the boundary's sharpness on temporal reflection in dispersive media. *Optics Letters*, 46 (16):4053, Aug. 2021. ISSN 0146-9592, 1539-4794. doi: 10.1364/OL.432180. URL https://www.osapublishing.org/abstract.cfm?URI=ol-46-16-4053.

[140] X. H. Zhang, Z. G. Qu, X. C. He, and D. L. Lu. Experimental study on the sound absorption characteristics of continuously graded phononic crystals. *AIP Advances*, 6(10):105205, Oct. 2016. ISSN 2158-3226. doi: 10.1063/1.4965923. URL http://aip.scitation.org/doi/10.1063/1.4965923.

[141] J. Zhao, Q. Wang, X. Wang, W. Yuan, Y. Huang, S. Chen, A. Riaud, and J. Zhou. On-chip valley phononic crystal plates with graded topological interface. *International Journal of Mechanical Sciences*, 227: 107460, Aug. 2022. ISSN 0020-7403. doi: 10.1016/j.ijmecsci.2022.107460. URL https://www.sciencedirect.com/science/article/pii/S0020740322003630.

[142] X. Zhou, X. Liu, and G. Hu. Elastic metamaterials with local resonances: An overview. *Theoretical and Applied Mechanics Letters*, 2(4):041001, 2012. ISSN 20950349. doi: 10.1063/2.1204101. URL https://linkinghub.elsevier.com/retrieve/pii/S2095034915301586.

[143] Y. Zhou, M. Z. Alam, M. Karimi, J. Upham, O. Reshef, C. Liu, A. E. Willner, and R. W. Boyd. Broadband frequency translation through time refraction in an epsilon-near-zero material. *Nature Communications*, 11(1): 2180, Dec. 2020. ISSN 2041-1723. doi: 10.1038/s41467-020-15682-2. URL http://www.nature.com/articles/s41467-020-15682-2.

[144] J. Zhu, Y. Chen, X. Zhu, F. J. Garcia-Vidal, X. Yin, W. Zhang, and X. Zhang. Acoustic rainbow trapping. *Scientific Reports*, 3(1):1728, Apr. 2013. ISSN 2045-2322. doi: 10.1038/srep01728. URL https://www.nature.com/articles/srep01728.

Chapter 2

METHODS

2.1 Experimental Setup

The experimental setup used throughout the studies presented in this thesis is a finite, one-dimensional phononic lattice with time-varying grounding stiffnesses. The temporal control of grounding stiffness can achieve both boundary-like, in which the single dispersion band changes discontinuously in time, and space- and time-periodic modulations, which open band gaps in the acoustic band.

Phononic lattice

The lattice setup, shown in Fig. 2.1(a), was originally developed by Wang and coauthors [2]. It is composed of $N = 12$ ring magnets (K&J Magnetic, Inc., P/N R848), mounted with sleeve bearings (McMaster-Carr P/N 6377K2) on a low-friction cylindrical rod (McMaster-Carr P/N 8543K28). The magnets are arranged with opposite polarity so that adjacent ring magnets repel, and the boundaries are fixed. This chain of repelling magnets acts effectively as a spring-mass chain with nonlinear coupling stiffnesses. The spring-mass model is depicted in Fig. 2.1(b) with masses m, coupling stiffness k_c, time-variable grounding stiffnesses $k_g(t)$, and viscous damping coefficient c, which is used to model dissipative forces in the model. Electromagnetic coils (APW Company SKU: FC-6489) positioned concentrically around individual ring magnets provide a restoring force proportional to the applied current and the relative displacement of the magnet from the center of the coil. When the coils are fixed around the equilibrium point of the magnets, their restoring force act as an effective grounding stiffness. The first free mass on one end of the lattice has a coil slightly offset from equilibrium, which provides the driving input force. Then, the eight center ring magnets have modulating coils (as opposed to all of the remaining free magnets) so that the symmetry of the system is preserved.

The primary challenge for the studies presented here is to obtain measurements of the full velocity field response of the lattice in the different modulation cases in order to reconstruct the dispersion relation of the lattice. The procedure is explained in detail in the following subsection. Attempts to increase the total length of the system from 12 to 24 masses were limited by strong dissipation and the supported weight by the cylindrical rod. Decreasing the lattice constant (the equilibrium spacing between

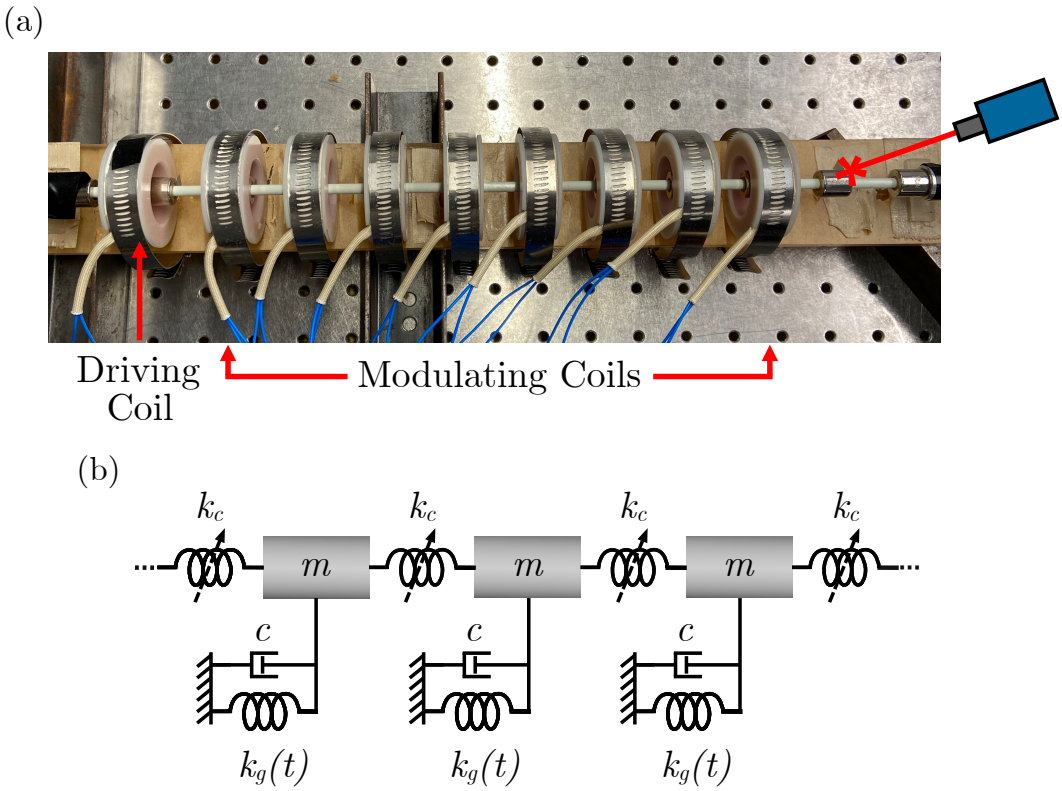

Figure 2.1: Velocity measurement (adapted from [1]). **(a)** Photo of the experimental apparatus, with electromagnetic coils corresponding to grounding springs (modulating coils) and ring magnets inside each coil (not fully visible) sliding freely on a low-friction rod; depiction of position of LDV velocity measurement. **(b)** Schematic of the mass-spring lattice model with nonlinear coupling stiffness k_c, time-varying grounding stiffness $k_g(t)$, and viscous damping c.

the masses) also could not combat dissipation because the increased repelling force and effective spring constant between adjacent masses become too large compared to the forces applied by the electromagnetic coils. Since the magnetic repelling force is approximately a dipole-dipole relationship, there is a dramatic increase in the effective stiffness for small decreases in the lattice constant. This is discussed further in Section 2.2. Additional designs for roller bearings were limited by the available magnet and coil geometries. Ultimately, many designs for reducing friction and dissipation did not see significant improvements or led to secondary issues. In the end, we focused on accurately modeling the dissipative forces, which is discussed in detail in Section 2.2. Future work will benefit from revisiting the possibility of a longer experimental lattice; nonetheless, we were successful in implementing full velocity field measurements, which were crucial not only to

dispersion reconstruction but also general spectral analysis of the response of the lattice.

Measurement procedure

The measurement of waves and vibrations in the phononic lattice is essentially the same for all types of modulations. A schematic of this process and the data acquisition are shown in Fig. 2.2. Input voltage signals, either harmonic or spectrally concentrated wavepackets of driving frequency f_{drive}, are generated by an arbitrary function generator (Aglient 33220A), then amplified (Topping TP30-MK2) before being applied to the offset driving electromagnetic coil, applying a driving force to the input mass. The sync out signal of the driving function generator is connected to the modulation function generator to synchronize the time-varying stiffness $k_g(t)$ and the oscilloscope to synchronize data acquisition. The modulating function generator, the output of which is optionally triggered by the driving function generator, supplies the time-varying grounding stiffness voltage signal, which is also amplified (Accel Instruments TS250-2) before being applied to the modulating coils in parallel. Particle velocities are measured by a laser Doppler vibrometer (Polytec CLV-2534), and the data is recorded by an oscilloscope (Tektronix DPO 3034), which is also recording and optionally triggered by the driving function generator. Although the ring magnets are largely obstructed by the surrounding electromagnetic coils, there is at least one clear line of sight to each magnet through the coils, which means the LDV can be aimed nearly along the along the axis of the supporting rod from one end of the lattice. This positioning is roughly shown by the cartoon on the right side of Fig. 2.1(a).

Synchronization of the driving, modulation, and data acquisition is crucial. Since the LDV can only measure one particle velocity at a time, it is necessary to repeat the measurement of a given signal and modulation at every mass in order to obtain the full velocity field. Therefore, particularly for non-harmonic modulations such as a temporal boundary, the time delay of the modulation from the input driving signal, as well as the start time of the data acquisition, must be identical every time. Several experiments, such as the determination of dynamic stability for given modulation parameters, only require the application of the modulation signal, a manually applied impulse or perturbation from quiescent conditions, and observation of the final steady state of the system at only one spatial location. In general, however, time-synchronized measurments are required.

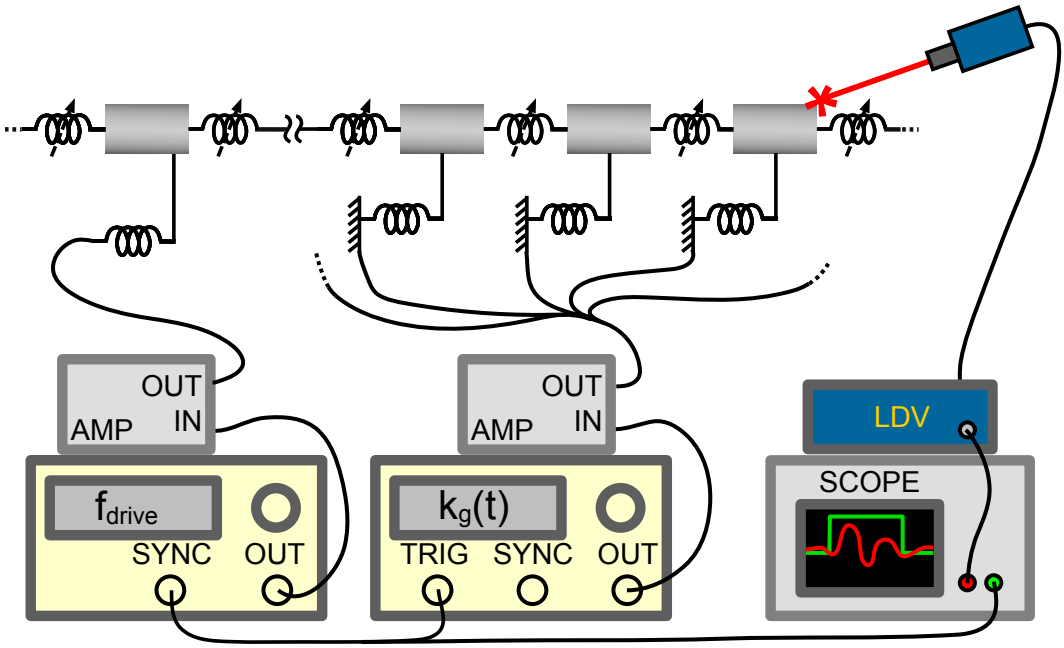

Figure 2.2: Schematic of measurement and data acquisition.

2.2 Lattice Model and Numerical Simulation

The model description in this section is adapted from [1].

The lattice is modeled as a discrete spring-mass chain, wherein the equation of motion for the n^{th} mass (ring magnet) with displacement u_n may be written as [2]

$$m\frac{d^2u_n}{dt^2} + k_g(t)u_n + F_{loss,n} + F_{mag,n} = \delta_{2,n}A_{dr}\cos\left(2\pi f_{dr}t\right), \tag{2.1}$$

for $n = 1$ to N, with fixed boundary conditions $u_1(t) = u_N(t) = 0$. All ring magnets have uniform mass m. The variable grounding stiffness, $k_g(t)$, acts uniformly on every individual mass. The dissipative forces are represented by $F_{loss,n}$, and $F_{mag,n}$ is the coupling force acting on the n^{th} mass due to repulsive force between neighboring ring magnets. The driving input amplitude and frequency are given by $A_{dr}([A_{dr}] = \text{N})$ and $f_{dr}([f_{dr}] = \text{Hz})$, respectively. The Kronecker delta, $\delta_{2,n}$, acts so that the input forcing applies only to mass $n = 2$.

A modulation signal voltage applied to the electromagnetic coils induces a harmonic grounding stiffness modulation of the form

$$k_g(t) = \delta_{j,n}A_{mod}g(t) \tag{2.2}$$

with amplitude A_{mod} $([A_{mod}] = \text{N m}^{-1})$ for some normalized modulation $g(t)$. The Kronecker delta index $j = 3$ to $N - 2$ so that the modulation acts only on masses

$n = 3$ to $N - 2$, labeled as modulating coils in Fig. 2.1(a). The amplitudes A_{dr} and A_{mod} are determined using empirical relations between applied voltage and resultant current in the coils and measurements of the reaction force exerted by the coils on the concentric ring magnets as a function of displacement from equilibrium position for a given current [2]. The stiffness (in N m^{-1}) of each coil is approximately $A_{mod} \approx 81A_V$ for applied voltages $A_V < 0.575$ V, and $A_{mod} \approx 39 + 14A_V$ for voltages $A_V \geq 0.575$ V, when using the Topping TP30-MK2 amplifier. For the Accel Instruments TS250-2 amplifier, the relationship is $A_{mod} \approx 50A_V$. The driving is offset from the equilibrium position of the driven mass by 7.5 mm, therefore the driving amplitude A_{dr} (in N) is obtained by multiplying the previous stiffness-voltage relations by the offset.

Dissipative forces are modeled phenomenologically with a viscous damping term,

$$F_{loss,n} = c\frac{du_n}{dt} \tag{2.3}$$

where the damping coefficient c ($[c]$ = N s m^{-1}) is determined empirically. Typically, dissipation might be estimated using a similar method to a cavity ring-down measurement, determining an exponential decay constant in time as free oscillations of the lattice decay; however, because strong dissipation causes rapid decay of free oscillations in time (on the order of one period), it is better for this system to estimate the damping constant by considering spatial decay. We measure and simulate short bursts of monochromatic waves excited from the driving coil traveling through the lattice for many frequencies spanning the pass band of the lattice. We then compute the norms of the error between the simulated and experimental velocity amplitude envelopes. The simulation is repeated for a range of values of the damping coefficient c, so the norm of the errors across all driving frequencies is determined as a function of the damping coefficient. The value of c that minimizes the magnitude of this total error is used in all analytical and numerical modeling. The coefficient is modeled a constant, but it performs well for all frequencies. A representative example of the measured velocity envelope with the simulated enveloped using the optimal value of $c = 0.15$ N s m^{-1} is shown in Fig. 2.3(a).

The coupling force term is defined using the repulsive magnetic force $P(x)$ between neighboring masses, where $P(x)$ is a function of the center-to-center distance x (m) between masses. The measured force-distance relation between neighboring masses is fit with a dipole-dipole approximation given by

$$P_{dipole}(x) = k_{dipole}x^{-\alpha} + P_{0,dipole}. \tag{2.4}$$

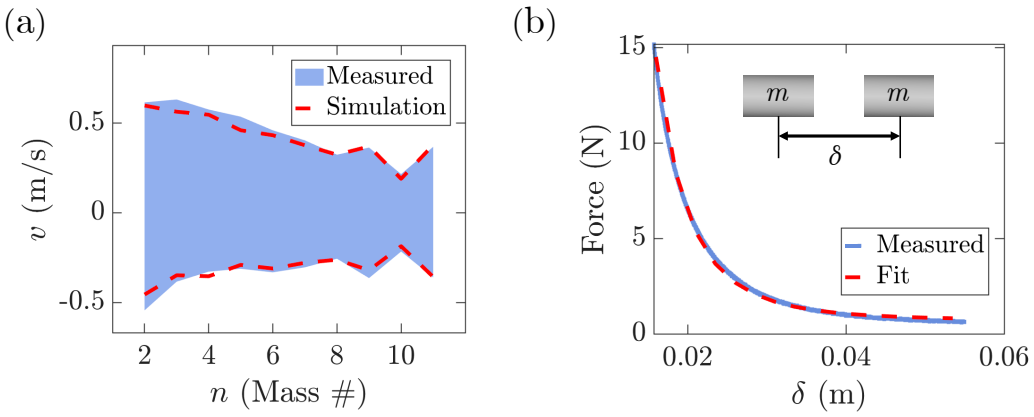

Figure 2.3: Fit of damping and force-distance relationship (adapted from [1]). **(a)** Measured (blue shaded region) and numerically simulated (red dashed lines) nodal velocity envelope, used for viscous damping parameter fitting by matching spatial decay. **(b)** Force-distance measurement (blue line) [2] and fit (red dashed line) of repulsive magnetic force between neighboring masses.

The measured force-distance relationship and dipole-dipole fit values are shown in Fig. 2.3(b). If the displacement amplitude of the masses is small relative to the equilibrium distance between adjacent masses, it is useful to employ a linear approximation using the Taylor expansion of the above expression about the equilibrium displacement

$$P_{linear}(x) = k_{linear}x, \tag{2.5}$$

where $k_{linear} = P'_{dipole}(a)$, where a is the equilibrium distance between adjacent masses. Thus the total coupling force on a given mass is calculated using its displacement u_n, the displacement of the neighboring masses $u_{n\pm1}$ as follows

$$F_{mag,n} = P\left(a - u_n + u_{n+1}\right) - P\left(a - u_{n-1} + u_n\right), \tag{2.6}$$

where P can be given by either P_{dipole} or P_{linear}.

Numerical simulations are performed by solving Eq. (2.1) using a variable step fourth order Runge-Kutta method implementd with MATLAB ode45, which can be performed for arbitrary driving and modulation waveform and amplitude. Linear or nonlinear force-distance relation $P(x)$ are used for modeling coupling stiffness to validate theoretical linear dynamics or reproduce the real lattice dynamics, respectively. Measured parameters, such as mass and lattice constant, are fixed, and the fit damping coefficient is constant except when studying a longer lattice numerically in Section 3.7. Two comparisons of numerical simulation and measured lattice

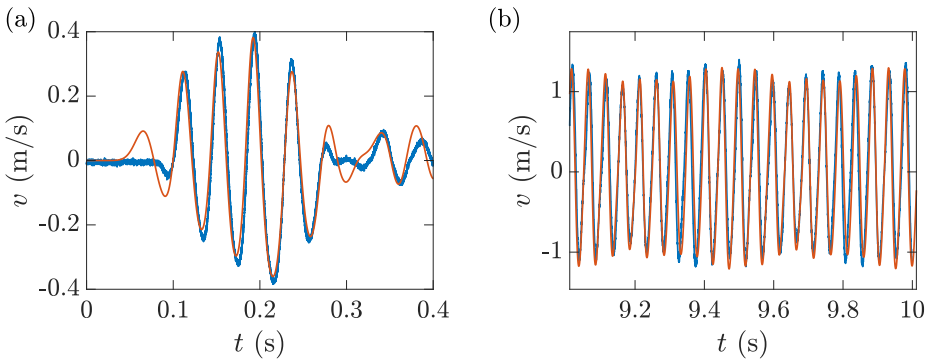

Figure 2.4: Numerical simulation of lattice response. **(a),(b)** Examples of experiment (blue) and simulation (orange) of transient (a) and steady state (b) responses of lattice.

response are shown in Fig. 2.4. Fig. 2.4(a) shows one of the transient responses of the lattice to a short burst of sine waves, used to fit the damping coefficient and measure dispersion in the lattice. Fig. 2.4(b) shows the steady state response under large amplitude harmonic modulation, as studied in Section 4.5.

References

[1] B. L. Kim, C. Chong, S. Hajarolasvadi, Y. Wang, and C. Daraio. Dynamics of time-modulated, nonlinear phononic lattices. *Physical Review E*, 107(3): 034211, Mar. 2023. doi: 10.1103/PhysRevE.107.034211. URL `https://link.aps.org/doi/10.1103/PhysRevE.107.034211`.

[2] Y. Wang, B. Yousefzadeh, H. Chen, H. Nassar, G. Huang, and C. Daraio. Observation of nonreciprocal wave propagation in a dynamic phononic lattice. *Physical Review Letters*, 121(19):194301, Nov. 2018. ISSN 0031-9007, 1079-7114. doi: 10.1103/PhysRevLett.121.194301. URL `https://link.aps.org/doi/10.1103/PhysRevLett.121.194301`.

Chapter 3

TEMPORAL REFRACTION

Research presented in this chapter has been adapted from the following publication:

Brian L. Kim, Christoper Chong, and Chiara Daraio. Temporal refraction in an acoustic phononic lattice. *In preparation*, 2023

3.1 Preamble

Temporal refraction of waves induced by a rapid change of the properties of a medium has been considered the dual to the refraction of waves across a spatial boundary. In this chapter, we present the first experimental demonstration of refraction of acoustic waves in a phononic lattice with a temporal boundary in the elastic properties. The conversion of frequency and preservation of wavelength resulting from the discontinuous change in group velocity of incident waves provide evidence of temporal refraction, a fundamental phenomenon of the prorogation of waves in time-varying media. Phononic analogs of the classical Snell and Frensel relationships are also obtained, and are in good agreement with the theoretical predictions.

3.2 Introduction

The propagation of waves in time-varying media has received a great deal of attention across a variety of domains, from optical and electromagnetic to acoustic and elastic systems. Much work has focused on periodic variations in material properties, enabling phenomena including parametric amplification [20, 40, 41], nonreciprocal propagation [32, 39, 42, 43], or topological effects [11, 17, 44]. However, recent focus has shifted to the interaction of propagating waves with non-periodic temporal variations, especially boundaries or discontinuities of the properties of a medium in time [19, 47, 50]. Since such temporal boundaries were introduced [31], they have been studied as a temporal analog to spatial refraction [1, 15, 26–28, 35, 38, 49] and extended to more general space-time variations [6, 8, 9, 46].

Rapid time-variation enables a range of functionalities for electromagnetic waves, such as antireflection temporal coatings [34], enhanced thin absorbers [21], or instantaneous time mirrors [5, 14]. Natural extensions of temporal boundaries have been explored as well, including temporal slabs and layered media [10, 23, 36, 37]

and boundaries with finite rise times [48]. Simple temporal boundaries still have great value and potential utility, enabling broadband, linear frequency conversion [19, 50] without the typical considerations of conventional nonlinear frequency conversion, such as phase matching [7, 18, 22, 24].

A number of schemes have been proposed to realize rapid change in the properties of a host medium, primarily in electromagnetic systems, such as abrupt changes in the Fermi level of graphene sheets [29] or magnetoelastic media [3]. Experimentally, Flash ionization [33, 45], rapidly time-varying optical metasurfaces [19], ultrafast pumping of a metal-semiconductor waveguide [30], and electrostriction-controlled water waves [2] have been shown to achieve frequency conversion using temporal boundaries.

In this chapter, we present the first experimental realization of the refraction of acoustic waves in a one-dimensional phononic lattice, inducing a single temporal boundary in elastic properties. The lattice consists of a series of repelling magnets (serving as discrete masses and springs) controlled by electromagnetic coils (serving as grounding stiffness elements), Fig. 3.1(a). The temporal boundary is realized by a rapid, step-like change in the grounding stiffness, Fig. 3.1(b). The experimentally measured conversion of frequency, conservation of wavelength, and transmission and reflection of signals provides a novel demonstration of temporal refraction in acoustic and elastic systems. Like previous examples of wave propagation in media with dynamic or rapid changes in elastic properties, such as elastic waveguides with piezoelectric elements [13, 25, 41] or magnetically tunable resonators [12], this work demonstrates both fundamental physics of waves in time-varying media, as well as the potential for time-varying acoustic and elastic devices for signal processing, filtering, or frequency conversion.

3.3 Lattice Model

The lattice depicted in Fig. 3.1(a) is modeled as a discrete mass-spring chain, similar to prior work [16, 43]. The equation of motion for the n^{th} mass (ring magnet) with displacement u_n (m) may be written as

$$\begin{aligned} m\frac{d^2u_n(t)}{dt^2} + c\frac{du_n(t)}{dt} + k_{g,n}(t)u_n(t) - F_{drive,n}(t) \\ +k_{linear}\left(u_{n-1}(t) + u_{n+1}(t) - 2u_n(t)\right) &= 0, \end{aligned} \tag{3.1}$$

for $n = 1$ to 12, with fixed boundary conditions $u_1(t) = u_{12}(t) = 0$. The time dependent grounding stiffness, $k_{g,n}(t)$, acts uniformly on masses $n = 3$ to 10. All

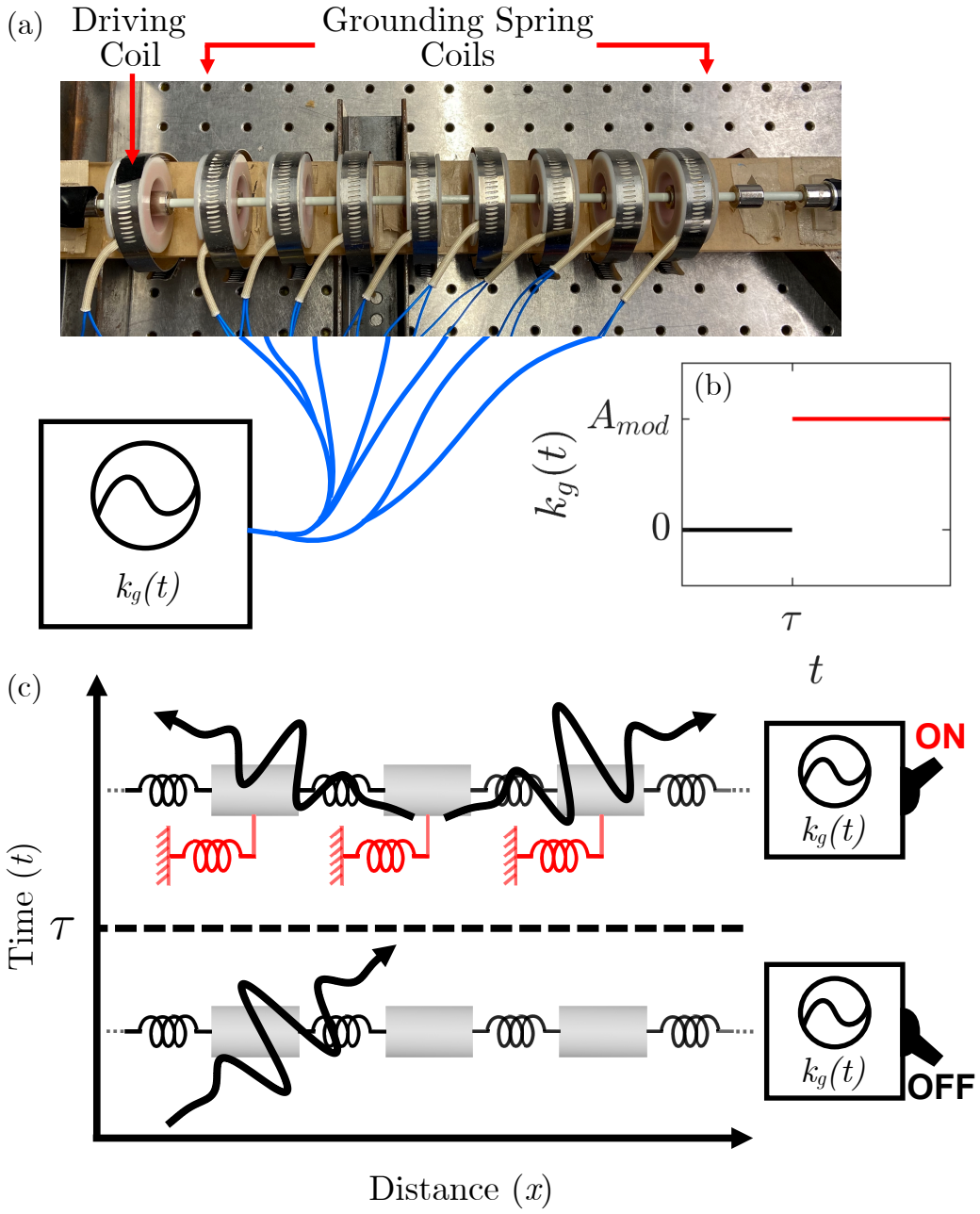

Figure 3.1: Schematic of temporal boundary experiments. **(a)** Photo of experimental lattice, driving and grounding stiffness coils labeled. **(b)** Depiction of step-up grounding stiffness, from zero to A_{mod} at temporal boundary τ. **(c)** Schematic of lattice before (below) step-up temporal boundary ($t < \tau$) and depiction of the incident wave. After (above) the temporal boundary ($t > \tau$), transmitted and reflected waves are observed.

ring magnets have mass $m = 9.8$ g, $c = 0.15$ N s m^{-1} is an empirically determined damping coefficient, and $k_{linear} = 87.03$ N m^{-1} is a linear fit of the measured coupling stiffness between adjacent masses [16].

For the case of a temporal boundary, the grounding stiffness takes the form

$$k_{g,n}(t) = \begin{cases} \delta_{j,n} A_0, & t < \tau \\ \delta_{j,n} A_1, & t \geq \tau \end{cases} \tag{3.2}$$

so that the masses experience a discontinuous change in grounding stiffness at time τ. We consider both a "step-up," where $A_0 = 0$ and $A_1 = A_{mod}$ (depicted in Fig. 3.1(b)), and a "step-down," where $A_0 = A_{mod}$ and $A_1 = 0$ ($[A_{mod}] = \text{N m}^{-1}$). The Kronecker delta with index $j = 3$ to 10 applies $k_{g,n}(t)$ only to masses with grounding stiffness coils.

The driving force is given by $F_{drive,n} = A_{dr}\delta_{2,n}g(t)$, where $A_{dr}([A_{dr}] = \text{N})$ is the driving amplitude, and Kronecker delta $\delta_{2,n}$ applies the input forcing applies only to mass $n = 2$. To study frequency conversion and refraction, $g(t)$ is chosen to be a Gaussian modulated sinusoidal pulse of the form

$$g(t) = \exp\left[(t - t_0)^2/(2\sigma^2)\right] \cos\left(2\pi f_{dr} t\right), \tag{3.3}$$

where f_{dr} is the center frequency of the pulse, t_0 is the time delay of the pulse, and the standard deviation of the Gaussian envelope is defined using a -6dB fractional bandwidth $B_{-6\text{dB}}$, so that $\sigma = \sqrt{2\log 2}/(\pi B_{-6\text{dB}} f_{dr})$. $B_{-6\text{dB}} = 0.6$, and $t_0 = 1.3/(B_{-6\text{dB}} f_{dr})$ for all measurements and simulations.

3.4 Temporal Analog of Snell's Law and Frensel Relations

The general solution of Eq. (3.1) on an infinite lattice without losses ($c = 0$) or drive ($F_{drive} = 0$) is given by

$$u_n(t) = \begin{cases} \int_{-\pi}^{\pi} \left(\hat{A}(k)e^{i\omega_0(k)t} + \hat{B}(k)e^{-i\omega_0(k)t}\right) e^{ikn}, & t < \tau \\ \int_{-\pi}^{\pi} \left(\hat{C}(k)e^{i\omega_1(k)t} + \hat{D}(k)e^{-i\omega_1(k)t}\right) e^{ikn}, & t \geq \tau \end{cases} \tag{3.4}$$

where the dispersion relation before the temporal boundary $t < \tau$ is $\omega_0(k)^2 = A_0/m + 4k_{linear}\sin^2(k/2)/m$ and the dispersion relation after the temporal boundary $t > \tau$ is $\omega_1(k)^2 = A_1/m + 4k_{linear}\sin^2(k/2)/m$ (see Fig. 3.2(a) for step-up case). The Fourier coefficients $\hat{A}(k)$ and $\hat{B}(k)$ are chosen to satisfy the initial data and $\hat{C}(k)$ and $\hat{D}(k)$ are chosen to ensure continuity of u_n and $\dot{u}_n$ at the interface $t = \tau$.

For initial data that is spectrally concentrated at a wavenumber k_0 (like a Gaussian-modulated pulse in (3.3)) the resulting incident wave can be approximated by

$$u_n(t) = U_i e^{i(k_0 n + \omega_0(k_0))t}, \qquad t < \tau \tag{3.5}$$

where $U_i = \hat{A}(k_0)$ is the amplitude of the incident wave. Note, the $\hat{B}$ coefficient is zero since the incident wave is assumed to be propagating in one direction. For $t > \tau$, the solution given by Eq. (3.4) can be approximated by

$$u_n(t) = U_t e^{i(k_0 n + \omega_1(k_0))t} + U_r e^{i(k_0 n - \omega_1(k_0))t}, \tag{3.6}$$

where the spectral concentration about the wavenumber k_0 was again assumed. The coefficient $U_t = \hat{C}(k_0)$ is the amplitude of the transmitted wave and the inclusion of the amplitude $U_r = \hat{D}(k_0)$ accounts for a reflected wave.

Differentiating the two dispersion relationships $\omega_0(k)^2$ and $\omega_1(k)^2$ with respect to k leads to

$$\omega_0(k)\omega_0'(k) = k_{linear}/m \sin(k/2)\cos(k/2), \tag{3.7}$$

$$\omega_1(k)\omega_1'(k) = k_{linear}/m \sin(k/2)\cos(k/2), \tag{3.8}$$

which implies that

$$\delta := \frac{\omega_0(k)}{\omega_1(k)} = \frac{c_1(k)}{c_0(k)}, \tag{3.9}$$

where the group velocities are $c_0(k) = \omega_0'(k)$ and $c_1(k) = \omega_1'(k)$, respectively (see Fig. 3.2(b)). Equation (3.9) is a phononic analog of Snell's law for time

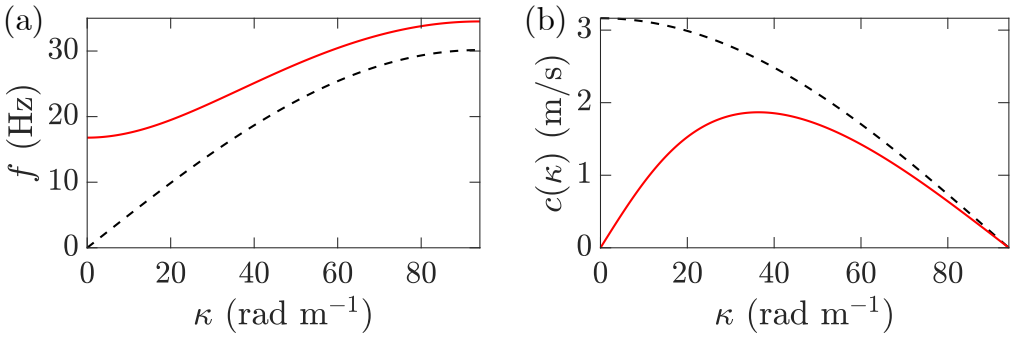

Figure 3.2: Dispersion and group velocity across temporal boundary. **(a)** Dispersion relation of the infinite lattice before (black dashed) and after (red solid) step-up grounding stiffness temporal boundary ($\kappa = k/a$, $f = \omega/(2\pi)$ are the dimensional wavenumber (rad m^{-1}) and frequency (Hz), respectively). **(b)** Group velocity versus wavenumber of infinite lattice before (black dashed) and after (red solid) step-up boundary.

refraction. The corresponding Frensel relations are found by enforcing continuity at the interface $t = \tau$ in Eqs. (3.5) and (3.6), yielding

$$\frac{\tilde{U}_t}{\tilde{U}_i} = \frac{1+\delta}{2}, \tag{3.10a}$$

$$\frac{\tilde{U}_r}{\tilde{U}_i} = \frac{1-\delta}{2}, \tag{3.10b}$$

where $\tilde{U}_i = U_i e^{i\omega_0(k_0)\tau}, \tilde{U}_t = U_t e^{i\omega_1(k_0)\tau}, \tilde{U}_r = U_r e^{i\omega_1(k_0)\tau}$. Equation (3.10b) implies there will always be a reflected wave unless $\delta = 1$, which corresponds to the case of no temporal change in grounding stiffness ($A_{mod} = 0$).

3.5 Experimental Observation of Temporal Refraction and Snell's Law

The experimental platform is adapted from [16, 43]. For details, refer to Section 2.1.

We first demonstrate that the proposed lattice with temporal boundary can efficiently convert input frequency. We consider Gaussian-modulated sinusoidal pulses, as defined in Eq. (3.3), incident on a temporal boundary. For the step-up, center frequencies of $f_{dr} = 10$ to 30 Hz in 2 Hz increments are used so that the incident wavepacket is not longer than the lattice. For the step-down incident frequencies, we use wavepackets of the same wavelengths as the step-up, which are simply the post-boundary frequencies $f_1 = \omega_1(k_0)/(2\pi)$ of the step-up case. At the temporal boundary $\tau = 0.17255$ s, a DC voltage applied to the modulating coils is turned on (off) for a step-up (step-down) boundary, resulting in an rapid change in grounding stiffness of the modulated portion of the lattice from $k_g(t < \tau) = A_0$ N m^{-1} to $k_g(t \geq \tau) = A_1$ N m^{-1} with a change in amplitude of magnitude $A_{mod} \approx 106$ N m^{-1}. The velocity time series of every mass ($n = 2$ to $n = 11$) is measured using the laser Doppler vibrometer. The LDV measurements are synchronized via a trigger signal from a function generator providing the DC modulation signal, which also triggers a second function generator providing the input wavepacket and initiates data acquisition by an oscilloscope. Both modulation and input signal voltages are amplified before transmission to modulation and input coils, respectively. Fig. 3.3(a) shows a representative measurement of a velocity time-series of the input ($n = 2$) and output ($n = 11$) masses for a step-up boundary.

The input frequency f_0 and the output frequency f_1 are defined as the location of the spectral peaks (Fourier transform) of the input and output velocity time series, respectively. The input velocity time series is measured at $n = 2$ for time $t = 0$ to $t = \tau$ to isolate the incident wavepacket, and the output velocity time series is

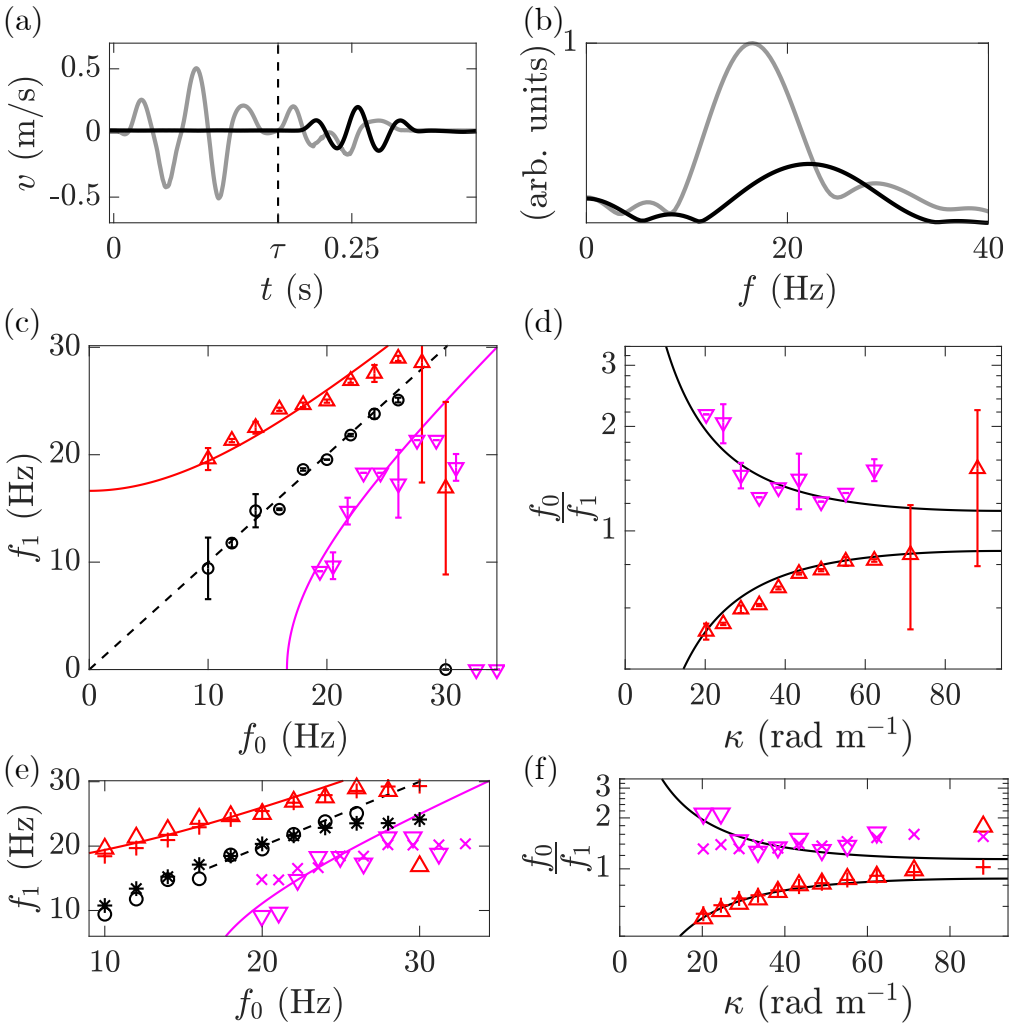

Figure 3.3: Frequency conversion across temporal boundary. **(a)** Representative measured velocity time series of input mass ($n = 2$, gray) and output mass ($n = 11$, black) for Gaussian pulse with center frequency $f_0 = f_{dr} = 18$ Hz. Black dashed line denotes step-up temporal boundary. **(b)** Fourier transforms of incident (gray) and transmitted signals (black) from (a), showing frequency conversion. **(c)** Markers with error bars show output frequency versus input frequency of Gaussian pulse signals in lattice with temporal boundary (step-up, red triangles; step-down, magenta down-triangles) and without temporal boundary (black circles). Theoretical curves based on dispersion relationships with (step-up, red; step-down, magenta) and without (dashed black) temporal boundary. **(d)** Measured ratio of input to output frequency, step-up (red triangles) and step-down (magenta down-triangles), with theoretical phononic analog of Snell's law (black). **(e),(f)** Comparison of experimental measurement (same data as (c) and (d)) to simulation of frequency conversion and ratio (step-up, crosses; step-down, X's, stars, no boundary.

measured at $n = 11$ from $t = \tau = 0.17255$ s to $t = t_{max} \in [0.3, 0.36]$ s to isolate the transmitted wavepacket. Typical spectral peaks used to determine f_0 and f_1 are shown in Fig. 3.3(b), which correspond to the velocity time series shown in Fig. 3.3(a). Similarly, the reflected wavepacket may be observed by measuring the velocity time series at $n = 2$ from $t = \tau$ to $t = t_{max}$.

Fig. 3.3 (c) shows the measured output frequency f_1 versus input frequency f_0 with (step-up, red; step-down, magenta) and without (black) temporal boundaries. Markers (step-up, triangles; step-down, down-triangles; no boundary, circles) show the averages of six sets of measurements, with standard error bars for both input and output frequencies. The solid red and magenta curves are the expected output frequency f_1 for the step-up and step-down, respectively, and the dashed black is the case of no boundary. The expected output frequency is calculated by rearranging Eq. (3.9) and substituting $\omega_{0,1} = 2\pi f_{0,1}$, so that $f_1 = f_0 c_0/c_1$. Theoretical propagation speeds c_0 and c_1 are a function of the coupling stiffness k_{linear} and the magnitude of the grounding stiffness $k_{g,n}(t)$. In the absence of the temporal boundary, $f_1 = f_0$, and no frequency conversion is observed. The measured output frequencies after a temporal boundary show excellent agreement with the theoretical predictions, especially the step-up, except at higher frequencies approaching the cutoff frequency of the lattice. The step-down suffers from stronger dispersion of incident signals, but still exhibits frequency clear conversion of frequency versus the lattice without any temporal boundary. Additionally, we plot the measured ratio $\delta = f_0/f_1$ of signals refracted across the temporal boundary as a function of theoretical incident wavenumber (see Fig. 3.3(d)), demonstrating that frequency conversion agrees with the analytical prediction based on the phononic analog of Snell's law (Eq. (3.9)). Experimental frequency conversion and ratio are compared with the same results for a numerically simulated lattice in Fig. 3.3 (e) and (f), solving Eq. (3.1) using a variable step 4^{th} order Runge-Kutta method (MATLAB ode45), in order to validate our finite, linear theoretical model.

Second, we demonstrate the conservation of wavelength across the temporal boundary. By taking a two-dimensional Fourier transform of the velocity field of the lattice before and after the temporal boundary, we determine the frequency and wavenumber of propagating wavepackets as the location of the maximum amplitude in the inverse space. This is shown for two example input frequencies, $f_0 = 18$ and 26 Hz in Fig. 3.4(a) and (b), respectively, for the step-up, and $f_0 = 24.5$ and 30.9 Hz in Fig. 3.4(c) and (d), respectively, for the step-down. Before the boundary, we

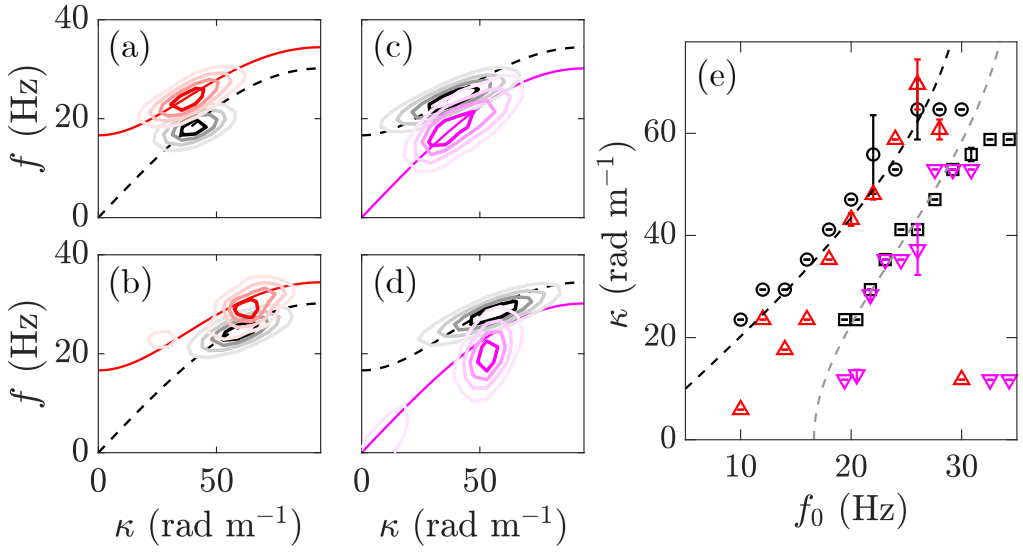

Figure 3.4: Wavenumber conservation across temporal boundary. **(a)-(d)** Two-dimensional Fourier transform of incident (black contours) and transmitted wavepackets for the step-up (red contours in (a,b)) and the step-down (magenta contours in (b,d)) system for input frequencies $f_0 = 18$ Hz (a), $f_0 = 26$ Hz (b), $f_0 = 24.5$ Hz (c), $f_0 = 30.9$ Hz (d). Initial (dashed black) and post-boundary (solid step-up red, step-down magenta) theoretical dispersion relations are also shown. **(e)** Measured step-up and step-down wavenumber versus input frequency of incident (black circles, squares) and transmitted (red triangles, magenta down-triangles) wavepackets with standard error. Theoretical expected wavenumber for step-up (dashed black) and step-down (dashed gray) are also shown.

observe a peak (black contours) centered near the input frequency f_0 and located on the initial dispersion relation $\omega_0(k)$ (dashed black) as expected. After the boundary, the red (magenta) peaks are shifted up (down) in the frequency axis for the step-up (step-down), but remain at approximately the same wavenumber, now aligned with the post-boundary dispersion relation $\omega_1(k)$ in solid red (magenta). This is in contrast to spatial refraction, where the peak would translate left (right) in the wavenumber axis onto the post-boundary dispersion relation [27]. In Fig. 3.4(e), the incident and transmitted wavenumbers are plotted versus the input frequency f_0 for the full range of input frequencies for both the step-up (black quares and red triangles) and step-down (black circles and magenta down-triangles) boundaries. The expected wavenumber for temporal refraction, which is the initial dispersion relation $\omega_0(k_0)$, is plotted for the step-up (dashed black) and step-down (dashed gray). The discrepancies at longer wavelengths most likely occur since the low frequency input signals do not terminate before the temporal boundary; likewise,

shorter wavelengths near the cutoff frequency experience strong dispersion. Overall, however, in clear contrast to the conversion of wavelength that would be present across a spatial boundary, the experiments demonstrate the preservation of the expected wavelength across the temporal boundary, complementing the Snell's law to complete the temporal analog to spatial refraction.

3.6 Experimental Observation of Fresnel Relations

Last, we experimentally reconstruct the Fresnel relations given in Eq. (3.10a) and (3.10b). The amplitude of incident (U_i) wavepackets is measured as the maximum velocity of a mass before the temporal boundary. Likewise, the transmitted (U_t), and reflected (U_r) wavepacket amplitudes are given by the maximum velocities immediately after the temporal boundary at masses forward (to the right) and backward (to the left), respectively, of the approximate spatial location of the wavepacket at the time of the termporal boundary. The measured ratios of these amplitudes are plotted, with error bars denoting standard error of six sets of measurements, in Fig. 3.5(a) and (b) for the step-up and step-down, respectively, along with the corresponding magnitudes of the theoretical predictions, based on the ratio δ for the given temporal boundary. Again, outside of smaller wavenumbers, where longer signal periods limit measurement of reflections in the short finite lattice, and larger wavenumbers approaching the cutoff frequency, the measured transmitted and reflected amplitudes agree well with the theoretical predictions, although the step-down suffers from low transmission. Still, both cases show a dependence on the incident wavelength in agreement with the phononic analog to the Fresnel relations.

3.7 Numerical Simulations

Since strong dissipation limits the length of the current experimental lattice, we employ numerical simulation to further study the refraction phenomena. We have shown that the numerical lattice model accurately captures the behavior of the experimental system, as demonstrated in Fig. 3.3(e) and (f) and in previous work by the authors [16]. Using simulation, it is possible reduce or eliminate dissipative forces in order to increase the lattice length and clearly observe the refraction of incident wavepackets in a lattice longer than the wavepacket itself. Accordingly, in Eq. 3.1, we set $c = 0$ Ns/m and $N = 64$ and select an input pulse (see Eq. 3.3) with center frequency $f_{dr} = f_0 = 10$ Hz at the driving mass $n = 2$.

The time-displacement field of the lattice in Fig. 3.6(a) shows the propagation of the incident pulse (I) and its refraction across a step-up temporal boundary

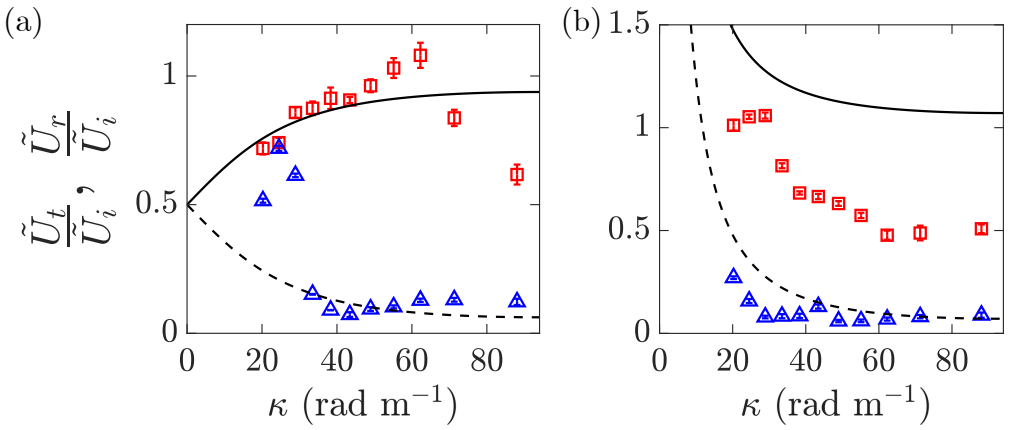

Figure 3.5: Temporal Fresnel relations. **(a),(b)** Experimental measurement of Fresnel relations for step-up (a) and step-down (b) boundaries. Amplitude ratios of transmitted to incident wavepackets (red squares) and reflected to incident wavepackets (blue triangles). Theoretical Fresnel relations based on value of δ for temporal boundary for transmitted (solid) and reflected (dashed) waves.

at $\tau = 2.6 \cdot t_0 \approx 0.563$ s with amplitude $A_{mod} = 106$ N/m. Across the the temporal boundary, a reflected (R) and transmitted pulse (T) are observed. This is further illustrated by the snapshots before, at, and after the temporal boundary in Fig. 3.6(b)-(d). We next demonstrate the preservation of wavenumber by taking the spatial Fourier transform of each isolated wavepacket, $\kappa \approx 21$ rad m^{-1}, see Fig. 3.7(a), while the temporal Fourier transform of the signals shows a conversion of the temporal frequency from $f_0 \approx 10.5$ Hz to $f_1 \approx 19.5$ Hz, see Fig. 3.7(b). This affirms the notion of this phenomenon as temporal refraction, converse to the frequency preservation and wavelength conversion of spatial refraction.

A 2D Fourier analysis of the displacement field in Fig. 3.7(c) shows the traces of the incident, transmitted, and reflected waves, which map onto the dispersion relation of the lattice before (dashed) and after (red) the temporal boundary. The upshift in frequency occurs according to the incident wavenumber, and the reflected wave trace has a negative wavenumber, indicating backward propagation. The change in group velocity, predicted by this "jump" from the original dispersion relation to the new relation is observed by tracking the leading edge of the incident and transmitted pulses, shown in Fig. 3.7(d). We determine this speed of the forward propagation wavefront before ($t < \tau$, black) and after ($t > \tau$, red) the temporal boundary using a linear regression. The group velocities of the incident and transmitted wave are $c_0(\kappa) \approx 3.065$ m/s and $c_1(\kappa) \approx 1.567$ m/s, respectively, in good agreement with

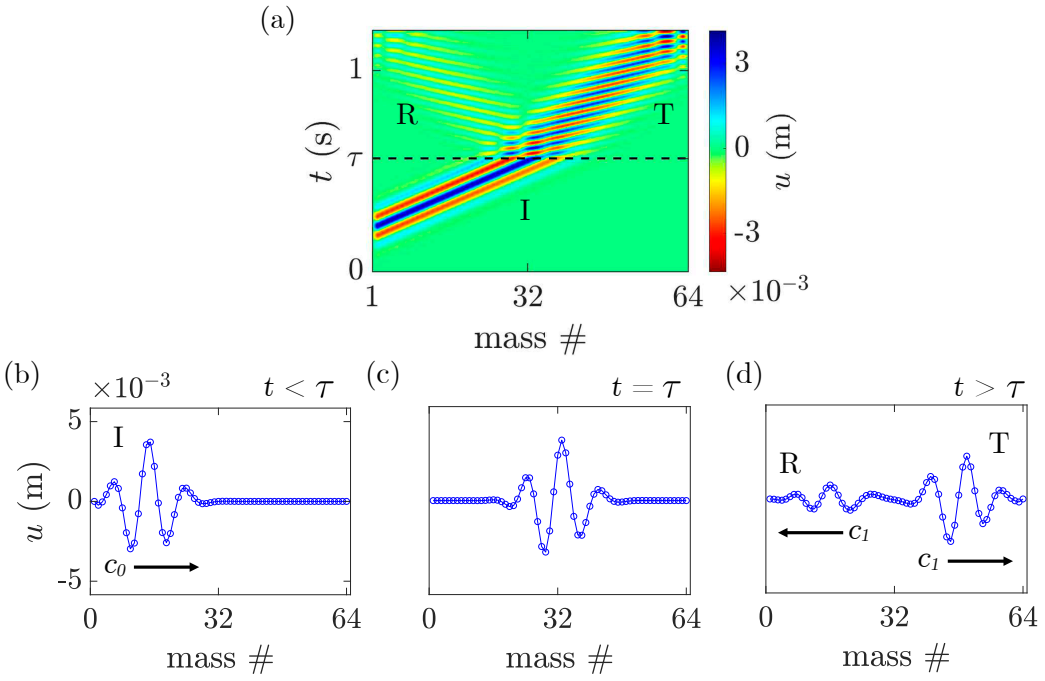

Figure 3.6: Numerical simulation of a $N = 64$ mass lattice with zero dissipation. **(a)** Displacement field of lattice with Gaussian pulse of central frequency $f_0 = 10$ Hz, with temporal boundary at $t = \tau$ denoted by the dashed line, and labels I, T, and R, corresponding, to the incident, transmitted, and reflected pulses waves, respectively. **(b),(c),(d)** Snapshots of mass displacement at times (b) before the temporal boundary $t < \tau$, showing incident pulse (I) traveling approximately at group velocity c_0; (c) at instant of time boundary; and (d) at a time after the temporal boundary $t > \tau$, showing transmitted and reflected pulses (T and R) traveling approximately at group velocity c_1.

the theory (Fig. 3.2(b)) and giving a ratio of $c_1/c_0 \approx 0.51$, close to the predicted $\delta(\kappa) \approx 0.54$.

We also simulate the measurement of the temporal Fresnel relations, comparing them the to experimental measurment shown in Fig. 3.5(a). The transmission and reflection ratios in Fig. 3.7(e) show, like the experiments, that outside of the extremes of wavelengths and frequency, which are, again, limited by the finite lattice, the transmission and reflection of waves across a temporal boundary clearly demonstrates this analog of classical spatial refraction.

Finally, in a lattice of length $N = 256$, we consider a very small wavenumber ($f_{dr} = 4$ Hz), at which the contrast between the propagation speed before and after the step-up boundary is the highest, and the post-boundary propagation speed is small (see Fig. 3.2(b)). This achieves a "slow sound" type trapping of the incident signal,

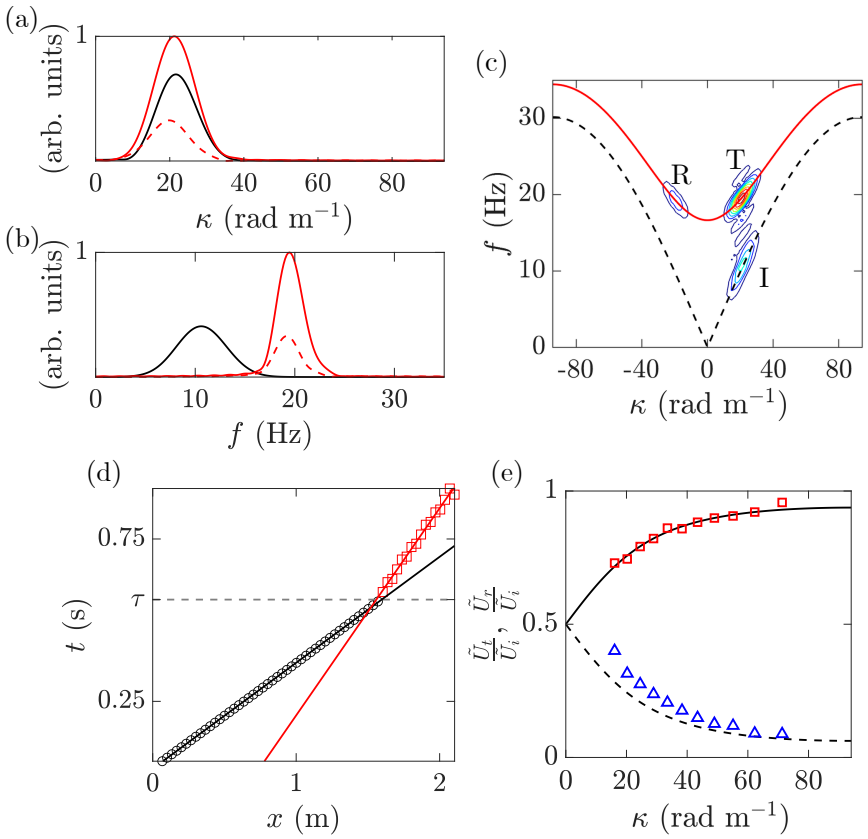

Figure 3.7: Numerical simulation of a $N = 64$ mass lattice with zero dissipation. **(a),(b)** Spatial (a) and temporal (b) Fourier transforms of incident (black), transmitted (red solid), and reflected (red dashed) signals, showing preservation of the signal wavelength and conversion of frequency. **(c)** Contour plot of 2D FFT of time-displacement field with theoretical dispersion relation of lattice before (black dashed) and after (red solid) temporal boundary. Intensity peaks corresponding to the incident, transmitted, and reflected pulses waves are labeled I, T, and R, respectively. **(d)** Location of forward-propagating wavefront of signal versus time, giving approximate group velocity of signal before (black circles and fit line) and after (red squares and fit line) temporal boundary. **(e)** Amplitude ratios of transmitted (red squares) and reflected (blue triangles) wavepackets to amplitude of incident wavepackets. Theoretical Fresnel relations for reflected (dashed) and transmitted (solid) amplitudes are also shown.

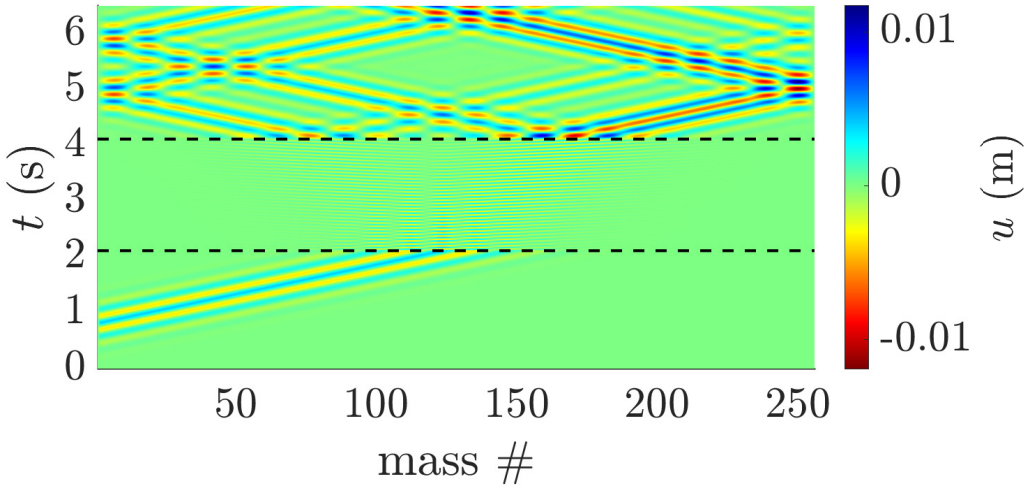

Figure 3.8: "Slow sound" using consecutive step-up and step-down boundaries, denoted by dashed lines. Incident signal of $f_{dr} = 4$ Hz in lattice of length $N = 256$.

similar to the trapping of light in a highly dispersive medium [4]. The grounding stiffness can then be turned off again, a step-down boundary, and the frequencies will be converted back to that of the original signal. The simulated displacement field is shown in Fig. 3.8. In the present system, the strong dispersion of the trapped pulse and multiple reflections may limit practical applications; however, the principle of slowing or trapping sound for an arbitrary time using temporal boundaries has many potential applications such as signal processing or energy absorption.

3.8 Summary and Conclusions

We reported the first experimental demonstration of the refraction of acoustic or elastic waves across a temporal boundary. We present the theory of this temporal refraction in a linearized, infinite-length approximation of the experimental lattice, contextualizing the experimental results in analog to the geometrical optics interpretation. This novel demonstration provides proof of concept for design of acoustic and elastic waveguides and devices with temporal boundaries and rapid changes in elastic properties or group velocity. In particular, the implementation of rapid change in stiffness by the application of an external field is potentially scalable to both larger and smaller systems and conceivably realizable in configurations more complex than one-dimensional propagation.

Acknowledgements

This material is based upon work supported by the US National Science Foundation under Grant Nos. DGE-1745301 (B.L.K.), EFRI-1741565 (C.D.) and DMS-2107945 (C.C.).

References

[1] A. Akbarzadeh, N. Chamanara, and C. Caloz. Inverse prism based on temporal discontinuity and spatial dispersion. *Optics Letters*, 43(14):3297, July 2018. ISSN 0146-9592, 1539-4794. doi: 10.1364/OL.43.003297. URL https://opg.optica.org/abstract.cfm?URI=ol-43-14-3297.

[2] B. Apffel and E. Fort. Frequency conversion cascade by crossing multiple space and time interfaces. *Physical Review Letters*, 128(6):064501, Feb. 2022. ISSN 0031-9007, 1079-7114. doi: 10.1103/PhysRevLett.128.064501. URL https://link.aps.org/doi/10.1103/PhysRevLett.128.064501.

[3] B. Auld, J. Collins, and H. Zapp. Signal processing in a nonperiodically time-varying magnetoelastic medium. *Proceedings of the IEEE*, 56(3):258–272, Mar. 1968. ISSN 1558-2256. doi: 10.1109/PROC.1968.6270.

[4] T. Baba. Slow light in photonic crystals. *Nature Photonics*, 2(8):465–473, Aug. 2008. ISSN 1749-4893. doi: 10.1038/nphoton.2008.146. URL https://www.nature.com/articles/nphoton.2008.146.

[5] V. Bacot, M. Labousse, A. Eddi, M. Fink, and E. Fort. Time reversal and holography with spacetime transformations. *Nature Physics*, 12(10), Oct. 2016. ISSN 1745-2481. URL https://www.nature.com/articles/nphys3810.

[6] F. Biancalana, A. Amann, A. V. Uskov, and E. P. O'Reilly. Dynamics of light propagation in spatiotemporal dielectric structures. *Physical Review E*, 75(4): 046607, Apr. 2007. ISSN 1539-3755, 1550-2376. doi: 10.1103/PhysRevE.75.046607. URL https://link.aps.org/doi/10.1103/PhysRevE.75.046607.

[7] R. W. Boyd. *Nonlinear Optics*. Academic Press, 3rd edition, Mar. 2008. ISBN 978-0-12-369470-6. URL https://www.elsevier.com/books/nonlinear-optics/boyd/978-0-12-369470-6.

[8] C. Caloz and Z.-L. Deck-Léger. Spacetime metamaterials—Part II: Theory and applications. *IEEE Transactions on Antennas and Propagation*, 68(3): 1583–1598, Mar. 2020. ISSN 1558-2221. doi: 10.1109/TAP.2019.2944216.

[9] C. Caloz and Z.-L. Deck-Léger. Spacetime metamaterials—Part I: General concepts. *IEEE Transactions on Antennas and Propagation*, 68(3):1569–1582, Mar. 2020. ISSN 1558-2221. doi: 10.1109/TAP.2019.2944225.

[10] G. Castaldi, V. Pacheco-Peña, M. Moccia, N. Engheta, and V. Galdi. Exploiting space-time duality in the synthesis of impedance transformers via temporal metamaterials. *Nanophotonics*, Aug. 2021. ISSN 2192-8614. URL http://www.degruyter.com/document/doi/10.1515/nanoph-2021-0231/html.

[11] J. Cayssol, B. Dóra, F. Simon, and R. Moessner. Floquet topological insulators. *physica status solidi (RRL) – Rapid Research Letters*, 7(1-2), 2013. ISSN 1862-6270. URL https://onlinelibrary.wiley.com/doi/abs/10.1002/pssr.201206451.

[12] Y. Chen, X. Li, H. Nassar, A. N. Norris, C. Daraio, and G. Huang. Nonreciprocal wave propagation in a continuum-based metamaterial with space-time modulated resonators. *Physical Review Applied*, 11(6):064052, June 2019. ISSN 2331-7019. doi: 10.1103/PhysRevApplied.11.064052. URL https://link.aps.org/doi/10.1103/PhysRevApplied.11.064052.

[13] C. Croënne, J. O. Vasseur, O. Bou Matar, M.-F. Ponge, P. A. Deymier, A.-C. Hladky-Hennion, and B. Dubus. Brillouin scattering-like effect and non-reciprocal propagation of elastic waves due to spatio-temporal modulation of electrical boundary conditions in piezoelectric media. *Applied Physics Letters*, 110(6):061901, Feb. 2017. ISSN 0003-6951, 1077-3118. doi: 10.1063/1.4975680. URL http://aip.scitation.org/doi/10.1063/1.4975680.

[14] M. Fink and E. Fort. From the time-reversal mirror to the instantaneous time mirror. *The European Physical Journal Special Topics*, 226(7):1477–1486, May 2017. ISSN 1951-6401. doi: 10.1140/epjst/e2016-60258-8. URL https://doi.org/10.1140/epjst/e2016-60258-8.

[15] J. Gratus, R. Seviour, P. Kinsler, and D. A. Jaroszynski. Temporal boundaries in electromagnetic materials. *New Journal of Physics*, 23(8):083032, Aug. 2021. ISSN 1367-2630. doi: 10.1088/1367-2630/ac1896. URL https://iopscience.iop.org/article/10.1088/1367-2630/ac1896.

[16] B. L. Kim, C. Chong, S. Hajarolasvadi, Y. Wang, and C. Daraio. Dynamics of time-modulated, nonlinear phononic lattices. *Physical Review E*, 107(3):034211, Mar. 2023. doi: 10.1103/PhysRevE.107.034211. URL https://link.aps.org/doi/10.1103/PhysRevE.107.034211.

[17] T. Kitagawa, E. Berg, M. Rudner, and E. Demler. Topological characterization of periodically driven quantum systems. *Physical Review B*, 82(23):235114, Dec. 2010. ISSN 1098-0121, 1550-235X. doi: 10.1103/PhysRevB.82.235114. URL https://link.aps.org/doi/10.1103/PhysRevB.82.235114.

[18] M. Lapine, I. V. Shadrivov, and Y. S. Kivshar. Colloquium: Nonlinear metamaterials. *Reviews of Modern Physics*, 86(3):1093–1123, Sept. 2014. ISSN 0034-6861, 1539-0756. doi: 10.1103/RevModPhys.86.1093. URL https://link.aps.org/doi/10.1103/RevModPhys.86.1093.

[19] K. Lee, J. Son, J. Park, B. Kang, W. Jeon, F. Rotermund, and B. Min. Linear frequency conversion via sudden merging of meta-atoms in time-variant metasurfaces. *Nature Photonics*, 12(12), Dec. 2018. ISSN 1749-4893. URL http://www.nature.com/articles/s41566-018-0259-4.

[20] S. Lee, J. Park, H. Cho, Y. Wang, B. Kim, C. Daraio, and B. Min. Parametric oscillation of electromagnetic waves in momentum band gaps of a spatiotemporal crystal. *Photonics Research*, 9(2):142, Feb. 2021. ISSN 2327-9125. doi: 10.1364/PRJ.406215. URL https://www.osapublishing.org/abstract.cfm?URI=prj-9-2-142.

[21] H. Li, A. Alù, and A. Alù. Temporal switching to extend the bandwidth of thin absorbers. *Optica*, 8(1):24–29, Jan. 2021. ISSN 2334-2536. doi: 10.1364/OPTICA.408399. URL https://www.osapublishing.org/optica/abstract.cfm?uri=optica-8-1-24.

[22] R. Lifshitz, A. Arie, and A. Bahabad. Photonic quasicrystals for nonlinear optical frequency conversion. *Physical Review Letters*, 95(13):133901, Sept. 2005. ISSN 0031-9007, 1079-7114. doi: 10.1103/PhysRevLett.95.133901. URL https://link.aps.org/doi/10.1103/PhysRevLett.95.133901.

[23] L. Lu, X. Ma, T. Dong, and Q. Liu. Time reflection and refraction in temporal periodic structures. In *2018 IEEE International Symposium on Antennas and Propagation USNC/URSI National Radio Science Meeting*, pages 2253–2254, July 2018. doi: 10.1109/APUSNCURSINRSM.2018.8608800.

[24] L. Ma, O. Slattery, and X. Tang. Single photon frequency up-conversion and its applications. *Physics Reports*, 521(2):69–94, Dec. 2012. ISSN 0370-1573. doi: 10.1016/j.physrep.2012.07.006. URL https://www.sciencedirect.com/science/article/pii/S0370157312002384.

[25] J. Marconi, E. Riva, M. Di Ronco, G. Cazzulani, F. Braghin, and M. Ruzzene. Experimental observation of nonreciprocal band gaps in a space-time-modulated beam using a shunted piezoelectric array. *Physical Review Applied*, 13(3):031001, Mar. 2020. doi: 10.1103/PhysRevApplied.13.031001. URL https://link.aps.org/doi/10.1103/PhysRevApplied.13.031001.

[26] J. T. Mendonça and A. Guerreiro. Time refraction and the quantum properties of vacuum. *Physical Review A*, 72(6):063805, Dec. 2005. ISSN 1050-2947, 1094-1622. doi: 10.1103/PhysRevA.72.063805. URL https://link.aps.org/doi/10.1103/PhysRevA.72.063805.

[27] J. T. Mendonça and P. K. Shukla. Time refraction and time reflection: Two basic concepts. *Physica Scripta*, 65(2):160–163, Jan. 2002. ISSN 0031-8949, 1402-4896. doi: 10.1238/Physica.Regular.065a00160. URL https://iopscience.iop.org/article/10.1238/Physica.Regular.065a00160.

[28] J. T. Mendonça, A. Guerreiro, and A. M. Martins. Quantum theory of time refraction. *Physical Review A*, 62(3):033805, Aug. 2000. doi: 10.1103/PhysRevA.62.033805. URL https://link.aps.org/doi/10.1103/PhysRevA.62.033805.

[29] G. A. Menendez and B. Maes. Time reflection and refraction of graphene plasmons at a temporal discontinuity. *Optics Letters*, 42(23):5006, Dec. 2017. ISSN 0146-9592, 1539-4794. doi: 10.1364/OL.42.005006. URL https://www.osapublishing.org/abstract.cfm?URI=ol-42-23-5006.

[30] F. Miyamaru, C. Mizuo, T. Nakanishi, Y. Nakata, K. Hasebe, S. Nagase, Y. Matsubara, Y. Goto, J. Pérez-Urquizo, J. Madéo, and K. M. Dani. Ultrafast frequency-shift dynamics at temporal boundary induced by structural-dispersion switching of waveguides. *Physical Review Letters*, 127(5):053902, July 2021. ISSN 0031-9007, 1079-7114. doi: 10.1103/PhysRevLett.127.053902. URL https://link.aps.org/doi/10.1103/PhysRevLett.127.053902.

[31] F. Morgenthaler. Velocity modulation of electromagnetic waves. *IRE Transactions on Microwave Theory and Techniques*, 6(2):167–172, Apr. 1958. ISSN 2331-088X. doi: 10.1109/TMTT.1958.1124533.

[32] H. Nassar, B. Yousefzadeh, R. Fleury, M. Ruzzene, A. Alù, C. Daraio, A. N. Norris, G. Huang, and M. R. Haberman. Nonreciprocity in acoustic and elastic materials. *Nature Reviews Materials*, pages 1–19, July 2020. ISSN 2058-8437. doi: 10.1038/s41578-020-0206-0. URL https://www.nature.com/articles/s41578-020-0206-0.

[33] A. Nishida, N. Yugami, T. Higashiguchi, T. Otsuka, F. Suzuki, M. Nakata, Y. Sentoku, and R. Kodama. Experimental observation of frequency up-conversion by flash ionization. *Applied Physics Letters*, 101(16):161118, Oct. 2012. ISSN 0003-6951, 1077-3118. doi: 10.1063/1.4755843. URL http://aip.scitation.org/doi/10.1063/1.4755843.

[34] V. Pacheco-Peña and N. Engheta. Antireflection temporal coatings. *Optica*, 7(4):323–331, Apr. 2020. ISSN 2334-2536. doi: 10.1364/OPTICA.381175. URL https://www-osapublishing-org.caltech.idm.oclc.org/optica/abstract.cfm?uri=optica-7-4-323.

[35] B. W. Plansinis, W. R. Donaldson, and G. P. Agrawal. What is the temporal analog of reflection and refraction of optical beams? *Physical Review Letters*, 115(18):183901, Oct. 2015. ISSN 0031-9007, 1079-7114. doi: 10.1103/PhysRevLett.115.183901. URL https://link.aps.org/doi/10.1103/PhysRevLett.115.183901.

[36] D. Ramaccia, A. Toscano, and F. Bilotti. Light propagation through metamaterial temporal slabs: Reflection, refraction, and special cases. *Optics Letters*, 45(20):5836, Oct. 2020. ISSN 0146-9592, 1539-4794. doi: 10.1364/OL.

402856. URL https://www.osapublishing.org/abstract.cfm?URI=ol-45-20-5836.

[37] D. Ramaccia, A. Alù, A. Toscano, and F. Bilotti. Temporal multilayer structures for designing higher-order transfer functions using time-varying metamaterials. *Applied Physics Letters*, 118(10):101901, Mar. 2021. ISSN 0003-6951, 1077-3118. doi: 10.1063/5.0042567. URL https://aip.scitation.org/doi/10.1063/5.0042567.

[38] D. M. Solís, R. Kastner, and N. Engheta. Time-varying materials in presence of dispersion: Plane-wave propagation in a lorentzian medium with temporal discontinuity. *arXiv:2103.06142*, Mar. 2021. URL http://arxiv.org/abs/2103.06142.

[39] D. L. Sounas and A. Alù. Non-reciprocal photonics based on time modulation. *Nature Photonics*, 11(12):774–783, Dec. 2017. ISSN 1749-4893. doi: 10.1038/s41566-017-0051-x. URL https://www.nature.com/articles/s41566-017-0051-x.

[40] D. Torrent, W. J. Parnell, and A. N. Norris. Loss compensation in time-dependent elastic metamaterials. *Physical Review B*, 97(1):014105, Jan. 2018. ISSN 2469-9950, 2469-9969. doi: 10.1103/PhysRevB.97.014105. URL https://link.aps.org/doi/10.1103/PhysRevB.97.014105.

[41] G. Trainiti, Y. Xia, J. Marconi, G. Cazzulani, A. Erturk, and M. Ruzzene. Time-periodic stiffness modulation in elastic metamaterials for selective wave filtering: Theory and experiment. *Physical Review Letters*, 122(12):124301, Mar. 2019. ISSN 0031-9007, 1079-7114. doi: 10.1103/PhysRevLett.122.124301. URL https://link.aps.org/doi/10.1103/PhysRevLett.122.124301.

[42] S. P. Wallen and M. R. Haberman. Nonreciprocal wave phenomena in spring-mass chains with effective stiffness modulation induced by geometric nonlinearity. *Physical Review E*, 99(1):013001, Jan. 2019. ISSN 2470-0045, 2470-0053. doi: 10.1103/PhysRevE.99.013001. URL https://link.aps.org/doi/10.1103/PhysRevE.99.013001.

[43] Y. Wang, B. Yousefzadeh, H. Chen, H. Nassar, G. Huang, and C. Daraio. Observation of nonreciprocal wave propagation in a dynamic phononic lattice. *Physical Review Letters*, 121(19):194301, Nov. 2018. ISSN 0031-9007, 1079-7114. doi: 10.1103/PhysRevLett.121.194301. URL http://arxiv.org/abs/1803.11503. arXiv: 1803.11503.

[44] Y.-T. Wang, Y.-T. Wang, Y.-W. Tsai, and W. Gao. Floquet topological photonic crystals with temporally modulated media. *Optics Express*, 28(14):21268–21274, July 2020. ISSN 1094-4087. doi: 10.1364/OE.395504. URL https://www.osapublishing.org/oe/abstract.cfm?uri=oe-28-14-21268.

[45] S. C. Wilks, J. M. Dawson, and W. B. Mori. Frequency up-conversion of electromagnetic radiation with use of an overdense plasma. *Physical Review Letters*, 61(3):337–340, July 1988. ISSN 0031-9007. doi: 10.1103/PhysRevLett.61.337. URL https://link.aps.org/doi/10.1103/PhysRevLett.61.337.

[46] Y. Xiao, G. P. Agrawal, and D. N. Maywar. Spectral and temporal changes of optical pulses propagating through time-varying linear media. *Optics Letters*, 36(4):505, Feb. 2011. ISSN 0146-9592, 1539-4794. doi: 10.1364/OL.36.000505. URL https://www.osapublishing.org/abstract.cfm?URI=ol-36-4-505.

[47] Y. Xiao, D. N. Maywar, and G. P. Agrawal. Reflection and transmission of electromagnetic waves at a temporal boundary. *Optics Letters*, 39(3):574, Feb. 2014. ISSN 0146-9592, 1539-4794. doi: 10.1364/OL.39.000574. URL https://www.osapublishing.org/abstract.cfm?URI=ol-39-3-574.

[48] J. Zhang, W. R. Donaldson, and G. P. Agrawal. Impact of the boundary's sharpness on temporal reflection in dispersive media. *Optics Letters*, 46 (16):4053, Aug. 2021. ISSN 0146-9592, 1539-4794. doi: 10.1364/OL.432180. URL https://www.osapublishing.org/abstract.cfm?URI=ol-46-16-4053.

[49] J. Zhang, W. R. Donaldson, and G. P. Agrawal. Temporal reflection and refraction of optical pulses inside a dispersive medium: An analytic approach. *Journal of the Optical Society of America B*, 38(3):997, Mar. 2021. ISSN 0740-3224, 1520-8540. doi: 10.1364/JOSAB.416058. URL https://www.osapublishing.org/abstract.cfm?URI=josab-38-3-997.

[50] Y. Zhou, M. Z. Alam, M. Karimi, J. Upham, O. Reshef, C. Liu, A. E. Willner, and R. W. Boyd. Broadband frequency translation through time refraction in an epsilon-near-zero material. *Nature Communications*, 11(1):2180, Dec. 2020. ISSN 2041-1723. doi: 10.1038/s41467-020-15682-2. URL http://www.nature.com/articles/s41467-020-15682-2.

Chapter 4

WAVENUMBER BAND GAPS AND STABILITY OF NONLINEAR TIME-PERIODIC PHONONIC LATTICES

Research presented in this chapter has been adapted from the following publication:

Brian L. Kim, Christoper Chong, Setare Hajarolasvadi, Yifan Wang, and Chiara Daraio. Dynamics of time-modulated, nonlinear phononic lattices. *Physical Review E*, 107:034211, Mar. 2023. https://doi.org/10.1103/PhysRevE.107.034211

4.1 Preamble

In this chapter, the response of a one-dimensional phononic lattice with time-periodic elastic properties is studied with experimental, numerical, and theoretical approaches in both linear and nonlinear regimes. For small amplitude excitation, in agreement with linear theoretical predictions, wavenumber band gaps emerge. The underlying instabilities associated to the wavenumber band gaps are investigated with Floquet theory and the resulting parametric amplification is observed in both theory and experiments. In contrast to genuinely linear systems, large amplitude responses are stabilized via the nonlinear nature of the magnetic interactions of the system, and results in a family of nonlinear time-periodic states. The bifurcation structure of the periodic states is studied, where it is found the linear theory predicts parameter values from which the time-periodic states bifurcate from the zero state. In the presence of an external drive, the parametric amplification induced by the wavenumber band gap can lead to bounded and stable responses that are temporally quasi-periodic. Controlling the propagation of acoustic and elastic waves by balancing nonlinearity and external modulation offers a new dimension in the realization of advanced signal processing and telecommunication devices. For example, it could enable time-varying, cross-frequency operation, mode- and frequency-conversion, and signal-to-noise ratio enhancements.

4.2 Introduction

Acoustic metamaterials and phononic crystals often achieve control of wave propagation by leveraging scattering effects induced by the presence of spatial periodicity in the design of their micro-structure [23, 29, 33, 36, 61]. In active mechanical

systems, the periodic variation of material properties in time provides an additional, less-explored strategy to control acoustic and elastic waves. This strategy draws inspiration from the study of parametric amplifiers [12, 56] and the effects of traveling-wave-like harmonic modulations (i.e., periodic in both space and time) on electromagnetic waves [6, 7]. Indeed, spatio-temporally periodic acoustic and elastic systems have been shown, both theoretically and experimentally, to exhibit the characteristic opening of band gaps in their dispersion relations. Most studies have focused on the presence of nonreciprocal frequency band gaps in linear systems, such as beams and metamaterials with spatially and temporally varying resonators or continuous elastic structures with spatio-temporally periodic properties [1, 9, 21, 35, 40–43, 59, 65, 69].

Whereas frequency band gaps are the hallmark of spatially periodic systems, gaps in the wavenumber axis of a linear medium's dispersion relation have been shown to arise in time-periodic and spatio-temporally periodic systems, in which the wave speed of the traveling-wave-like-modulation is greater than the velocity of propagation of the medium [6, 19, 28, 31, 49, 60, 65]. These so-called wavenumber band gaps are understood to be parametrically amplified standing waves (i.e., non-propagating, hence the analogous notion of a band gap) [12, 49, 60]. For example, in a phononic lattice with a supersonic traveling-wave modulation, incident signals within the induced wavenumber band gap excite unstable oscillations of the scattered field. This results in apparent amplification of frequencies corresponding to the band gaps, which are different for forward- and backward-propagating waves since this form of spatio-temporal modulation breaks reciprocity [65]. In another example, an elastic waveguide is modulated periodically only in time via an array of piezoelectric patches controlling the stiffness. The reflection of a broadband signal incident on the interface of the modulated region is observed to comprise narrowband content at half the modulation frequency, consistent with the parametrically amplified standing wave solution present within wavenumber band gaps [60]. Generally, in a lossy mechanical medium, the gain realized by time-periodic modulation may compensate for or balance energy dissipation [58]. Wavenumber band gaps have been shown to open experimentally in transmission lines and theoretically in proposed photonic systems [31, 49]. In a system more analogous to the present study, instabilities in a linear phononic lattice with time-modulated spatially periodic modulations have been explored [32], but the opening of wavenumber band gaps in the dispersion relation of phononic systems has not been directly shown.

Aside from periodicity, the introduction of nonlinearity provides an alternative strategy to control waves in discrete chains. The role of nonlinearity in discrete chains, for example, has been studied extensively since the first analysis of the Fermi-Pasta–Ulam–Tsingou problem [16, 18]. Some examples include nonlinearity-induced band gaps [5, 8, 20], nonreciprocal transmission [4], discrete breathers [3, 13, 55], solitary waves [37, 46, 57] frequency conversion [52], and nonlinear dispersion [15, 34, 39, 66]. A more comprehensive review of the extensive work done on nonlinear lattices can be found in the review articles [2, 17, 25] or books [10, 24, 45, 54].

Nonlinear effects and their interplay with parametric amplification have indeed been studied in photonic and transmission line systems, which serve as practically implementable analogs to one-dimensional optical metamaterials. Multistability has been shown in Kerr nonlinear photonic crystals [53, 64, 67] as well as transmission lines with nonlinear capacitance [47]. Parametric amplification in nonlinear transmission lines has also been demonstrated [27, 48]. Unidirectional soliton-like edge states in nonlinear Floquet topological insulators, which are modeled by a discrete Nonlinear Schrödinger equation with time variable coefficients, were explored in [38]. The interactions between extrinsic time-periodic modulation and nonlinear effects in phononic systems, however, have typically only been investigated in the limits of linearized behavior of nonlinear systems [63].

In the present chapter, we investigate a time-modulated phononic lattice in both linear and nonlinear regimes using a combination of experiments, theory and numerical simulations. In addition to the experimental observation of wavenumber band gaps, we demonstrate how the linear dynamics can partially explain the observed bifurcation structure of time-periodic states that result due to the presence of nonlinearity. The linearized theory is complemented by a detailed nonlinear bifurcation analysis that exploits a fixed point algorithm for the computation of time-periodic orbits and a pseudo-arclength continuation. This bifurcation structure provides a road map to understand hysteretic behavior observed in the system in the presence of an external drive, where both time-periodic and temporally quasi-periodic states are found to co-exist.

The chapter is structured as follows. The experimental details are described in Sections 4.3. Results on wavenumber band gaps and their associated instabilities in the small amplitude regime and a parametric investigation of stability are reported in Section 4.4. Nonlinear effects leading to the formation of stable temporally time-

Table 4.1: Lattice Model Parameters

Measured		Fit	
Parameter	Value	Parameter	Value
m	0.0097 kg	c	0.15 N s m^{-1}
a	33.4 mm	k_{linear}	87.03 N m^{-1}
f_{mod}			
$= \omega_{mod}/(2\pi)$	$\in$ [1 70] Hz	k_{dipole}	9.044×10^{-7} N m^4
$f_{dr} = \omega_{dr}/(2\pi)$	$\in$ [1 40] Hz	$P_{0,dipole}$	0.7047 N
		A_{mod}	$\in$ [0 100] N m^{-1}
		A_{dr}	$\in$ [0.15 0.4] N

periodic and quasi-periodic orbits are explored in 4.6. Section 4.7 concludes the chapter.

4.3 Experimental Setup

The experimental platform is adapted from [16, 65]. For details, refer to Section 2.1.

For the present study, an AC sinusoidal voltage (with zero DC offset) applied to the electromagnetic coils induces a harmonic grounding stiffness modulation of the form

$$k_g(t) = \delta_{j,n} A_{mod} \cos(2\pi f_{mod} t) \tag{4.1}$$

with amplitude A_{mod} ($[A_{mod}]$ = N m^{-1}) and frequency f_{mod} ($[f_{mod}]$ = Hz). Table 4.1 summarizes the measured and fit parameters used throughout the chapter.

4.4 Wavenumber Band Gaps

Theoretical Determination of Wavenumber Band Gaps

In the small amplitude displacement regime, we observe experimentally the existence of wavenumber band gaps. In this section, we summarize the linear theory predicting parameter values that lead to the emergence of wavenumber band gaps in our system. In the limit of small displacements, we employ the linear approximation of the magnetic inter-site-coupling discussed previously. Ignoring damping (which we return to later) and assuming that the chain is infinite in length results in the following model

$$m\frac{d^2u_n}{dt^2} + A_{mod}\cos(2\pi f_{mod}t)u_n + k_{linear}(2u_n - u_{n-1} - u_{n+1}) = 0. \tag{4.2}$$

One approximate solution of this equation will be the sum of the incident wave and the scattered fields induced by the time modulation [41],

$$u_n(t) = U_{-1}e^{i(q_0 n - 2\pi f_{-1} t)} + U_0 e^{i(q_0 n - 2\pi f_0 t)} + U_1 e^{i(q_0 n - 2\pi f_1 t)}, \tag{4.3}$$

where f_0 is the ordinary frequency of the incident wave with amplitude U_0 and $q_0 = \kappa_0 a$ is the dimensionless form of the wavenumber. Note, an analysis that includes all harmonics is discussed in Section 4.5. The amplitudes of the scattered fields are U_{-1} and U_1 which have frequencies $f_{\pm 1} = f_0 \pm f_{mod}$. The coupling between the incident and scattered fields is negligible except where $D(f_0, q_0) = D(f_{\pm 1}, q_0) = 0$ [41, 65], where

$$D(f, q) := m(2\pi f)^2 - 4k_{linear} \sin^2(q/2) = 0, \tag{4.4}$$

is the usual dispersion relationship in the unmodulated lattice (i.e., $A_{mod} = 0$). The intersections occur precisely when $f_0(q) = f_{mod}/2$. Substituting Eq. (4.3) into Eq. (4.2) and equating coefficients of the three harmonics leads to a zero determinant condition [41], and is given by the expression

$$\begin{aligned} \hat{D}(f, q) = \quad & D(f - f_{mod}, q)\, D(f, q)\, D(f + f_{mod}, q) \\ & -A_{mod}^2 \left(D(f - f_{mod}, q) - D(f + f_{mod}, q) \right) \\ = \quad & 0. \end{aligned} \tag{4.5}$$

This condition is a modified dispersion relation in the neighborhood of the intersections of $D(f_{\pm 1}, q_0) = 0$ and $D(f_0, q_0) = 0$. Values of q that lead to solutions of Eq. (4.5) with complex valued f makeup the so-called wavenumber band gaps in the band structure and correspond to a parametrically amplified standing wave with growth rate given by the imaginary part of f [31, 60]. The analytical dispersion relations for the unmodulated ($D(f, q) = 0$) and modulated ($\hat{D}(f, q) = 0$) lattices are shown in Fig. 3.2(a) and (b), respectively, for parameters $f_{mod} = 40$ Hz and $A_{mod} = 37.5$ N m^{-1}. As predicted by the intersection of the incident and scattered fields, the wavenumber band gap opens at $f = f_{mod}/2$, as seen in Fig. 3.2(c).

To verify the dispersion calculations, we simulate the lattice as described in Section 2.2 (Eq. (2.1)) using the same modulation parameters for the grounding stiffness $k_g(t)$ and mass m that were used to compute the dispersion relationships, but we use the nonlinear repulsive force (P_{dipole} instead of P_{linear}), and we include viscous damping c (see Table 4.1 for the specific values used). The simulation is solved repeatedly for monochromatic, six-cycle sine bursts from $f_{dr} = 1$ to 40 Hz (in 1 Hz

increments) with driving amplitude $A_{dr} = 0.38$ N. The numerical dispersion relationship is obtained by computing the two-dimensional Fourier transform (2DFFT) of the velocity components of the numerical solutions. Color intensity corresponds to the normalized spectral energy density (a composite of all driving frequencies) of the unmodulated ($A_{mod} = 0$ N m^{-1}) and modulated ($A_{mod} = 37.5$ N m^{-1}) lattices in Fig. 3.2(a) and (b), respectively. This method is similar to a spectral energy density method frequently employed in photonic and phononic systems [41, 62, 65]. The numerical dispersion relation accounts for nonlinearity, gain, losses, and finite effects but still agrees well with the linear theory based on the infinite losses lattice with only three fields used to determine the dispersion relationship.

Experimental Observation of Wavenumber Band Gaps

To reconstruct the dispersion relation of acoustic waves propagating through the experimental lattice, we measure the velocity of each mass using the LDV (Polytec CLV-2534). We use these measurements to construct a full space-time-resolved transient velocity response of the lattice. The leftmost free mass $n = 2$ is driven by a monochromatic, six-cycle sine wave burst from quiescent initial conditions, exciting a right (forward) travelling wave. The finite-cycle burst and termination time of each measurement are chosen so that reflections off the right boundary $n = 12$ are not captured. Using the velocity field measurements from driving frequencies from from $f_{dr} = 1$ to 35 Hz (in 1 Hz increments), a composite of spectral energy densities of the two-dimensional velocity fields yields a reconstruction of the dispersion relation (the same method used in the numerical simulations). Fig. 4.1(a), (b), (d), and (e) show the comparison of measured dispersion against the numerical simulation overlaid with the analytical predictions.

The measured dispersion reconstruction in Fig. 4.1(d) for the lattice without external modulation exhibits the expected behavior of a monatomic lattice, i.e., a single acoustic branch terminating at the edge of the Brillouin zone. The positive wavenumber branch corresponds to forward (right) travelling waves, while the negligible intensity negative wavenumber branch indicates the absence of backward (left) travelling waves in the unmodulated lattice.

The measurements are then repeated with an extrinsic temporal grounding stiffness modulation applied to the lattice via the electromagnetic coils. The effective grounding stiffness of the masses are modulated harmonically at $f_{mod} = 40$ Hz. Dissipation in the experimental apparatus makes detection of small wavenumber

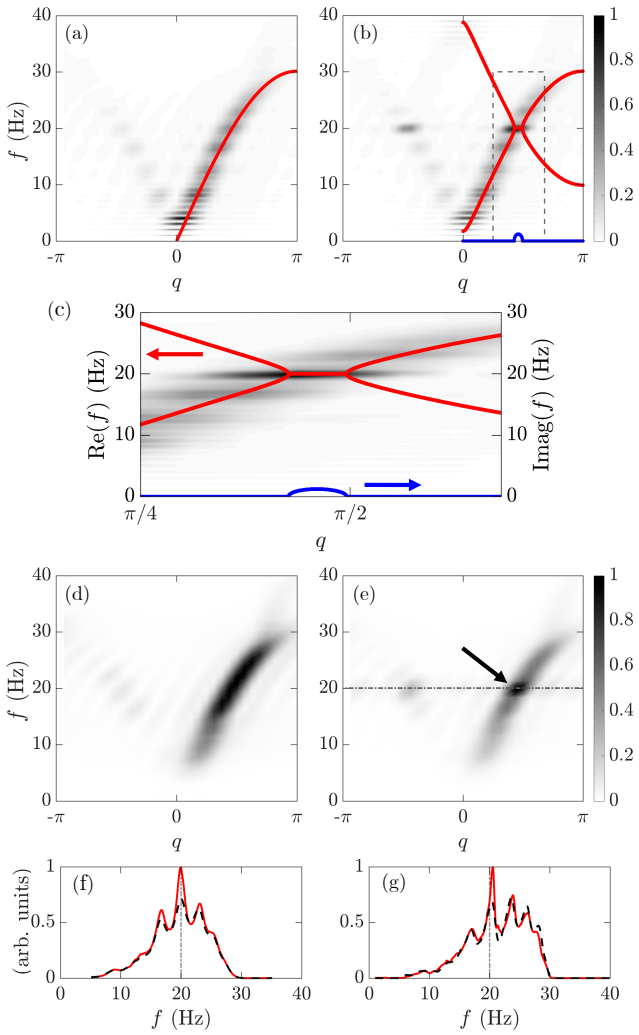

Figure 4.1: Dispersion relation and transmission response in unmodulated and modulated lattice at f_{mod} = 40 Hz. **(a)** Numerical dispersion reconstruction for the unmodulated lattice. The analytical predication is shown by the red curve. **(b)** Numerical dispersion reconstruction with modulation frequency f_{mod} = 40 Hz. The real part (red curve) and imaginary part (blue curve) of the analytical approximation is also shown. **(c)** Expanded view of the band gap from the gray dashed window in panel (b). **(d)** Experimentally measured dispersion reconstruction for the unmodulated lattice. **(e)** Experimentally measured dispersion reconstruction with modulation frequency f_{mod} = 40 Hz. The frequency $f_{mod}/2$ = 20 Hz is indicated by the gray dash-dotted line. The arrow highlights amplitude peak in dispersion branch. **(f)** Numerically simulated frequency transmission spectra for the unmodulated lattice (black dashed curve) and modulated lattice (red curve) with f_{mod} = 40 Hz. The frequency $f_{mod}/2$ = 20 Hz is indicated by the gray dash-dotted line. **(g)** Same as panel (f), but for the experimentally measured frequency transmission spectra.

signals difficult; therefore, the modulation frequency is selected so that the salient features of the wavenumber band gap, which occur at $f_{mod}/2$, lie on a clear section of the dispersion branch. The numerical and experimental dispersion reconstructions shown in Fig. 4.1(b) and (e), respectively, exhibit a strong peak (i.e., darker regions in the spectral energy density), at $f_{mod}/2 = 20$ Hz on the dispersion branch. In the numerical simulation, this peak aligns with the analytical prediction of the wavenumber band gap, and the experimental peak is highlighted by an arrow and seen to align with $f_{mod}/2 = 20$ Hz. This increased amplitude response is consistent with the expected parametric amplification, associated with the complex frequency inside the wavenumber band gap, and is in line with previous results in the literature [31, 60]. Compared to the unmodulated lattice, the dispersion branch of the modulated lattice is largely unchanged, except for the small neighborhood of frequencies around $f_{mod}/2 = 20$ Hz.

Both the experimental and numerical results show good agreement in the presence of time modulation, and the location of the wavenumber band gap is predicted accurately by the analytical model. Moreover, an additional amplitude peak is observed at $f_{mod}/2$ and the negative of the wavenumber corresponding to the band gap, where the negative wavenumber may be interpreted as backward propagating waves (Fig. 4.1(b), (d)). Such behavior is consistent both with the predicted parametrically amplified standing wave solution that occurs within the wavenumber band gap and with previous experimental work that has shown evidence of the same effect via the conversion of broadband signals into narrowband reflections [60].

In addition to exploring dispersion of travelling waves, we examine the transmission spectrum of the harmonically driven lattice. The lattice is driven harmonically at the input mass $n = 2$ by the reference signal of a lock-in amplifier (LIA, Stanford Research SR860). The reference signal is a continuous sine sweep from $f_{dr} = 1$ to 40 Hz, which is sufficiently slow for the lattice to exhibit effectively steady state behavior. The output velocity at mass $n = 11$ is measured using the LDV, and the output is multiplied by the reference signal and integrated over a moving time window by the LIA. This gives a spectrum of the amplitude of the lattice response versus frequency, relative the constant input amplitude of the LIA reference signal. Experimental parameters are identical to the dispersion reconstruction, with $f_{mod} = 40$ Hz, $A_{mod} = 37.5$ N m^{-1}, and $A_{dr} = 0.38$ N. This is also reproduced in numerical simulation. The resulting frequency spectrum demonstrates clearly that the extrinsic time-periodic modulation induces amplification of signals at half

the modulation frequency, in both experiment and simulation, see Fig. 4.1(f) and (g), respectively. The relatively narrowband amplification provides further evidence that the dispersion reconstruction accurately depicts the localized nature of the wavenumber band gap and its amplifying effect on incident signals.

4.5 Parametric Investigation of Stability

A more complete analysis of stability can be achieved by considering more than the three modes included in Eq. (4.3) that result in a complex-valued f. Moreover, the inclusion of damping also has a non-trivial effect on the stability properties. Therefore, we conduct a stability analysis on the linearized equations of motion of an infinite mass-spring chain with damping,

$$m\frac{d^2u_n}{dt^2} + c\frac{du_n}{dt} + A_{mod}\cos\left(2\pi f_{mod}t\right)u_n + k_{linear}\left(2u_n - u_{n-1} - u_{n+1}\right) = 0. \quad (4.6)$$

In particular, we make use of discrete Fourier transform,

$$\hat{u}(q,t) = \sum_{n\in\mathbb{Z}} u_n(t)e^{iqn}, \quad (4.7)$$

to cast Eq. (4.6) in Fourier space,

$$\partial_t^2\hat{u}(q,t) + \frac{c}{m}\partial_t\hat{u}(q,t) + \left[(2\pi f(q))^2 + \frac{A_{mod}}{m}\cos(2\pi f_{mod}t)\right]\hat{u}(q,t) = 0, \quad (4.8)$$

where $D(f(q),q) = 0$, that is $f(q)$ satisfies the dispersion relation in the unmodulated lattice. Equation (4.8) is a Mathieu equation, which includes a linear viscous damping term [22, 26, 30, 50, 68].

The stability regions of the Mathieu equation can be approximated analytically. The standard form of the Mathieu equation is $\ddot{x}(t)+\gamma\dot{x}(t)+(\delta+\epsilon\cos(t))\,x(t) = 0$ where $\gamma = \frac{c}{m2\pi f_{mod}}$, $\delta = \left(\frac{f(q)}{f_{mod}}\right)^2$, and $\epsilon = \frac{A_{mod}}{(2\pi f_{mod})^2 m}$. In the absence of damping, regions of instability in the $[\delta,\epsilon]$ parameter plane emerge at the values $\delta_j = \frac{j^2}{4}$, where j is an integer [44]. If one considers the parametric plot $s(q) = (\delta(f(q)),\epsilon(f(q)))$ in the stability diagram of the Mathieu equation, one sees that $s(q)$ must cross the first instability tounge since $f(q)$ is continuous and increases monotonically from zero, assuming an infinite lattice. Thus, a condition for stability in the limit of small modulation amplitude can be obtained by considering the instability tongue associated to $j = 1$, namely that $\left(\frac{f(q)}{f_{mod}}\right)^2 < 1/4$. This recovers the result that instability is induced by the intersection of dispersion curves when $f(q) = f_{mod}/2$, as discussed in Section 4.4.

In a finite sized lattice with zero boundary conditions, the set of wavenumbers is discrete, and are given by $q_r = \pi r/N$. Thus, to derive a condition for stability in the finite lattice case, each frequency must be inspected, since it is possible that the parametric set of points given by $s(q_r)$ may never fall in the first instability region due to the discrete nature of q_r in the finite lattice.

We now derive the stability condition in a finite lattice in the presence of damping. The transition curves of the the stability regions of the Mathieu equation with damping and small but finite modulation amplitude can be found via perturbation analysis [26, 44],

$$\delta = \frac{1}{4} \pm \frac{\sqrt{\epsilon^2 - \gamma^2}}{2}, \tag{4.9}$$

which is valid for small ϵ. In terms of the original system parameters f_{mod} and A_{mod}, Eq. (4.9) implies the following condition for stability, which considers all $N-1$ wavenumbers of the finite system given by $q_r = \pi r/N$,

$$\max_{1\le r\le N-1} \left| \left(\frac{f(q_r)}{f_{mod}}\right)^2 \pm \frac{1}{2}\sqrt{\left(\frac{A_{mod}}{(2\pi f_{mod})^2 m}\right)^2 - \left(\frac{c}{m2\pi f_{mod}}\right)^2} \right| < \frac{1}{4}. \tag{4.10}$$

The black line of Fig. 4.2(a) shows the transition curves of the regions of instability based on the analytical approximation Eq. (4.10).

While the application of the Mathieu equation in Eq. (4.10) accounts for the finite length and boundary conditions of the experimental lattice, it does not account for the fact that the experimental lattice is only partially modulated. In particular, the first and last free masses are not modulated in order to allow more accurate measurements of their velocities. In this case, one must compute Floquet multiplers to determine stability. If all Floquet multiplers have modulus not exceeding unity, then the solution (the zero solution in this case) is stable. Otherwise it is unstable (at least one Floquet multipler exceeds unity). The stability analysis of the zero state in Section 4.4 is based on a Fourier decomposition in space, which is only valid assuming each node is modulated. If the lattice is partially modulated (like in the experiment, where the first and last node are not modulated) one must determine stability based on the numerical computation the Floquet multipliers.

To numerically compute the Floquet multiplers, we solve the full system of equations given by Eq. (2.1) for the linear case when $F_{mag,n} = k_{linear}\,(2u_n - u_{n-1} - u_{n+1})$. The second order system is be reduced to a first order system $\mathbf{u'(t)} = \mathbf{A}(t)\mathbf{u}(t)$, where the vector $\mathbf{u}(t)$ contains the displacements and velocities of each mass, and the coefficient matrix $\mathbf{A}(t)$ contains the stiffness, damping, and modulation of the lattice,

$$\mathbf{u}(t) = \begin{pmatrix} u_1(t) \\ \vdots \\ u_N(t) \\ u_1'(t) \\ \vdots \\ u_N'(t) \end{pmatrix},$$

$$\mathbf{A}(t) = \begin{pmatrix} \mathbf{0} & \mathbf{I} \\ -\mathbf{M}^{-1}\left(\mathbf{K} + \mathbf{K_g}(t)\right) & -\mathbf{M}^{-1}\mathbf{C} \end{pmatrix},$$

with mass matrix $\mathbf{M} = m\mathbf{I}$, damping matrix $\mathbf{C} = c\mathbf{I}$, stiffness matrix

$$\mathbf{K} = k_{linear} \begin{pmatrix} 2 & -1 & 0 & \cdots & 0 \\ -1 & \ddots & \ddots & \ddots & \vdots \\ 0 & \ddots & & & 0 \\ \vdots & \ddots & & & -1 \\ 0 & \cdots & 0 & -1 & 2 \end{pmatrix},$$

and modulation matrix

$$\mathbf{K}_g(t) = \begin{pmatrix} 0 & 0 & \cdots & & 0 \\ 0 & k_g(t) & \ddots & & \vdots \\ \vdots & \ddots & \ddots & & \\ & & & k_g(t) & 0 \\ 0 & \cdots & & 0 & 0 \end{pmatrix}.$$

Since the harmonic modulation $k_g(t) = A_{mod}\cos(2\pi f_{mod})$ makes the time dependent coefficient matrix periodic with period $T = 1/f_{mod}$, we apply Floquet theory to determine the stability the linearized system. At each point (f_{mod}, A_{mod}) in the modulation parameter space, we solve numerically for the fundamental solution matrix $\mathbf{U}(t)$ at time $t = T$ from initial conditions $\mathbf{U}(t = 0) = \mathbf{I}$. The state is stable if the eigenvalues of $\mathbf{U}(T)$, the Floquet multipliers, have moduli less than one. This corresponds to all multipliers lying within the unit circle in the complex plane. Otherwise, the state is unstable. Similar studies have shown this type of Floquet analysis to be an effective method for characterizing instability of propagating waves in discrete systems [28].

The results of this analysis are shown in Fig. 4.2(a), where the gray shaded region indicates modulation parameters that yield an unstable solution. The qualitative structure of the instability region agrees with the analytical prediction of Eq. (4.10), but the boundary is shifted to higher modulation amplitudes for some frequencies, which is consistent with the fact that fewer masses in the lattice are gaining energy from modulation.

In order to explore the validity of the linear theoretical stability predictions, we study both the numerically simulated and experimentally measured response of the lattice. The existence of unstable, exponentially growing solutions from the linear model implies large-amplitude displacements, and indeed large-amplitude displacements (relative to the equilibrium spacing a) are experimentally observed. To illustrate the difference between the responses, we simulate the response of the lattice both with the linearized and the nonlinear repulsive force (P_{linear} and P_{dipole}, respectively) using the measured and fit parameters matching the experimental setup (see Table 4.1). An unstable set of modulation parameters, as predicted by the linear theory (in particular, $f_{mod} = 41.6\,\mathrm{Hz}$, $A_{mod} = 78\,\mathrm{N\,m^{-1}}$, see black star in Fig. 4.2(a)), is applied to the lattice with no input drive ($A_{dr} = 0$). The simulation is initiated with quiescent conditions except for an initial velocity at the driving mass ($n = 2$). It is observed that while the response of the linear simulation grows exponentially, the nonlinear simulation reaches an oscillatory steady state, sustained by the grounding stiffness modulation. This is illustrated by the velocity responses of the output mass ($n = 11$) in Fig. 4.2(b), with the linear simulation in gray and nonlinear simulation in black. Conversely, for parameter values where the linear theory predicts stability, the responses of both the linear and nonlinear simulations decay with time due to damping. Thus, as a proxy for the theoretical linear instability, we search the full modulation parameter space for any response that does not decay with time, what we will refer to as non-decaying responses, from the nonlinear simulation or experimental lattice.

The modulation parameters that lead to a non-decaying response for the numerical simulation are denoted in Fig. 4.2(a) by white markers. The region of modulation parameters that lead to a non-decaying response in the numerical simulation with nonlinear interaction included exhibits good quantitative agreement with the unstable region predicted through both the Floquet theory and damped Mathieu (Eq. (4.10)) stability conditions. We perform the same procedure for the experimental setup over a subset of the modulation parameter space, exciting the input mass

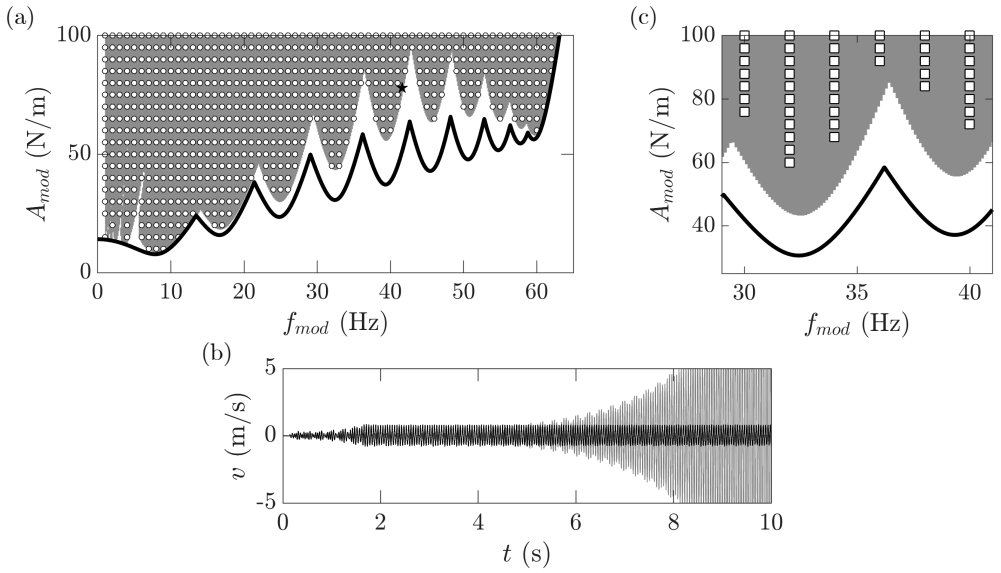

Figure 4.2: Stability of modulation parameters. **(a)** The black curve shows the analytical prediction of the stability boundary based on condition Eq. (4.10). Shaded region indicates unstable solutions for modulation parameter combinations as determined by the Floquet analysis. The white circles indicate parameter combinations for which the fully nonlinear simulation exhibits a non-decaying, modulation-driven response to an initial impulse. The black star indicates the parameters shown in panel (b). **(b)** Numerically simulated velocity output time series for the parameters indicated by the black star in panel (a). The fully nonlinear simulation (black line) has a bounded response, while the linearized simulation (gray line) exhibits exponential growth. **(c)** Experimental non-decaying parameter combinations (white squares). The black curve shows the analytical prediction of the stability boundary based on condition Eq. (4.10). Shaded region indicates unstable solutions for modulation parameter combinations as determined by the Floquet analysis.

($n = 2$) with an impulse and observing decaying or non-decaying responses. The experimental non-decaying region (Fig. 4.2 (c)) shows similarly good agreement with the linear theoretical predictions.

Despite linearization and, in the case of the Mathieu condition, a perturbation method approximate solution, both the Floquet and Mathieu stability conditions accurately predict the ranges of modulation parameters for which a modulation-driven response is observed in the experiment. This suggests that the onset of such modulation-driven response can be predicted, to a degree, by the approximate linear dynamics of the lattice. On the other hand, the nonlinearity is clearly playing an important role in the observed dynamics. As illustrated by Fig. 4.2(b), the nonlinearity has a stabilizing effect, leading to bounded steady-states rather than

unbounded growth as the linear theory predicts. We explore this, and other aspects of nonlinearity, in the next section.

4.6 Nonlinear Lattice Dynamics

Nonlinear states with no external drive

We now further investigate the interplay of the nonlinearity of the system with the extrinsic time modulation. As a particular case example, we fix the modulation frequency to $f_{mod} = 41.6$ Hz, which corresponds to the frequency of the star point in Fig. 4.2(a). At this modulation frequency, the linear theory predicts that the zero state becomes unstable at a modulation amplitude of $A_{mod} \approx 75.2\,\mathrm{N\,m^{-1}}$ (in the fully modulated lattice the prediction is $A_{mod} \approx 50.1\,\mathrm{N\,m^{-1}}$). For modulation amplitudes above the threshold, the response initially grows, but eventually settles to a stable, time periodic state (as suggested by Fig. 4.2(b)). The period of oscillation is twice the period of the modulation period, which corresponds to the frequency of the unstable modes lying in the wavenumber band gap. In order to better understand these nonlinear time-periodic states, we employ a Newton-type procedure to identify them with high precision. Using a Newton method to find time-periodic solutions allows us to identify solutions that are unstable and to compute bifurcation diagrams, which is not possible through direct dynamic simulations, which can only identify stable solutions. To investigate the dynamical stability of the obtained states, a Floquet analysis is used to compute the Floquet multipliers associated with the solutions. Time periodic orbits are computed by finding roots of the map $F := \mathbf{u}(2T_{mod}) - \mathbf{u}(0)$, where $2T_{mod}$ is the period of oscillation, $\mathbf{x}(2T_{mod})$ is the solution of Eq. (2.1) at time $2T_{mod}$ with initial condition $\mathbf{u}(0)$. Roots of this map (and hence time-periodic solutions of Eq. (2.1)) are found via Newton iterations. This requires the Jacobian of F, which is of the form $V(2T_{mod}) - I$, where I is the identity matrix, V is the solution to the N^2 variational equations $\dot{V} = DF \cdot V$ where DF is the Jacobian of the equations of motion evaluated at the given state vector. The stability is computed in the same way as detailed above for the zero state, but with the coefficient matrix given by $A(t)$ being replaced by the Jacobian matrix DF.

Fig. 4.3 shows example solutions obtained with the Newton method with the parameters $f_{mod} = 41.6$ Hz and $A_{mod} = 70\,\mathrm{Nm^{-1}}$. There are two time-periodic solutions found at this parameter set. The panels in the left coloumn correspond to a stable solution and the panels in the right coloumn correspond to an unstable solution. Panel (a) shows the profile of the solution at $t = 0$. The inset shows a plot of the Floquet multipliers in the complex plane. All multipliers lie within the unit circle

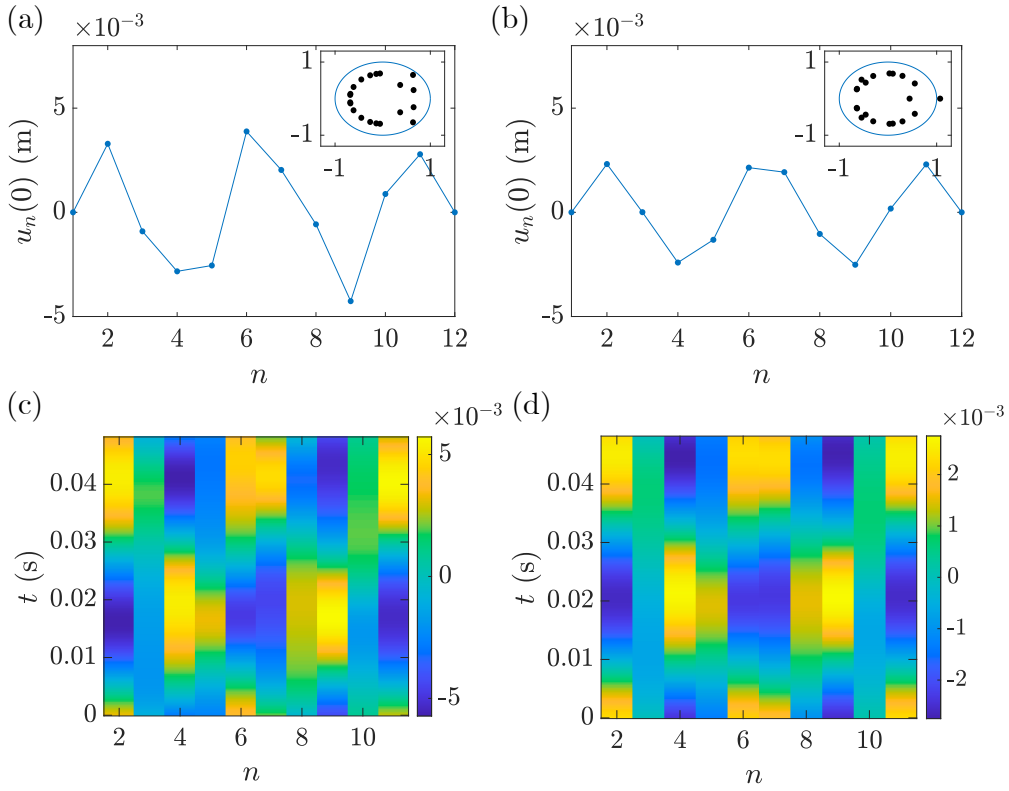

Figure 4.3: Time-periodic solutions of Eq. (2.1) with $f_{mod} = 41.6$ Hz and $A_{mod} = 70$ N m^{-1}. **(a)** Spatial profile of a stable solution. The inset shows the Floquet multiplers. **(b)** Spatial profile of an unstable stable solution. **(c)** Intensity plot of the spatio-temporal evolution of the solution shown in panel (a) for one period of motion (color intensity corresponds to displacement). **(d)** Intensity plot of the spatio-temporal evolution of the solution shown in panel (b) .

(blue solid line in the inset shown) indicating the solution is stable. Panel (c) shows a spatio-temporal intensity plot of the solution over one period of motion, where the oscillating character can been seen. Panel (b) shows the profile of the unstable solution, whose instability is indicated by a Floquet multipler lying outside of the unit circle. Panel (d) shows the corresponding spatio-temporal intensity plot.

We conduct a bifurcation analysis of the nonlinear time-periodic solutions using a pseudo-arclength continuation [14] with the modulation frequency fixed to $f_{mod} = 41.6$ Hz and the modulaiton amplitude A_{mod} as the continuation parameter. The bifurcation diagram is shown in Fig. 4.4(a). The norm of the initial sate of the solution $\|u(0)\| = \sqrt{\sum_n u_n(0)^2}$ is shown on the vertical axis, and the modulaiton amplitude is shown on the horizontal axis. Solid blue lines correspond to stable

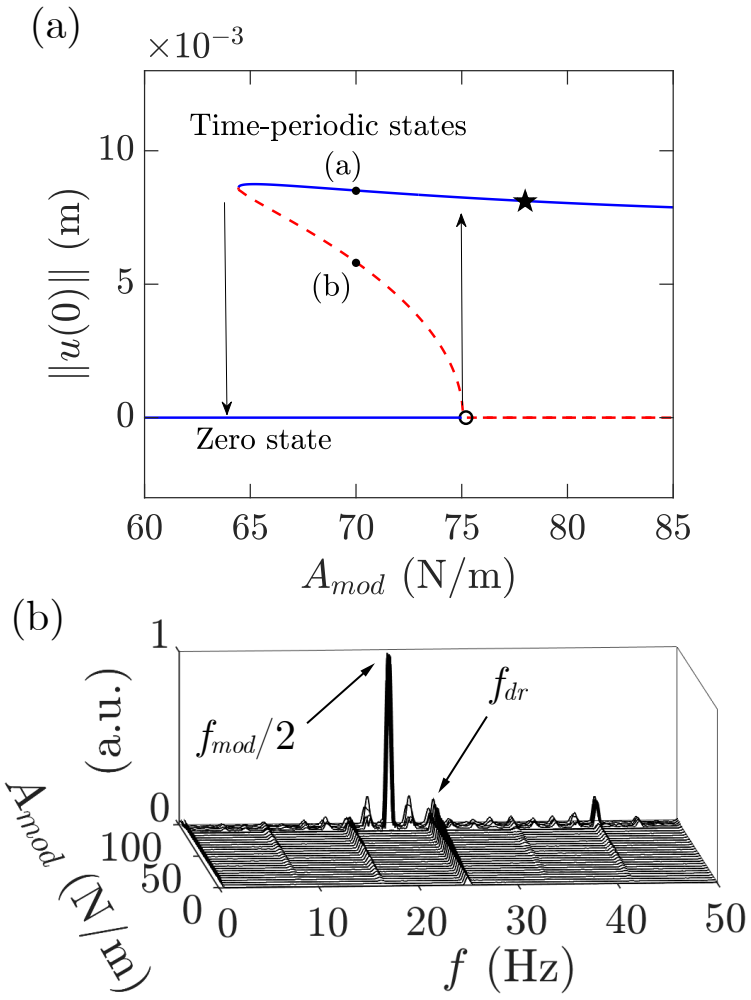

Figure 4.4: Bifurcation analysis. **(a)** Bifurcation diagram with $f_{mod} = 41.6$ Hz fixed showing how time-periodic states bifurcate for the zero state. **(b)** The frequency response of the experimental lattice for fixed amplitude harmonic driving and increasing harmonic modulation. At a critical amplitude, the lattice transitions from a driving-dominated response to a high amplitude, modulation-dominated response.

solutions (all Floquet multiplers have modulus not exceeding unity) and red dashed lines correspond to unstable solutions (at least one Floquet multipler exceeds unity).

In the diagram, the zero state corresponds to the horizontal line at $\|u(0)\| = 0$ m. The zero state is stable until $A_{mod} \approx 75.2$ N m^{-1} (the black circle on panel (a) shows the bifurcation point). This coincides with the prediction based on the linear stability analysis detailed in Section 4.5. An unstable nonlinear time-periodic state bifurcates from the zero state at the critical modulation amplitude $A_{mod} \approx 75.2$ N m^{-1}. This unstable nonlinear time-periodic state remains unstable until it undergoes a saddle-node bifurcation at $A_{mod} \approx 64.44$ N m^{-1} and $\|u(0)\| = .009$ m. The two

solutions shown in Fig. 4.3 correspond to the labels (a) and (b), respectively. This bifurcation implies classic hysteretic behavior is possible. For small modulation amplitudes ($A_{mod} < 75.2$ N m^{-1}), the zero state will be approached. Once the threshold $A_{mod} \approx 75.2$ N m^{-1} is exceeded, the zero state is no longer stable, and a small perturbation to the system (like the impulse studied in the previous section) will result in an initial increase in amplitude. However, in the presence of nonlinearity, there exists a stable, time-periodic state, which the dynamics approach asymptotically. For example, with $A_{mod} = 78$ N m^{-1} (which corresponds to the star in Fig. 4.2(a)) the zero state is unstable, and the thus the stable time-periodic state is approached upon perturbation, see the star in Fig. 4.4(a). Once the time-periodic state is excited, one can gradually decrease the modulation amplitude until the saddle-node bifurcation point. Below this point, the dynamics will once again approach the zero state. The bifurcation diagram also implies a region of bi-stability. Namely, the zero state and a time-periodic orbit is stable in the range $64.44 \lessapprox A_{mod} \lessapprox 75.2$. The bifurcation diagram in the fully modulated lattice is qualitatively similar, but solution curves are shifted, see Fig. 4.5. The bifurcation structure of the time-periodic states in fully modulated lattice with no external drive is similar to the partially modulated lattice, shown in Fig. 4.4(a). The black circle in the figure indicates when the zero-state becomes unstable, according to Eq. (4.10). This point coincides with the numerically computed time-periodic state bifurcating from the zero state.

Nonlinear states in presence of external drive

In the classic paradigm of oscillators with time-independent stiffness, it is well known that presence of damping and external drive can lead to periodic orbits, period-doubling, quasi-periodicity and chaos [44]. The study of spatially extended lattices (with time-independent stiffness) with damping and external drive is an active research area. Some examples include the study of granular crystals [10, 45] and micromechanical oscillator arrays [51]. In such systems, the primary structure is the periodic orbit. Other structures, such as those with higher period, or quasi-periodic ones, typically bifurcate from branches in parameter space consisting of periodic orbits. In this section, we add an external (harmonic) drive to our system with time-dependent stiffness and explore the bifurcations as an underlying parameter is varied. We will demonstrate that the primary structures in the system are quasi-periodic ones, which is in contrast to the periodic ones found in lattices with time-independent stiffness.

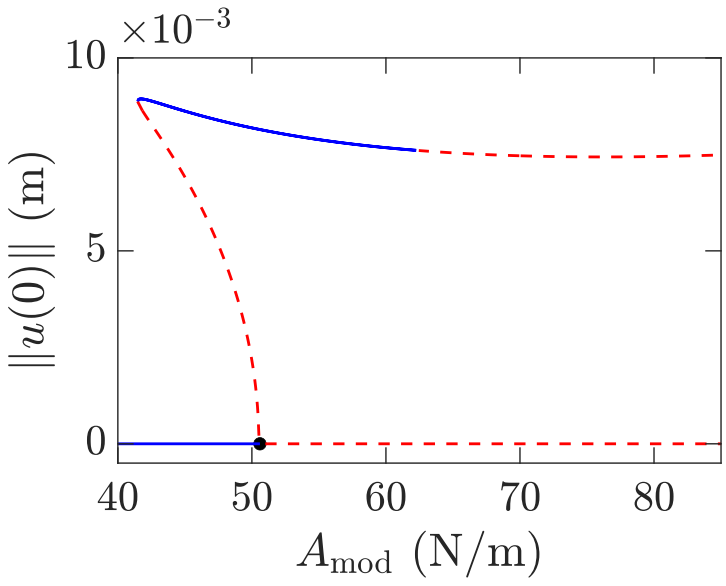

Figure 4.5: Bifurcation diagram with f_{mod} = 41.6 Hz fixed showing how time-periodic states bifurcate for the zero state in the fully modulated lattice.

When the lattice is driven harmonically, and the modulation amplitude is incrementally increased, we observe a transition from a driving-dominated to a modulation-dominated response, as shown in Fig. 4.4(b) for the measured steady state output (mass $n = 2$) velocity. The frequency response shows a sharp transition in dominant frequency component (from driving frequency to half the modulation frequency) and large increase in amplitude. To better understand this, we start by conducting a parametric sweep of the modulation amplitude A_{mod}, both experimentally and numerically. This is a natural parameter to consider for bifurcation studies, since it is expected that larger values of A_{mod} will lead to nonlinear effects. For each value of A_{mod}, the lattice is driven by a harmonic input at one end ($n = 2$), and the output signal is measured at the opposite end ($n = 11$). The velocity response is allowed to reach steady-state and the amplitude of the response is recorded. In particular, the magnitude of the temporal Fourier coefficient associated to the drive frequency f_{dr} and half the modulation frequency $f_{mod}/2$ are recorded. This will indicate if the observed dynamics is due primarily to the drive (i.e., larger Fourier amplitude at $f = f_{dr}$) or the time modulation (i.e., larger Fourier amplitude at $f = f_{mod}/2$). The modulation amplitude is increased by increment ΔA_{mod}, and the response is again allowed to reach steady-state and is recorded. These steps are repeated until the maximum modulation amplitude is reached. We call this procedure the "forward sweep." The "backward sweep" procedure is similar, where

A_{mod} is decreased rather than increased. This process is carried out numerically and experimentally. In particular, for the numerical results, Eq. (2.1) is simulated with the parameters specified in Table 4.1 and with drive frequency $f_{dr} = 25$ Hz and drive amplitude $A_{dr} = 0.15$ N. Similar to Section 4.6, we fix the the modulation frequency $f_{mod} = 41.6$ Hz. Notice that the drive frequency is not a rational multiple of the modulation frequency, which represents a generic choice of these frequencies. The case where one is a rational multiple of the other is briefly discussed below. The range of modulation amplitudes considered is $A_{mod} \in [0, 100]$ N m^{-1} where increments of $\Delta A_{mod} = 2$ N m^{-1} are used in the sweeps. Experimental forward and backward sweep measurements are repeated 4 times with identical driving and modulation parameters, with the exception that the step size is $\Delta A_{mod} \approx 3.75$.

Fig. 4.6 summarizes the results of the modulation amplitude sweeps. In Fig. 4.6(a), the response of the lattice to a forward sweep of modulation amplitude is analyzed. The relative Fourier amplitudes of the drive frequency $f = f_{dr}$ are shown in blue (squares/line) and the Fourier amplitudes of the half modulation frequency $f = f_{mod}/2$ are shown in black (triangles/line). Error bars show standard deviation for experimental measurements. For small modulation amplitudes, the response is completely dominated by harmonic driving dynamics, and the amplitude of oscillations at $f_{mod}/2$ is negligible. Then, at a critical modulation amplitude, the output response transitions sharply from the small displacement, driving signal-dominated regime to a large displacement, modulation-dominated regime, at the sharp jump in the relative amplitude of the $f_{mod}/2$ (black) in Fig. 4.6(a). Fig. 4.6(b) examines the transition between the amplitude jumps in more detail. Since only the modulation-dominated response is necessary to track the transition of the lattice between the two states, Fig. 4.6(b) shows a comparison of the relative Fourier amplitude of $f = f_{mod}/2$, this time for both the forward (black) and backward sweep (gray) of the modulation amplitude A_{mod} near the transition point. Significant hysteresis is observed both in the experiment (markers) and simulation (dashed-lines). This transition occurs at approximately $A_{mod} = 90$ N m^{-1} in the experiments and $A_{mod} = 73$ N m^{-1} in simulation for the forward sweep and $A_{mod} = 60$ N m^{-1} and $A_{mod} = 63$ N m^{-1} for the measured and simulated backward sweep, respectively.

The structure of the solutions in the low amplitude, drive dominated region are simple. They are time-periodic with period given by the period of the drive. The solution structure of the higher amplitude, modulated dominated region is more subtle. To understand this structure, we use Poincaré sections of the output

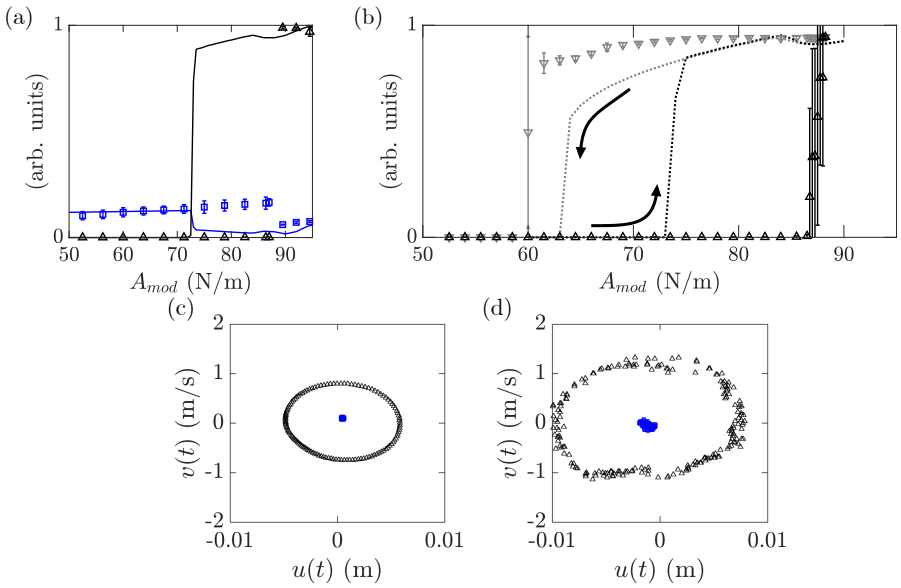

Figure 4.6: Nonlinear lattice dynamics **(a)** Fourier amplitudes for f_{dr} (blue/squares) and $f_{mod}/2$ (black/triangles) versus modulation amplitude for experimental (markers) and numerical simulation (lines). Note that error bars are also shown. **(b)** Hysteresis of $f_{mod}/2$ Fourier component around mode transition, with slowly increasing (black triangles) and decreasing (gray upside down triangles) modulation amplitude. Numerical simulation shown in dashed lines. **(c)** Poincaré section of the output response of the numerical simulation, with sampling period $T = 1/f_{dr}$. Pre- and post- forward sweep transition modulation amplitude responses are shown as blue squares and black triangles, respectively. **(d)** Same as panel (c) for the experiment.

response. A Poincaré section effectively turns a continuous signal into a discrete one by sampling the solution at some fixed time increment, say T [44]. For example, a single point in the Poincaré section would correspond to a periodic orbit with period T of the original time series. Two points in the Poincaré section would correspond to a solution with period $2T$ (period doubling), and a closed loop in the Poincaré section would correspond to a quasi-periodic orbit. To create the Poincaré section the output position u (which is found experimentally by integrating the velocity measured by the LDV) and velocity $v = \frac{du}{dt}$ are plotted in the (u, v) phase plane with a sampling period of $T = 1/f_{dr}$. Both numerical simulation and experimental Poincaré sections are sampled at modulation amplitudes at least one ΔA_{mod} smaller and larger than their respective forward sweep transition points. Fig. 4.6(c) shows the numerically simulated Poincaré section at $A_{mod} = 71\ \mathrm{N\,m^{-1}}$ (blue squares) and $A_{mod} = 75\ \mathrm{N\,m^{-1}}$ (black triangles) and Fig. 4.6(d) shows the experimentally measured Poincaré section at $A_{mod} \approx 80\ \mathrm{N\,m^{-1}}$ (blue squares) and $A_{mod} = 93\ \mathrm{N\,m^{-1}}$ (black triangles). Before

the transition, the plot of the Poincaré sections reveals a single point, indicating the solution is time-periodic. After the transition, the Poincaré sections form an invariant curve in the phase plane, indicating the solution is temporally quasi-periodic. The Poincaré sections confirm what is already suggested in Fig. 4.6(a). Namely, there is a single dominant frequency in the response before the transition (time-periodic response) and there are two non-negligible incommensurate frequencies after the transition (time-quasi-periodic response).

The hysteretic behavior shown in Fig. 4.6 represents a departure in the hysteretic behavior observed in classic nonlinear systems [44]. Typically the main branch of solutions consist of constant or time-periodic solutions. While quasi-periodic orbits can exist in classic oscillator systems, they are typically unstable (see the discussion in [11]). Here we have demonstrated that in large regions in parameter space, the quasi-periodic orbits are stable. The hysteretic behavior, and the region of bi-stability, of Fig. 4.6(b) can be understood in the framework of the previous sections. The reason for this is as follows: In the presence of the external drive, the ground state is no longer the zero state, but rather it is a time-periodic state with frequency identical to the external drive frequency. The quasi-periodic orbit found in the lattice with the external drive results from the combined effect of the nonlinear time-periodic state of the undriven system (discussed in 4.6) with frequency $f_{mod}/2$ and the external drive with frequency f_{dr}. The presence of the two frequencies in the response is what leads to the quasi-periodic motion. With this established, the bifurcation diagram shown in Fig. 4.4(a) will provide a roadmap for understanding bifurcations in the externally driven system. In particular, the analytical approximation for the jump in the forward sweep is $A_{mod} \approx 51.1$ N m^{-1}, which is based on the Mathieu equation stability analysis of the fully modulated lattice detailed in Section 4.5. In the partially modulated lattice (where the first and final node are not modulated), the loss of stability occurs at $A_{mod} \approx 75.2$ N m^{-1}. This theoretical prediction from the linear analysis is very close to the observed jump shown in Fig. 4.6(b), $A_{mod} = 73$ N m^{-1}. Likewise, based on the analysis of Section 4.6 the jump in the backward sweep is predicted to occur at $A_{mod} \approx 64.44$ N m^{-1}, which is close to the observed value of $A_{mod} \approx 63$ N m^{-1}. Thus, the presence of the external drive did not significantly alter the bifurcation structure (compare Figs. 4.4(a) and 4.6(b). The underlying solution structure does, however, change significantly. The zero and time-periodic states in the undriven lattice became time-periodic and quasi-periodic ones in the driven one. The dynamics of a driven lattice with and without drive frequency that is a rational multiple of the modulation

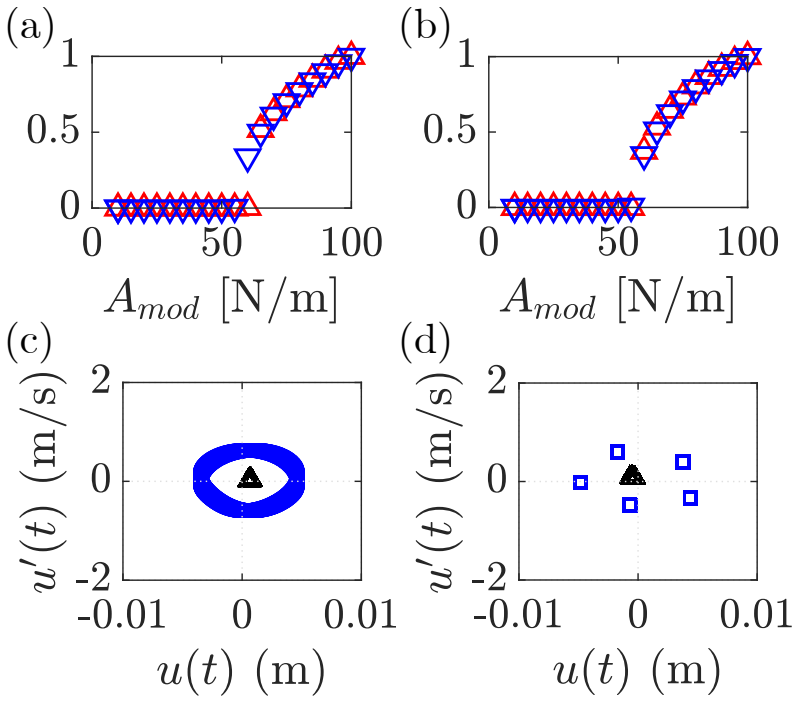

Figure 4.7: Effect of ratio of driving and modulation frequency. **(a),(b)** Forward and backward sweep for driving and modulation frequency combinations that aren't (a) and are (b) rational multiples. **(c),(d)** Poincaré sections for low (black triangles) and high (blue squares) amplitude regime with same frequency combinations as (a) and (b), respectively.

frequency are compared. We show a forward and backward sweep of the modulation amplitude for two cases, first, where the driving frequency is a not rational multiple of the modulation frequency (f_{dr} = 25.77 Hz, f_{mod} = 40 Hz), and second, where the driving frequency is a rational multiple of the modulation frequency (f_{dr} = 25 Hz, f_{mod} = 40 Hz). It is observed that this does not have a significant impact on the hysteresis behavior, as shown Fig. 8 in panels (a) and (b) for the not rational and rational case, respectively. The primary difference is observed in the Poincare sections for the same frequencies (where panel (c) and (d) are correspond to the same frequencies as panels (a) and (b), respectively. The outputs for low (black triangles) and high amplitude (blue squares) modulation regimes, exhibit a quasi-periodic orbit when the frequencies are not rational multiples, while the rational multiple case is periodic.

The stability analysis carried out in Section 4.5 can also help explain the observed discrepancy between the experimental results and simulated results (e.g., the region of bi-stability is slightly larger in the experiment). In Fig. 4.2(a) one sees that the

stability of the lattice with respect to the modulation frequency is very sensitive. In particular, for the modulation frequency f_{mod} = 41.6 Hz used in Fig. 4.6, the linear stability modulation amplitude (A_{mod}) threshold can change by more than 10 N m^{-1} for a change in f_{mod} of ± 1 Hz (see boundary of gray instability region in Fig. 4.2(a)). Therefore, even a small mistuning between the experimental and theoretical frequency could cause significant changes to the transition modulation amplitude.

While additional tuning of the parameters could yield better quantitative agreement, the primary features of nonlinearity and time modulation are captured well by our model with predetermined parameter values.

4.7 Summary and Conclusions

We studied the response of a linear and nonlinear discrete, phononic lattice, consisting of magnetic particles controlled by electromagnetic coils. We excited the lattice at one end and imparted external stiffness modulation at each particle site. In the linear regime, we experimentally reconstructed the dispersion relation of a chain with modulated grounding stiffness, demonstrating the opening of wavenumber band gaps. For larger modulation amplitudes, the nonlinearity of the coupling force between masses admits bounded solutions that would otherwise not be present in a linear system, where the parametric amplification characteristic of this form of extrinsic modulation induces exponential growth. In particular, the nonlinearity of the system allows for the existence of a family of time-periodic states which bifurcate from the zero state when it losses stability. The combination of external drive and time-modulation allows for the creation of stable, large-amplitude time-quasi-periodic solutions that can co-exist with stable, small-amplitude time-periodic ones. This was confirmed both numerically and experimentally, with the experiments showing good qualitative agreement with the numerics.

Our analysis offers validation of the linear dynamics that produce the unique emergent dispersive properties of time-modulated systems, while demonstrating how nonlinearity provides additional flexibility in the design and study of wave propagation time-modulated systems. The findings offer insights on methods to control the propagation of acoustic waves in nonlinear, active systems. Implementing such solutions in small scale devices holds promise for applications in sensing and signal processing, offering frequency agile solutions for tunable filters, delay lines and signal conversion. Such nonlinear phenomena could also be used to compensate

losses and dissipation, thereby allowing the miniaturization of components and the addition of on-chip functionalities.

Acknowledgements

This material is based upon work supported by the US National Science Foundation under Grant Nos. DGE-1745301 (B.L.K.), EFRI-1741565 (C.D.) and DMS-2107945 (C.C.). We thank Prof. Bumki Min and Dr. Jagang Park for helpful discussions.

References

[1] M. H. Ansari, M. A. Attarzadeh, M. Nouh, and M. A. Karami. Application of magnetoelastic materials in spatiotemporally modulated phononic crystals for nonreciprocal wave propagation. *Smart Materials and Structures*, 27(1): 015030, Dec. 2017. ISSN 0964-1726. doi: 10.1088/1361-665X/aa9d3d. URL https://doi.org/10.1088%2F1361-665x%2Faa9d3d.

[2] G. P. Berman and F. M. Izrailev. The Fermi-Pasta-Ulam problem: Fifty years of progress. *Chaos*, 15(1), 2005. ISSN 10541500.

[3] N. Boechler, G. Theocharis, S. Job, P. G. Kevrekidis, M. A. Porter, and C. Daraio. Discrete breathers in one-dimensional diatomic granular crystals. *Physical Review Letters*, 104(24):244302, June 2010. doi: 10.1103/PhysRevLett.104.244302. URL https://link.aps.org/doi/10.1103/PhysRevLett.104.244302.

[4] N. Boechler, G. Theocharis, and C. Daraio. Bifurcation-based acoustic switching and rectification. *Nature Materials*, 10(9):665–668, Sept. 2011. ISSN 1476-4660. doi: 10.1038/nmat3072. URL http://www.nature.com/articles/nmat3072.

[5] N. Boechler, J. Yang, G. Theocharis, P. G. Kevrekidis, and C. Daraio. Tunable vibrational band gaps in one-dimensional diatomic granular crystals with three-particle unit cells. *Journal of Applied Physics*, 109(7):074906, Apr. 2011. ISSN 0021-8979, 1089-7550. doi: 10.1063/1.3556455. URL http://aip.scitation.org/doi/10.1063/1.3556455.

[6] E. Cassedy. Dispersion relations in time-space periodic media part II—Unstable interactions. *Proceedings of the IEEE*, 55(7):1154–1168, July 1967. ISSN 1558-2256. doi: 10.1109/PROC.1967.5775.

[7] E. Cassedy and A. Oliner. Dispersion relations in time-space periodic media: Part I—Stable interactions. *Proceedings of the IEEE*, 51(10):1342–1359, Oct. 1963. ISSN 1558-2256. doi: 10.1109/PROC.1963.2566.

[8] A. L. Chen and Y.-S. Wang. Study on band gaps of elastic waves propagating in one-dimensional disordered phononic crystals. *Physica B: Condensed Matter*, 392(1):369–378, Apr. 2007. ISSN 0921-4526. doi: 10.1016/j.physb.2006.12.004. URL https://www.sciencedirect.com/science/article/pii/S0921452606018746.

[9] Y. Chen, X. Li, H. Nassar, A. N. Norris, C. Daraio, and G. Huang. Nonreciprocal wave propagation in a continuum-based metamaterial with space-time modulated resonators. *Physical Review Applied*, 11(6):064052, June 2019. ISSN 2331-7019. doi: 10.1103/PhysRevApplied.11.064052. URL https://link.aps.org/doi/10.1103/PhysRevApplied.11.064052.

[10] C. Chong and P. G. Kevrekidis. *Coherent Structures in Granular Crystals: From Experiment and Modelling to Computation and Mathematical Analysis*. Springer, New York, 2018.

[11] C. Chong, P. G. Kevrekidis, G. Theocharis, and C. Daraio. Dark breathers in granular crystals. *Physical Review E*, 87:042202, Apr 2013. doi: 10.1103/PhysRevE.87.042202. URL https://link.aps.org/doi/10.1103/PhysRevE.87.042202.

[12] A. L. Cullen. A travelling-wave parametric amplifier. *Nature*, 181(4605):332–332, Feb. 1958. ISSN 1476-4687. doi: 10.1038/181332a0. URL https://www.nature.com/articles/181332a0.

[13] C. Daraio, V. F. Nesterenko, E. B. Herbold, and S. Jin. Energy trapping and shock disintegration in a composite granular medium. *Physical Review Letters*, 96(5):058002, Feb. 2006. doi: 10.1103/PhysRevLett.96.058002. URL https://link.aps.org/doi/10.1103/PhysRevLett.96.058002.

[14] E. Doedel and L. S. Tuckerman. *Numerical Methods for Bifurcation Problems and Large-Scale Dynamical Systems*. Springer-Verlag, Heidelberg, Germany, 2000.

[15] X. Fang, J. Wen, B. Bonello, J. Yin, and D. Yu. Wave propagation in one-dimensional nonlinear acoustic metamaterials. *New Journal of Physics*, 19(5):053007, May 2017. ISSN 1367-2630. doi: 10.1088/1367-2630/aa6d49. URL https://doi.org/10.1088/1367-2630/aa6d49.

[16] E. Fermi, J. Pasta, S. Ulam, and M. Tsingou. Studies of nonlinear problems. Technical report, Los Alamos Scientific Laboratory, May 1955. URL https://www.osti.gov/biblio/4376203.

[17] S. Flach and A. V. Gorbach. Discrete breathers — Advances in theory and applications. *Physics Reports*, 467(1):1–116, 2008. ISSN 0370-1573. doi: https://doi.org/10.1016/j.physrep.2008.05.002. URL https://www.sciencedirect.com/science/article/pii/S0370157308001580.

[18] J. Ford. The Fermi-Pasta-Ulam problem: Paradox turns discovery. *Physics Reports*, 213(5):271–310, May 1992. ISSN 0370-1573. doi: 10.1016/0370-1573(92)90116-H. URL https://www.sciencedirect.com/science/article/pii/037015739290116H.

[19] E. Galiffi, P. Huidobro, and J. Pendry. Broadband nonreciprocal amplification in luminal metamaterials. *Physical Review Letters*, 123(20):206101, Nov. 2019. ISSN 0031-9007, 1079-7114. doi: 10.1103/PhysRevLett.123.206101. URL https://link.aps.org/doi/10.1103/PhysRevLett.123.206101.

[20] G. Gantzounis, M. Serra-Garcia, K. Homma, J. M. Mendoza, and C. Daraio. Granular metamaterials for vibration mitigation. *Journal of Applied Physics*, 114(9):093514, Sept. 2013. ISSN 0021-8979. doi: 10.1063/1.4820521. URL https://aip-scitation-org.caltech.idm.oclc.org/doi/10.1063/1.4820521.

[21] B. M. Goldsberry, S. P. Wallen, and M. R. Haberman. Non-reciprocal wave propagation in mechanically-modulated continuous elastic metamaterials. *The Journal of the Acoustical Society of America*, 146(1):782–788, July 2019. ISSN 0001-4966. doi: 10.1121/1.5115019. URL http://asa.scitation.org/doi/10.1121/1.5115019.

[22] C. S. Huang, S. L. Hung, W. C. Su, and C. L. Wu. Identification of time-variant modal parameters using time-varying autoregressive with exogenous input and low-order polynomial function. *Computer-Aided Civil and Infrastructure Engineering*, 24(7), 2009. ISSN 1467-8667. URL https://onlinelibrary.wiley.com/doi/abs/10.1111/j.1467-8667.2009.00605.x.

[23] R. James, S. M. Woodley, C. M. Dyer, and V. F. Humphrey. Sonic bands, bandgaps, and defect states in layered structures—Theory and experiment. *The Journal of the Acoustical Society of America*, 97(4):2041–2047, Apr. 1995. ISSN 0001-4966. doi: 10.1121/1.411995. URL https://asa.scitation.org/doi/10.1121/1.411995.

[24] P. G. Kevrekidis. *The Discrete Nonlinear Schrödinger Equation: Mathematical Analysis, Numerical Computations and Physical Perspectives*. Springer, New York, 2009.

[25] P. G. Kevrekidis. Non-linear waves in lattices: Past, present, future. *IMA Journal of Applied Mathematics*, 76(3):389–423, 2011. doi: 10.1093/imamat/hxr015.

[26] I. Kovacic, R. Rand, and S. Mohamed Sah. Mathieu's equation and its generalizations: Overview of stability charts and their features. *Applied Mechanics Reviews*, 70(2), 02 2018. ISSN 0003-6900. doi: 10.1115/1.4039144. URL https://doi.org/10.1115/1.4039144. 020802.

[27] A. B. Kozyrev, H. Kim, and D. W. van der Weide. Parametric amplification in left-handed transmission line media. *Applied Physics Letters*, 88(26):264101, June 2006. ISSN 0003-6951. doi: 10.1063/1.2214136. URL https://aip-scitation-org.caltech.idm.oclc.org/doi/10.1063/1.2214136.

[28] N. Kruss and J. Paulose. Nondispersive one-way signal amplification in sonic metamaterials. *Physical Review Applied*, 17(2):024020, Feb. 2022. ISSN 2331-7019. URL https://link.aps.org/doi/10.1103/PhysRevApplied.17.024020.

[29] M. S. Kushwaha, P. Halevi, L. Dobrzynski, and B. Djafari-Rouhani. Acoustic band structure of periodic elastic composites. *Physical Review Letters*, 71(13): 2022–2025, Sept. 1993. doi: 10.1103/PhysRevLett.71.2022. URL https://link.aps.org/doi/10.1103/PhysRevLett.71.2022.

[30] J. N. Kutz. Advanced differential equations: Asymptotics & perturbations. *arXiv:2012.14591 [nlin]*, Dec. 2020. URL http://arxiv.org/abs/2012.14591.

[31] S. Lee, J. Park, H. Cho, Y. Wang, B. Kim, C. Daraio, and B. Min. Parametric oscillation of electromagnetic waves in momentum band gaps of a spatiotemporal crystal. *Photonics Research*, 9(2):142, Feb. 2021. ISSN 2327-9125. doi: 10.1364/PRJ.406215. URL https://www.osapublishing.org/abstract.cfm?URI=prj-9-2-142.

[32] F. Li, C. Chong, J. Yang, P. G. Kevrekidis, and C. Daraio. Wave transmission in time- and space-variant helicoidal phononic crystals. *Physical Review E*, 90(5):053201, Nov. 2014. doi: 10.1103/PhysRevE.90.053201. URL https://link.aps.org/doi/10.1103/PhysRevE.90.053201.

[33] M.-H. Lu, L. Feng, and Y.-F. Chen. Phononic crystals and acoustic metamaterials. *Materials Today*, 12(12):34–42, Dec. 2009. ISSN 1369-7021. doi: 10.1016/S1369-7021(09)70315-3. URL http://www.sciencedirect.com/science/article/pii/S1369702109703153.

[34] K. L. Manktelow, M. J. Leamy, and M. Ruzzene. Weakly nonlinear wave interactions in multi-degree of freedom periodic structures. *Wave Motion*, 51 (6):886–904, Sept. 2014. ISSN 0165-2125. doi: 10.1016/j.wavemoti.2014.03.003. URL https://www.sciencedirect.com/science/article/pii/S0165212514000390.

[35] J. Marconi, E. Riva, M. Di Ronco, G. Cazzulani, F. Braghin, and M. Ruzzene. Experimental observation of nonreciprocal band gaps in a space-time-modulated beam using a shunted piezoelectric array. *Physical Review Applied*, 13(3):031001, Mar. 2020. doi: 10.1103/PhysRevApplied.13.031001. URL https://link.aps.org/doi/10.1103/PhysRevApplied.13.031001.

[36] R. Martínez-Sala, J. Sancho, J. V. Sánchez, V. Gómez, J. Llinares, and F. Meseguer. Sound attenuation by sculpture. *Nature*, 378(6554):241–241, Nov. 1995. ISSN 1476-4687. doi: 10.1038/378241a0. URL https://www.nature.com/articles/378241a0.

[37] M. Molerón, A. Leonard, and C. Daraio. Solitary waves in a chain of repelling magnets. *Journal of Applied Physics*, 115(18):184901, May 2014. ISSN 0021-8979, 1089-7550. doi: 10.1063/1.4872252. URL http://aip.scitation.org/doi/10.1063/1.4872252.

[38] S. Mukherjee and M. C. Rechtsman. Observation of unidirectional solitonlike edge states in nonlinear floquet topological insulators. *Phys. Rev. X*, 11(4): 041057, Dec. 2021. doi: 10.1103/PhysRevX.11.041057. URL https://link.aps.org/doi/10.1103/PhysRevX.11.041057. Publisher: American Physical Society.

[39] R. K. Narisetti, M. J. Leamy, and M. Ruzzene. A perturbation approach for predicting wave propagation in one-dimensional nonlinear periodic structures. *Journal of Vibration and Acoustics*, 132(3), Apr. 2010. ISSN 1048-9002. URL https://doi.org/10.1115/1.4000775.

[40] H. Nassar, H. Chen, A. Norris, and G. Huang. Non-reciprocal flexural wave propagation in a modulated metabeam. *Extreme Mechanics Letters*, 15:97–102, Sept. 2017. ISSN 23524316. doi: 10.1016/j.eml.2017.07.001. URL https://linkinghub.elsevier.com/retrieve/pii/S2352431617300706.

[41] H. Nassar, H. Chen, A. N. Norris, M. R. Haberman, and G. L. Huang. Non-reciprocal wave propagation in modulated elastic metamaterials. *Proceedings of the Royal Society A: Mathematical, Physical and Engineering Science*, 473(2202):20170188, June 2017. ISSN 1364-5021, 1471-2946. doi: 10.1098/rspa.2017.0188. URL http://rspa.royalsocietypublishing.org/lookup/doi/10.1098/rspa.2017.0188.

[42] H. Nassar, X. C. Xu, A. N. Norris, and G. L. Huang. Modulated phononic crystals: Non-reciprocal wave propagation and Willis materials. *Journal of the Mechanics and Physics of Solids*, 101:10–29, Jan. 2017. ISSN 0022-5096. doi: 10.1016/j.jmps.2017.01.010. URL http://www.sciencedirect.com/science/article/pii/S0022509616308997.

[43] H. Nassar, B. Yousefzadeh, R. Fleury, M. Ruzzene, A. Alù, C. Daraio, A. N. Norris, G. Huang, and M. R. Haberman. Nonreciprocity in acoustic and elastic materials. *Nature Reviews Materials*, pages 1–19, July 2020. ISSN 2058-8437. doi: 10.1038/s41578-020-0206-0. URL https://www.nature.com/articles/s41578-020-0206-0.

[44] A. H. Nayfeh and D. T. Mook. *Nonlinear Oscillations*. Wiley and Sons, Weihheim, Germany, 2004.

[45] V. Nesterenko. *Dynamics of Heterogeneous Materials*. Springer-Verlag, New York, 2001. ISBN 1-56720-543-7.

[46] V. F. Nesterenko. Propagation of nonlinear compression pulses in granular media. *Journal of Applied Mechanics and Technical Physics*, 24(5):733–743, Sept. 1983. ISSN 1573-8620. doi: 10.1007/BF00905892. URL https://doi.org/10.1007/BF00905892.

[47] D. A. Powell, I. V. Shadrivov, and Y. S. Kivshar. Multistability in nonlinear left-handed transmission lines. *Applied Physics Letters*, 92(26):264104, June 2008. ISSN 0003-6951. doi: 10.1063/1.2955531. URL https://aip-scitation-org.caltech.idm.oclc.org/doi/10.1063/1.2955531.

[48] D. A. Powell, I. V. Shadrivov, and Y. S. Kivshar. Asymmetric parametric amplification in nonlinear left-handed transmission lines. *Applied Physics Letters*, 94(8):084105, Feb. 2009. ISSN 0003-6951. doi: 10.1063/1.3089842. URL https://aip-scitation-org.caltech.idm.oclc.org/doi/10.1063/1.3089842.

[49] J. R. Reyes-Ayona and P. Halevi. Observation of genuine wave vector (k or β) gap in a dynamic transmission line and temporal photonic crystals. *Applied Physics Letters*, 107(7):074101, Aug. 2015. ISSN 0003-6951, 1077-3118. doi: 10.1063/1.4928659. URL http://aip.scitation.org/doi/10.1063/1.4928659.

[50] J. A. Richards. Stability diagram approximation for the lossy Mathieu equation. *SIAM Journal on Applied Mathematics*, 30(2):240–247, Mar. 1976. ISSN 0036-1399. doi: 10.1137/0130025. URL https://epubs.siam.org/doi/abs/10.1137/0130025.

[51] M. Sato, B. E. Hubbard, and A. J. Sievers. *Colloquium*: Nonlinear energy localization and its manipulation in micromechanical oscillator arrays. *Rev. Mod. Phys.*, 78:137, 2006.

[52] M. Serra-Garcia, M. Molerón, and C. Daraio. Tunable, synchronized frequency down-conversion in magnetic lattices with defects. *Philosophical Transactions of the Royal Society A: Mathematical, Physical and Engineering Sciences*, 376(2127):20170137, Aug. 2018. doi: 10.1098/rsta.2017.0137. URL https://royalsocietypublishing-org.caltech.idm.oclc.org/doi/10.1098/rsta.2017.0137.

[53] M. Soljačić, M. Ibanescu, S. G. Johnson, Y. Fink, and J. D. Joannopoulos. Optimal bistable switching in nonlinear photonic crystals. *Physical Review E*, 66(5):055601, Nov. 2002. doi: 10.1103/PhysRevE.66.055601. URL https://link.aps.org/doi/10.1103/PhysRevE.66.055601.

[54] Y. Starosvetsky, K. R. Jayaprakash, M. A. Hasan, and A. F. Vakakis. *Dynamics and Acoustics of Ordered Granular Media*. World Scientific, Singapore, 2017.

[55] G. Theocharis, N. Boechler, P. G. Kevrekidis, S. Job, M. A. Porter, and C. Daraio. Intrinsic energy localization through discrete gap breathers in one-dimensional diatomic granular crystals. *Physical Review E*, 82(5):056604, Nov. 2010. doi: 10.1103/PhysRevE.82.056604. URL https://link.aps.org/doi/10.1103/PhysRevE.82.056604.

[56] P. K. Tien and H. Suhl. A traveling-wave ferromagnetic amplifier. *Proceedings of the IRE*, 46(4):700–706, Apr. 1958. ISSN 2162-6634. doi: 10.1109/JRPROC.1958.286770.

[57] M. Toda. Wave propagation in anharmonic lattices. *Journal of the Physical Society of Japan*, 23(3):501–506, Sept. 1967. ISSN 0031-9015. doi: 10.1143/JPSJ.23.501. URL https://journals.jps.jp/doi/10.1143/JPSJ.23.501.

[58] D. Torrent, W. J. Parnell, and A. N. Norris. Loss compensation in time-dependent elastic metamaterials. *Physical Review B*, 97(1):014105, Jan. 2018. ISSN 2469-9950, 2469-9969. doi: 10.1103/PhysRevB.97.014105. URL https://link.aps.org/doi/10.1103/PhysRevB.97.014105.

[59] G. Trainiti and M. Ruzzene. Non-reciprocal elastic wave propagation in spatiotemporal periodic structures. *New Journal of Physics*, 18(8):083047, Aug. 2016. ISSN 1367-2630. doi: 10.1088/1367-2630/18/8/083047. URL https://iopscience.iop.org/article/10.1088/1367-2630/18/8/083047/meta.

[60] G. Trainiti, Y. Xia, J. Marconi, G. Cazzulani, A. Erturk, and M. Ruzzene. Time-periodic stiffness modulation in elastic metamaterials for selective wave filtering: Theory and experiment. *Physical Review Letters*, 122(12):124301, Mar. 2019. ISSN 0031-9007, 1079-7114. doi: 10.1103/PhysRevLett.122.124301. URL https://link.aps.org/doi/10.1103/PhysRevLett.122.124301.

[61] J. O. Vasseur, P. A. Deymier, B. Chenni, B. Djafari-Rouhani, L. Dobrzynski, and D. Prevost. Experimental and theoretical evidence for the existence of absolute acoustic band gaps in two-dimensional solid phononic crystals. *Physical Review Letters*, 86(14):3012–3015, Apr. 2001. ISSN 0031-9007. doi: 10.1103/PhysRevLett.86.3012.

[62] J. Vila, R. K. Pal, M. Ruzzene, and G. Trainiti. A Bloch-based procedure for dispersion analysis of lattices with periodic time-varying properties. *Journal of Sound and Vibration*, 406:363–377, Oct. 2017. ISSN 0022-460X. doi: 10.1016/j.jsv.2017.06.011. URL http://www.sciencedirect.com/science/article/pii/S0022460X17304777.

[63] S. P. Wallen and M. R. Haberman. Nonreciprocal wave phenomena in spring-mass chains with effective stiffness modulation induced by geometric nonlinearity. *Physical Review E*, 99(1):013001, Jan. 2019. ISSN 2470-0045,

2470-0053. doi: 10.1103/PhysRevE.99.013001. URL https://link.aps.org/doi/10.1103/PhysRevE.99.013001.

[64] F. Y. Wang, G. X. Li, H. L. Tam, K. W. Cheah, and S. N. Zhu. Optical bistability and multistability in one-dimensional periodic metal-dielectric photonic crystal. *Applied Physics Letters*, 92(21):211109, May 2008. ISSN 0003-6951, 1077-3118. doi: 10.1063/1.2938060. URL http://aip.scitation.org/doi/10.1063/1.2938060.

[65] Y. Wang, B. Yousefzadeh, H. Chen, H. Nassar, G. Huang, and C. Daraio. Observation of nonreciprocal wave propagation in a dynamic phononic lattice. *Physical Review Letters*, 121(19):194301, Nov. 2018. ISSN 0031-9007, 1079-7114. doi: 10.1103/PhysRevLett.121.194301. URL http://arxiv.org/abs/1803.11503.

[66] Y.-Z. Wang, F.-M. Li, and Y.-S. Wang. Influences of active control on elastic wave propagation in a weakly nonlinear phononic crystal with a monoatomic lattice chain. *International Journal of Mechanical Sciences*, 106:357–362, Feb. 2016. ISSN 0020-7403. doi: 10.1016/j.ijmecsci.2015.12.004. URL https://www.sciencedirect.com/science/article/pii/S002074031500421X.

[67] C.-P. Wen, W. Liu, and J.-W. Wu. Tunable terahertz optical bistability and multistability in photonic metamaterial multilayers containing nonlinear dielectric slab and graphene sheet. *Applied Physics A*, 126(6):426, June 2020. ISSN 0947-8396, 1432-0630. doi: 10.1007/s00339-020-03606-2. URL https://link.springer.com/10.1007/s00339-020-03606-2.

[68] W.-C. Xie. *Dynamic Stability of Structures*. Cambridge University Press, June 2006. ISBN 978-0-521-85266-1.

[69] X. Zhu, J. Li, C. Shen, X. Peng, A. Song, L. Li, and S. A. Cummer. Nonreciprocal acoustic transmission via space-time modulated membranes. *Applied Physics Letters*, 116(3):034101, Jan. 2020. ISSN 0003-6951, 1077-3118. doi: 10.1063/1.5132699. URL http://aip.scitation.org/doi/10.1063/1.5132699.

Chapter 5

MODULATION INSTABILITY AND WAVENUMBER GAP BREATHERS IN A TEMPORALLY LAYERED LATTICE

Research presented in this chapter has been adapted from the following publication:

> Christoper Chong, Brian L. Kim, Evelyn Wallace, and Chiara Daraio. Modulation instability and wavenumber gap breathers in a temporally layered lattice. *In preparation*, 2023.

5.1 Preamble

In this chapter, we continue to investigate the stability of the phononic lattice with time-periodic elastic properties. Now, a square wave modulation is chosen because its closed form solution permits a deeper insight into how system parameters affect stability, especially with respect to the behavior of eigenmodes of the finite discrete lattice located inside or outside regions of instability. We verify linear analytical predictions and full numerical simulations with experimental measurements. Next, because of the nonlinearity of the lattice, we consider the temporal analog of the discrete breather, a wavenumber bandgap breather that is localized in time and periodic in space. We search experimentally for such solutions, and compare measurements to simulations in which temporal breathers are observed. This evidence presents a significant demonstration of a type of nonlinear mechanical phenomenon that could see use in signal processing and metrology applications.

5.2 Introduction

The classical discrete breather is defined as a spatially localized, time-periodic solution of a nonlinear lattice differential equation. They have been studied in many scientific areas, including optical waveguide arrays [10], Josephson-junction ladders [2, 15], dynamical models of the DNA double strand [14], Bose–Einstein condensates in optical lattices [11], and many others. See the review articles [5–7] for a summary of results concerning breathers in lattices. One of the mechanisms in which breathers can manifest is through the modulation instability (MI) of plane waves. The breathers bifurcate from the linear modes at the edge of the linear spectrum and can be continued into the spectral gap [6]. In the context of photonic systems, such solutions have also been called gap solitons, since the frequency ω of

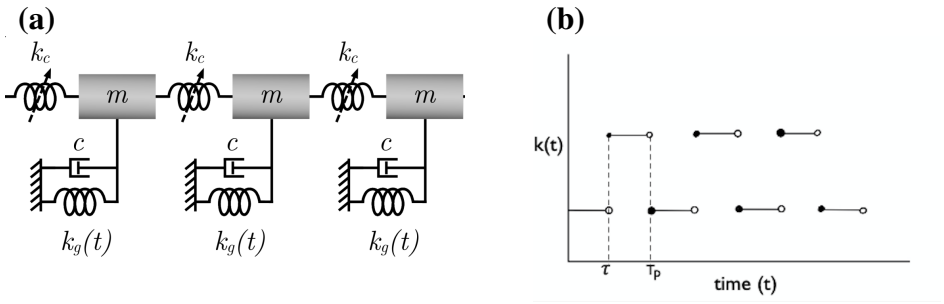

Figure 5.1: Lattice model and modulation. **(a)** Schematic of the mass-spring lattice model with nonlinear coupling stiffness A, time-varying grounding stiffness $k(t)$, and viscous damping c **(b)** Plot of the step-function $k(t)$.

the solution lies in the spectral gap [9]. Spatial periodicity of the lattice can induce spectral gaps.

A new direction that has seen significant recent attention are breathers that are localized in time, and periodic in space. In photonic systems, such solutions have been found that have a wavenumber, k, that lie in a wavenumber band-gap. Such solutions have been called k-gap solitons [1, 13]. The phononic anologue of k-gap solitons, which we will call k-gap breathers, are less explored [3, 42].

In this chapter, we characterize the stability of a temporally layered phononic lattice for both damped and undamped cases, comparing the behavior of long, approximately infinite, discrete lattices to short discrete lattices, wherein unstable regions may not always contain an eigenmode. We verify the stability predictions experimentally, and then use the analytical linear spectrum to find wavenumber band gap breathers.

Model Equations

The lattice is modeled as a nonlinear coupled oscillator [8, 16]

$$M\ddot{u}_n = A\left(d + u_n - u_{n-1}\right)^{-\alpha} - A\left(d + u_{n+1} - u_n\right)^{-\alpha} - k(t)\,u_n - c\dot{u}_n, \tag{5.1}$$

where u_n is the displacement ($[u]$ = m) of the nth ring magnet from its equilibrium position, where the equilibrium distance between adjacent magnets is d ($[d]$ = m). The indices run from $n = 1 \ldots N-1$ and we consider fixed boundary conditions $u_0(t) = u_N(t) = 0$. All ring magnets have uniform mass m. Dissipative forces are modeled with a phenomenological viscous damping term $c\frac{du_n}{dt}$ where the damping coefficient c ($[c]$ = Ns/m) is determined as in Section 2.2 The coupling force term is defined using the repulsive magnetic force between neighboring masses. The

Table 5.1: Lattice Model Parameters

Measured		Fit	
Parameter	Value	Parameter	Value
M	0.0097 [kg]	c	0.15 [N.s/m]
d	33.4 [mm]	K	87.03 [N/m]
$f_{mod} = \frac{\omega}{2\pi}$	$\in$ [1 70] [Hz]	A	9.044×10^{-7}Nm^4
		k_b	$\in$ [0 150] [N/m]

experimentally measured force-distance relation between neighboring masses is fit with a dipole-dipole approximation, as in [16], and is given by $Ax^{-\alpha}$, where x is the center-to-center distance between masses.

A periodic step function is applied to the electromagnetic coils, which induces a grounding stiffness modulation of the form

$$k(t) = \begin{cases} k_a & 0 \le t < \tau T \\ k_b & \tau T \le t < T \end{cases}, \tag{5.2}$$

where we assume that $k(t)$ is periodic with period T, namely, $k(t) = k(t+T)$ for all t, see Fig. 5.1. The step values k_a, k_b and duty-cycle $0 < \tau < 1$ ($[\tau] = $ s) are tuning parameters.

See Section 2.1 for more details of the experimental setup. Table 5.1 summarizes the parameters used throughout this chapter.

5.3 Modulation Instability

We first consider the linearized dynamics,

$$M\ddot{u}_n = K(u_{n-1} - 2u_n + u_{n+1}) - k(t)u_n - c\dot{u}_n, \tag{5.3}$$

where $K = \alpha A d^{\alpha-1}$. The linearized equation is obtained by keeping the linear terms in the Taylor expansion of the nonlinear coupling force $A(d+y)^{-\alpha}$, where it is assumed that $|y| = |u_n - u_{n-1}| \ll d$ for $n = 1 \dots N-1$. We will now derive an exact condition for stability in this equation, discussing first the case of no damping ($c = 0$) before moving on to the damped lattice case.

Undamped Case

Making the ansatz $u_n(t) = X_m(n) \cdot \Theta_m(t)$, one finds upon substitution into Eq. (5.3) that the spatial and temporal parts satisfy, respectively,

$$\lambda_m X_m(n) = -X_m(n-1) + 2X_m(n) - X_m(n+1), \tag{5.4}$$

$$\ddot{\Theta}_m = \frac{-\lambda_m K - k(t)}{M}\Theta_m. \tag{5.5}$$

The eigenvalue problem Eq. (5.4) subject to the Dirichlet boundary conditions $X(0) = X(N) = 0$ has the eigenvalues $\lambda_m = 4\sin^2(q_m/2)$ where the wavenumber is $q_m = m\pi/N$ with $m = 1, \ldots N-1$. The associated eigenfunctions are $X_m(n) = \sin(q_m n)$. Equation (5.5) has the form of a Hill's equation when $k(t)$ is assumed to be periodic [12]. Even though this equation is linear, for general periodic modulation terms $k(t)$, there is no closed form solution in terms of elementary functions. This is true even in the simple case of a harmonic modulation, in which case Eq. (5.5) has the form of a Mathieu equation [12]. However, in the case that the modulation coefficient is given by a step-function (see Eq. (5.2)), we can obtain an exact solution and stability condition. To motivate the approach to achieve this, consider that the general solution of the Hill's equation will be a superposition of functions of the form

$$\Theta_m(t) = H_m(t)e^{i\omega_m t} \tag{5.6}$$

where $H_m(t)$ is a function with the same period as $k(t)$ and $\pm i\omega_m$ is a Floquet exponent [12]. Due to the symmetries of Eq. (5.5) (which has no damping), ω_m will either be real, in which case the underlying solution will be stable, or ω_m will be purely imaginary, in which case the underlying solution will be unstable. The general solution of Eq. (5.3) will thus be unstable, since it is simply a superposition of the $N-1$ solutions of the form $X_m(n)\cdot\Theta_m(t)$.

We will now find an expression that will indicate if ω_m is real, or purely imaginary, which will be our stability condition. We suppose that $H_m(t)$ is a piece-wise function with period T,

$$H_m(t) = \begin{cases} H_{a,m}(t) & 0 \le t < \tau T \\ H_{b,m}(t) & \tau T \le t < T \end{cases}, \quad H_m(t+T) = H_m(t) \quad \text{for all } t. \tag{5.7}$$

Upon substitution of equation (5.6) into equation (5.5) we obtain for $0 \le t < \tau T$,

$$0 = \left(\frac{\lambda_m K + k_a}{M} - \omega_m^2\right) H_{a,m}(t) + 2i\omega_m \dot{H}_{a,m}(t) + \ddot{H}_{a,m}(t), \tag{5.8}$$

and for $\tau T \le t < T$ we have

$$0 = \left(\frac{\lambda_m K + k_b}{M} - \omega_m^2\right) H_{b,m}(t) + 2i\omega_m \dot{H}_{b,m}(t) + \ddot{H}_{b,m}(t). \tag{5.9}$$

Equations (5.8) and (5.9) have the general solutions, respectively,

$$H_{a,m}(t) = e^{-i\omega_m t}\left(A\cos\left(s_{a,m}t\right) + B\sin\left(s_{a,m}t\right)\right), \qquad s_{a,m} = \sqrt{\frac{\lambda_m K + k_a}{M}}, \tag{5.10}$$

$$H_{b,m}(t) = e^{-i\omega_m t}\left(C\cos\left(s_{b,m}t\right) + D\sin\left(s_{b,m}t\right)\right), \qquad s_{b,m} = \sqrt{\frac{\lambda_m K + k_b}{M}}, \quad (5.11)$$

where A, B, C, D are arbitrary constants. Demanding that $H_m(t)$ is continuous and differentiable at $t = 0$ and $t = \tau$ leads to the following four conditions:

$$\begin{aligned} 0 = {} & e^{-i\omega_m\tau T}\cos(s_{a,m}\tau T)A + e^{-i\omega_m\tau T}\sin(s_{a,m}\tau T)B \\ & -e^{-i\omega_m\tau T}\cos(s_{b,m}\tau T)C - e^{-i\omega_m\tau T}\sin(s_{b,m}\tau T)D, \end{aligned}$$

$$0 = A - e^{-i\omega_m T}C\cos(s_{b,m}T) - e^{-i\omega_m T}D\sin(s_{b,m}T),$$

$$\begin{aligned} 0 = {} & -e^{-i\omega_m\tau T}(s_{a,m}\sin(s_{a,m}\tau T) + i\omega_m\cos(s_{a,m}\tau T))A \\ & +e^{-i\omega_m\tau T}(s_{a,m}\cos(s_{a,m}\tau T) - i\omega_m\sin(s_{a,m}\tau T))B \\ & +e^{-i\omega_m\tau T}(s_{b,m}\sin(s_{b,m}\tau T) + i\omega_m\cos(s_{b,m}\tau T))C \\ & -e^{-i\omega_m\tau T}(s_{b,m}\cos(s_{b,m}\tau T) - i\omega_m\sin(s_{b,m}\tau T))D, \end{aligned}$$

$$\begin{aligned} 0 = {} & -i\omega_m A + Bs_{a,m} + Ce^{-i\omega_m T}(s_{b,m}\sin(s_{b,m}T) + i\omega_m\cos(s_{b,m}T)) \\ & -De^{\omega_m T}(s_{b,m}\cos(s_{b,m}T) - i\omega_m\sin(s_{b,m}T)). \end{aligned}$$

The above system of homogeneous linear equations for (A, B, C, D) has non-trivial solutions only if its determinant vanishes. This condition leads to the following equation for ω_m

$$\begin{aligned} \cos(\omega_m T) = {} & -\frac{s_{a,m}^2 + s_{b,m}^2}{2s_{a,m}s_{b,m}}\sin(s_{a,m}\tau T)\sin(s_{b,m}(1-\tau)T) \\ & +\cos(s_{a,m}\tau T)\cos(s_{b,m}(1-\tau)T), \\ \equiv {} & G(q, k_a, k_b, \tau, T). \end{aligned} \quad (5.12)$$

Since the magnitude of the left-hand side of this equation cannot exceed unity for real ω, we have a condition for instability. In particular $|G| > 1$ implies that ω must be imaginary and thus the underlying solution is unstable. This result is similar to those obtained in photonic systems [4].

The wavenumbers that are responsible for the transition from stability in the unmodulated lattice ($k_a = k_b = 0$) to instability in the modulated lattice ($k_b \neq 0 \neq k_b$) occur precisely when $|G(q, 0, 0, \tau, T)|$ intersects unity tangentially. In the zero-amplitude limit ($k_a = k_b = 0$) the expression G simplifies considerably. In particular we have that $G(q, 0, 0, \tau, T) = \cos(\omega_d(q)T)$, where $\omega_d(q)$ is the dispersion relation of the unmodulated lattice. This is consistent with the obvious fact that the Floquet

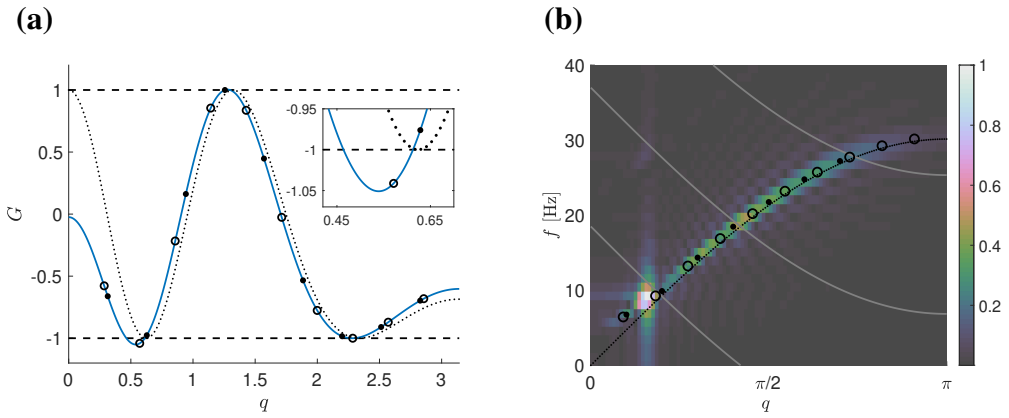

Figure 5.2: Stability and dispersion for square wave modulation. **(a)** Plot of the function G from Eq. (5.12) (solid blue line) in the modulated $k \neq 0$ and unmodulated lattice (black dashed line). The solid dots and open circles are the wavenumbers in the finite sized system with $N = 10$ and $N = 11$, respectively. **(b)** Dispersion relation corresponding to parameters in Table 5.1 with $f_{mod} = 18.5$ Hz. The markers are the imaginary part of the Floquet multiplers for $N = 10$ (solid dots) and for $N = 11$ (open circles). The black-dahsed line is the unmodulated dispersion curve, and the light gray curves are shifts of the dispersion curve $\pm f(q) \pm m f_{mod}$, where m is an integer. The color intensity in the background is the 2D FFT of a the signal resulting by applying a chirp at the left boundary in the $N = 200$ lattice, which detects unstable wavevnumbers near $q \approx 0.5$.

exponents in the limit of zero modulation amplitude approach the dispersion curve (where Eq. (5.12) reduces to $\cos(\omega_m T) = \cos(\omega_d(q_m)T)$). A plot of $G(q, 0, 0, \tau, T)$ (i.e., the unmodulated lattice) as a function of the wavenumber $q \in [0, \pi]$ is shown in Fig. 5.2(a) with the parameter values in table 5.1 (see black dotted line). The blue solid line in this plot shows $G(q, k_a, k_b, \tau, T)$ (the modulated lattice). There are three regions where the magnitude G exceeds unity (near $q = 0.5$, $q = 1.28$, $q = 2.28$) in the modulated case. For a finite lattice with $N - 1$ nodes, the relevant values of G will simply be for $q = q_m = m\pi/N$ for $m = 1, \ldots, N-1$. Thus, whether one of these discrete wave numbers falls into a region of instability will depend on the lattice size. For example, with $N = 10$ all wavenumbers lead to $|G|$ values that do not exceed unity (see filled in black discs in Fig. 5.2) but for $N = 11$ there is one wavenumber that falls into a region of instability (see empty circles in Fig. 5.2(a)). The unstable wavenumber in this case is $q_2 = 2\pi/11 \approx 0.5712$. A zoom of the region near the unstable wavenumber is shown in the inset of Fig. 5.2(a). In this inset, one sees the unstable wavenumber q_2 for $N = 11$ (the empty circle) a stable wavenumber q_2 for $N = 10$ (the black disc) and the vertex of the unmodulated G

function, which indicates the critical wavenumber that leads to instability once the modulation is turned on.

We also simulated the equations of motion in a large lattice ($N = 200$) with zero initial conditions and a chirped boundary on the left covering the frequencies $[0, 50]$ Hz. A PSD of the resulting velocity is computed, see the intensity plot in Fig. 5.2(b). Large intensities are found precisely where the Floquet multiplers live in the wavenumber-frequency plane. In particular the largest intensity is found near the unstable wavenumbers $q \in [0.465, 0.612]$ (namely, where $|G|$ exceeds unity). On this graph, the Floquet exponents ω_m are superimposed for the case of $N = 10$ (black discs) and $N = 11$ (empty circles), where we again see that the $N = 10$ Floquet exponents "miss" the unstable (high intensity) regions.

Note that the expression $G(q, 0, 0, \tau, T) = \cos(\omega_d(q)T)$ implies that the transition to instability will occur when $\omega_d(q) = j\omega_{mod}/2$ where j is an integer and $\omega_{mod} = 2\pi/T$ is the modulation frequency. This reproduces the well-known result that instability occurs in general time periodic modulated lattices when the dispersion relation intersects itself when shifted by $j\omega_{mod}$. In Fig. 5.2(b) a plot of the dispersion relation f_d is shown (block doted curve), where $f_d = \omega_d/2\pi$, along with the curves $-f_d + f_{mod}$, $-f_d + 2f_{mod}$, and $-f_d + 3f_{mod}$. The three intersections shown in the plot are the regions where instability manifests, and corresponds to the three critical points of $G(0, 0)$ shown in Fig. 5.2(a), namely near $q = 0.5$, $q = 1.28$, $q = 2.28$.

To validate the stability condition based on Eq. (5.12), we numerically integrate Eq. (5.3) under a few sets of initial conditions. Using the parameter set in Table5.1 (which corresponds to the parameter set for the solid blue curve of Fig. 5.2(a)) and an initial velocity $\dot{u}_1 = 1$ m/s imposed on the first node, and zero initial conditions are used otherwise. The result of this simulation with lattice size $N = 10$ is shown in Fig. 5.3(a), where it is seen that the dynamics are stable. The same simulation in a lattice with size $N = 11$ is shown in Fig. 5.3(b), where the dynamics appear to be unbounded (unstable). For $N = 10$ the expression $|G|$ is less than unity (see black discs of Fig. 5.2) and hence the solution is predicted to be stable, which is consistent with the simulation shown in Fig. 5.3(a). For $N = 11$ the expression $|G|$ exceeds unity (see open circle near $q = 0.5$ of Fig. 5.2) and hence the solution is predicted to be unstable, which is consistent with the simulation shown in Fig. 5.3(b). Although solutions with generic initial data will be unstable for this parameter set with $N = 11$, one can also select initial data corresponding to stable wavenumbers. For example, conducting a simulation once again with the same parameter set and $N = 11$ (which

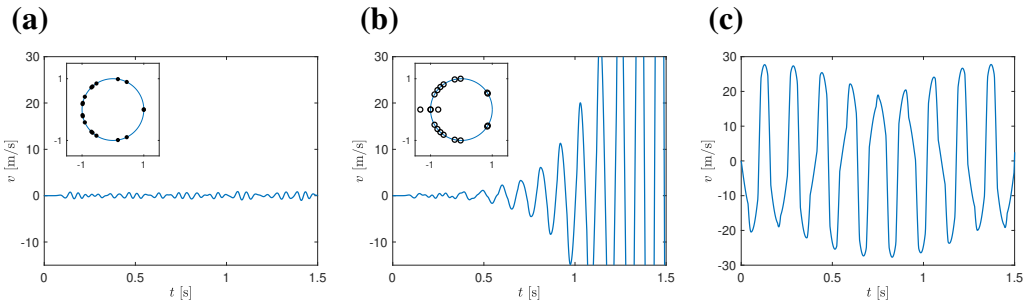

Figure 5.3: Stable and unstable solutions in finite lattices. **(a)** Simulation with $\dot{u}_1 = 1$ m/s and zero initial conditions otherwise in the $N = 10$ lattice. The inset shows the corresponding Floquet multiplers of the system, showing the dynamics are stable. **(b)**, same as panel (a) but in a lattice of size $N = 11$, where the dynamics are unstable. **(c)** Simulation in an unstable lattice, but initiated with a stable wavenumber $u_n(0) = \sin(q_1 n)$. The dynamics are stable, since only the stable mode is excited.

is generically unstable) but with the initial condition $u_n(0) = \sin(q_1 n)$, $\dot{u}_n(0) = 0$ leads to stable dynamics, see Fig. 5.3(c). This is due to the fact that the expression $|G(q = q_1)| < 1$, where $q_1 = \pi/11$ is the first wavenumber (see first empty circle of Fig. 5.2(a)).

The corresponding Floquet multipliers associated to the lattice sizes $N = 10$ and $N = 11$ are shown in the insets of Fig. 5.3 (a) and (b), respectively. A Floquet multiplier is defined as $\rho_m = \exp(i\omega_m T)$ where $i\omega_m$ is a Floquet exponent and T is the period of modulation. A Floquet multipler with modulus greater than unity implies instability. In Fig. 5.3 (a) all Floquet multiliers lie on the unit circle, implying stability, which is consistent with the simulation shown in the main panel of Fig. 5.3 (a). In Fig. 5.3 (b) there is a pair of Floquet multiliers that lie off the unit circle, implying instability, which is again consistent with the simulation shown in the main panel of Fig. 5.3 (b). Note, the real part of the Floquet multipler is identical to the expression G.

Damped Case

In the presence of damping ($c \neq 0$), the temporal part of the separated solution $\Theta_m(t)$ satisfies

$$\ddot{\Theta}_m = \frac{-\lambda_m K - k(t)}{M}\Theta_m - \frac{c}{M}\dot{\Theta}_m, \tag{5.13}$$

where the eigenvalues λ_m remain unchanged. In the presence of the damping term, we cannot assume that the existence of a Floquet exponent with real part implies

instability. Thus, a slightly more general form of the solution is assumed

$$\Theta_m(t) = H_m(t)e^{\mu_m t}, \tag{5.14}$$

where $\mu_m = \sigma_m + i\omega_m$ is the Floquet exponent where $\sigma_m, \omega_m \in \mathbb{R}$. Note, this is in contrast to the previous subsection where ω_m was allowed to be imaginary, which made the analysis slightly simpler. Here, we have dedicated terms for the real and imaginary part of the Floquet exponent, with $\sigma_m > 0$ implying instability. Following the process described in the previous section with the modified ansatz given by (5.14), we find the following equation

$$\begin{aligned} \exp\left[-\left(\sigma_m + \frac{c}{2M}\right)T\right](\cos(\omega_m T) - i\sin(\omega_m T)) + \\ \exp\left[\left(\sigma_m + \frac{c}{2M}\right)T\right](\cos(\omega_m T) + i\sin(\omega_m T)) \quad = 2G_c, \end{aligned} \tag{5.15}$$

where G_c has the same definition as G in Eq. (5.12), but with,

$$s_a = \frac{1}{2}\sqrt{\frac{4\left(\lambda_m \cdot K + k_a\right)}{M} - \left(\frac{c}{M}\right)^2}, \qquad s_b = \frac{1}{2}\sqrt{\frac{4\left(\lambda_m \cdot K + k_b\right)}{M} - \left(\frac{c}{M}\right)^2}. \tag{5.16}$$

Note that if $c = 0$ and $\sigma_m = 0$ then $G_{c=0} = G$ and Eq. (5.15) is identical to Eq. (5.12). Separating Eq. (5.15) into real and imaginary parts, we obtain

$$G_c = \cosh\left[\left(\sigma_m + \frac{c}{2M}\right)T\right]\cos(\omega_m T), \tag{5.17}$$

$$0 = \sinh\left[\left(\sigma_m + \frac{c}{2M}\right)T\right]\sin(\omega_m T). \tag{5.18}$$

If $|G_c| \leq 1$, then this equation will be satisfied if $\sigma_m = -c/(2M)$ and $\cos(\omega_m T) = G$ in which case the underlying solution is stable since $M > 0$, $c \geq 0$. This is not surprising: a stable solution in the undamped case remains stable in the presence of damping, but its Floquet exponents acquires a real part $-c/(2M)$. If $|G_c| > 1$, we must have that $\omega_m = j\pi/T$, where j is an integer and $G_c = (-1)^j \cosh\left[\left(\sigma_m + \frac{c}{2M}\right)T\right]$. The former equation simply implies that the imaginary part of the Floquet exponent is an integer multiple of half the modulation frequency (which is again consistent with what is known for general time-periodic modulated equations). The latter equation allows us to obtain an explicit expression for the real part of the Floquet exponent σ_m. Since $\sigma_m > 0$ implies instability, we arrive at the following condition for stability,

$$\left|G_c \operatorname{sech}\left(\frac{cT}{2M}\right)\right| \leq 1. \tag{5.19}$$

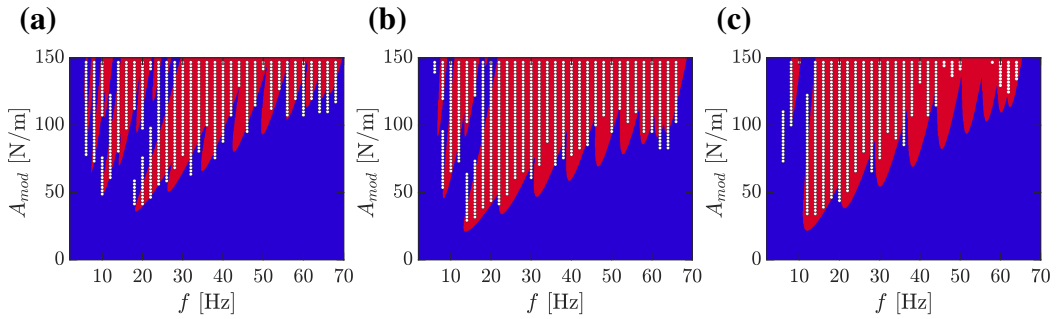

Figure 5.4: Stability diagram for $\tau = 0.3$ (a), $\tau = 0.5$ (b) and $\tau = 0.7$ (c) where red indicates instability and blue indicates stability. The white markers super-imposed on these panels are the parameter values where the experiment was observed to be unstable. A solution is considered unstable in the experimental set-up if an initially at rest lattice that is impacted on one boundary does not come to rest. If it does come to rest, it is called stable.

Thus, a solution that is unstable in the undamped case can be stabilized in the presence of damping. The precise amount of damping needed to stabilize the solution is given by Eq. (5.19).

With Eq. (5.19) in hand, we can easily determine stability in parameter space. We will fix all parameters other than the modulation frequency and amplitude. In Fig. 5.4 we show the stability diagram for $\tau = 0.3$ (a), $\tau = 0.5$ (b) and $\tau = 0.7$ (c) where red indicates instability and blue indicates stability. The white markers super-imposed on these panels are the parameter values where the experiment was observed to be unstable. A solution is considered unstable in the experimental set-up if an initially at rest lattice that is impacted on one boundary does not come to rest. If it does come to rest, it is called stable.

5.4 k-gap Breathers

In un-modulated lattices with periodic variation in the spatial proprieties of the lattice, it is well known that breathers can bifurcate from the edge of the linear spectrum [6]. The breathers become narrower and larger amplitude as the frequency goes deeper into the spectral gap.

To investigate a breathers in the wavenumber bandgap, we initialize Eq. (5.1) with a plane wave with wavenumber in the wavenumber bandgap. We start with a lattice of size $N = 300$, since there will be a large number of wavenumbers that fall into the gap. Fig. 5.5 shows an example of such a simulation. In panel (a), the time series of the velocity of the middle node $n = 150$ is shown. The pulse is localized is time.

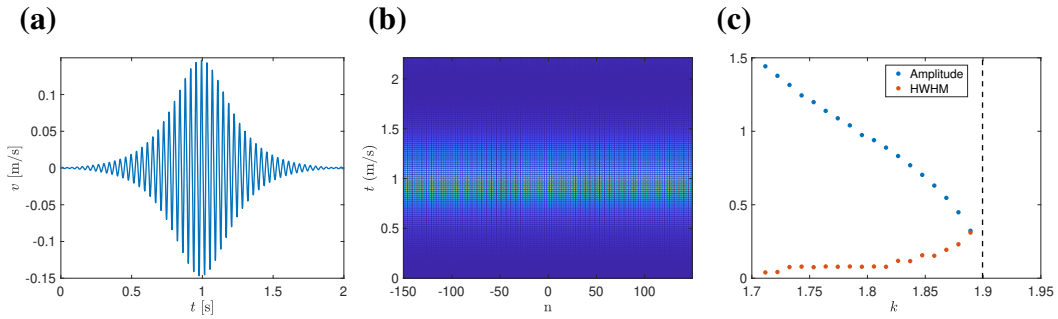

Figure 5.5: K-gap breather for $\tau = 0.5$, $A_{mod} = 150$, $f_{mod} = 52$ and $N = 300$ **(a)** Velocity profile of the middle node. **(b)** Intensity plot showing amplitude increases uniformly throughout the chain. **(c)** Plot of the amplitude (blue markers) and HWHM (red markers) of breathers bifurcating from the right band edge of the wavenumber bandgap. The vertical black dashed line is the edge of the bandgap.

In panel (b), an intensity plot is shown, where it is seen that the amplitude changes uniformly. The spatial periodicity of the solution is imposed by construction due to the finite length of the lattice with zero boundary conditions. This processes is continued for several wavenumbers in the bandgap (for these parameter values the gap is $q \in [1.35, 1.9]$). The amplitude is taken to be the maximuum velocity in the considered time domain, and width of the solution is measured to be half the width at half the maximuum of the solution (HWHM). As panel (c) shows, the wavenumber gap breather follows the same trend; the amplitude increases and becomes more narrow as wavenumbers deeper in the gap are selected. At some point, the breather becomes unstable ($q \approx 1.7$).

We now return to the lattice size relevant for the experiment, $N = 10$. In this case, there are only a few wavenumbers in the gap. Thus, to continue smoothly the breather as a wavenumber moves deeper into the gap, we fix the wavenumber but vary the modulation frequency so the relative position of the wavenumber in the gap will change. Here we pick $q_5 = 5\pi/11$. The results of this are shown in Fig. 5.6(a), starting with the f_{mod} at which q_5 is located at an upper band gap edge (shown as dashed line), and increasing the modulation frequency so that gap moves up relative q_5, until the breather solution is no longer found. We then add and increase the damping parameter, demonstrating that while the general trend of increasing amplitude remains, there is higher threshold of f_{mod} before breathers are observed.

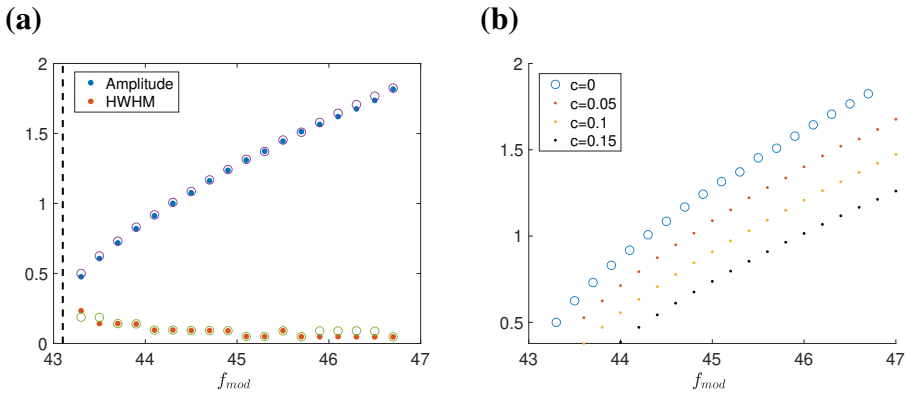

Figure 5.6: Same parameter set as previous figure, but with $A_{mod} = 140$. **(a)** Amplitude and HWHM while varying the modulation frequency and keeping the wavenumber fixed to $5\pi/11$. Plot compares the $N = 300$ (markers) and $N = 10$ lattice (open circles), showing the lattice size has minimal effect on the expected dynamics. **(b)** Amplitude varying the modulation frequency and keeping the wavenumber fixed to $5\pi/11$ with $N = 10$. Plot shows the effect of varying the damping constant c. While the amplitude decreases, as expected, the overall structure is preserved.

Experimental reconstruction

We search experimentally for breathers by initializing the time-periodic lattice with a single wavenumber and then observing the transient response. Since it not possible to prescribe the initial positions of the lattice at rest and then observe free oscillations in the modulated lattice, we approximate these initial conditions by driving lattice without modulation from one end with a monochromatic frequency corresponding to a wavenumber inside the band gap. Once a steady state is reached, the driving force is turned off as the time-periodic modulation is simultaneously turned on. Although this approach is imperfect, temporal solitons in an infinite medium have been shown previously to be generated by spatially localized input, so long as all wavenumber components of the input are located within the band gap [13].

We select a modulation amplitude of $k_b = 150$ N m^{-1} and $\tau = 0.5$ and select the the fifth eigenmode of the monatomic as the inital excitation of the lattice, corresponding to approximately $f = 19.7$ Hz. We use Eq. (5.19) to compute the range of f_{mod} for which the wavenumber of the fifth eigenmode $q_5 = 5\pi/11$ is located within the band gap, which is approximately $f_{mod} \in [44, 53]Hz$. The precise initial excitation is a 30-cycle sine burst of amplitude 0.3 N of lattice location $n = 2$, the end of which triggers the onset of the periodic modulation of amplitude 150 N m^{-1}. Sample velocity responses measured near the center of the lattice at location $n = 7$ are shown in Fig. 5.7.

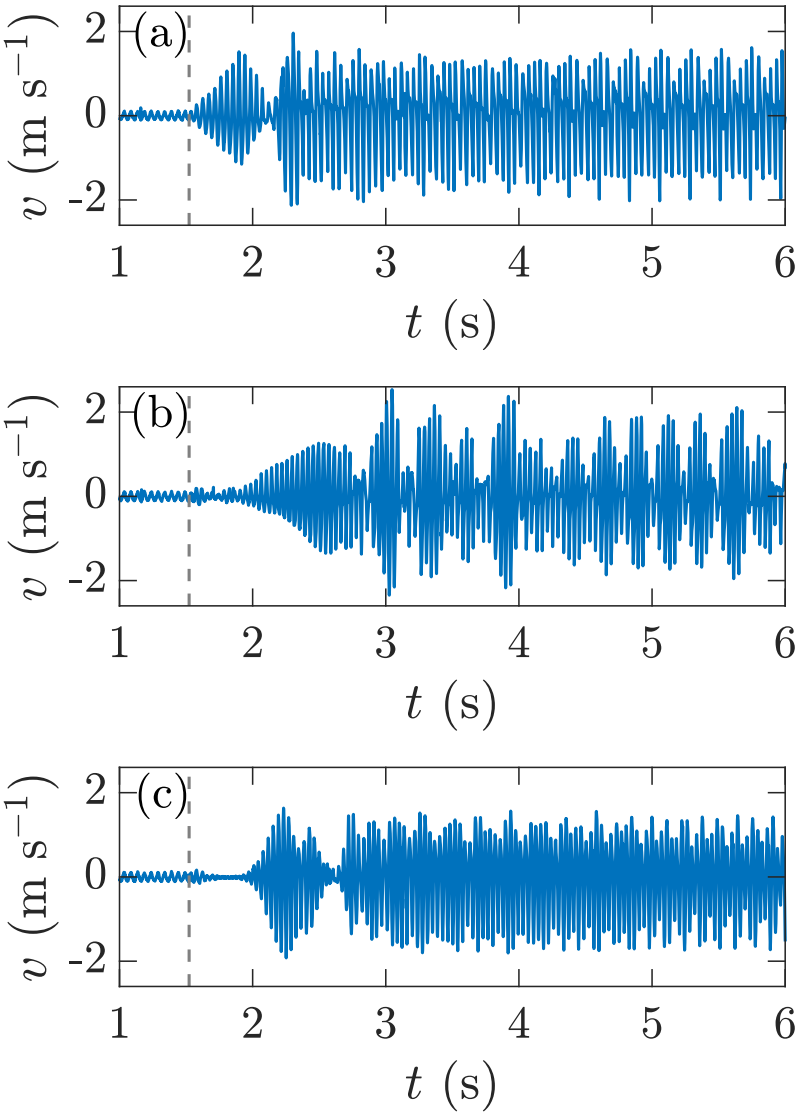

Figure 5.7: Velocity response of lattice location $n = 7$ with wavenumber q_5 initialized inside wavenumber band gap for modulation frequencies (a) $f_{mod} = 44$ Hz, (b) $f_{mod} = 50.2$ Hz, and (c) $f_{mod} = 52.8$ Hz. Gray dashed line indicated end of initial driving and onset of modulation.

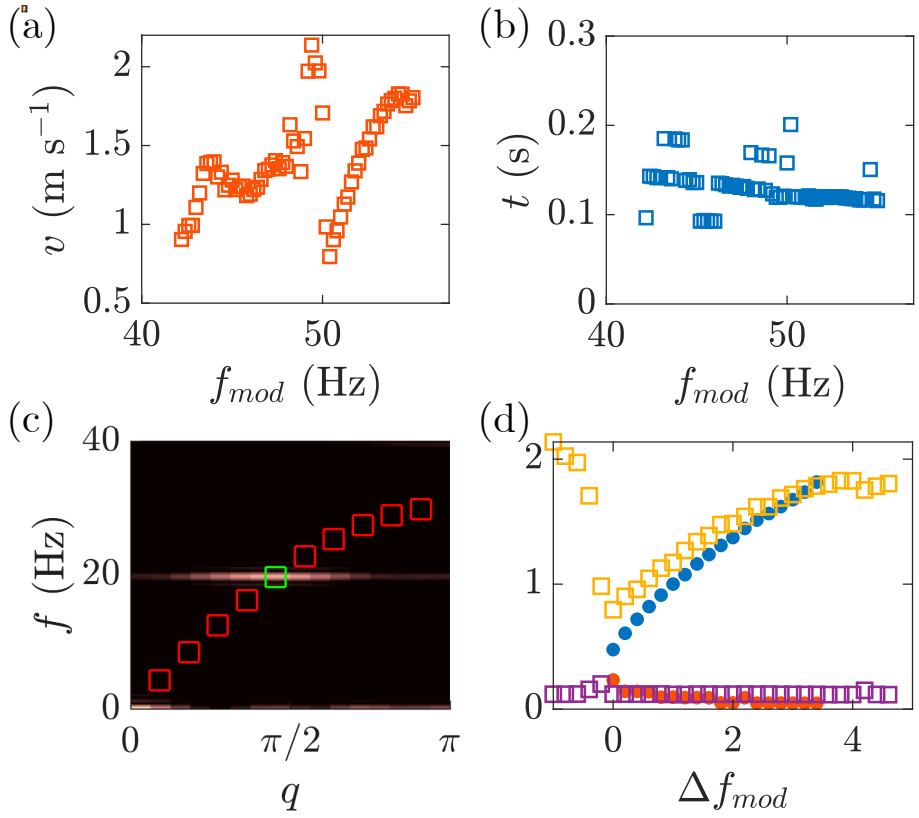

Figure 5.8: Characterization of breathers measured at location $n = 7$ with wavenumber q_5 initialized inside wavenumber band gap for modulation frequencies $f_{mod} \in [42, 55] Hz$. **(a)** Peak amplitude. **(b)** HWHM. **(c)** 2DFFT of input singal with eigenmodes labeled (squares) and target wavenumber highlighted green. **(d)** Comparison of simulation (squares) and measured (circles) amplitude (yellow, blue) and HWHM (purple, red) near an identified upper band.

It is observed in Fig. 5.7 that it is possible to observe temporally localized structures in the response of the lattice whether at the edges or within the analytically predicted band gap. The immediate response after the end of the initial wavenumber initialization typically exhibits the expected hyperbolic-secant-like envelope, growing in amplitude until reaching a maximum and then rapidly decaying. In a perfect system, this nonlinearity-induced transfer of energy between growing and decaying modes would repeat infinitely in time creating a train of identical pulses [13]. However, in the present system, we instead observe the emergence of a non-localized steady state solution, and we analyze the experimental breathers only before the transition to these other periodic modes.

We characterize these temporal breathers for the fifth mode for the full range of $f_{mod} \in [42, 55]$ Hz for which q_5 is inside the band gap. We measure the peak am-

plitude and the HWHM (see Fig. 5.8). Generally, the trend of increasing amplitude and decreasing HWHM is found in the experiments, but, interestingly, the very clear near-upper-band-edge behavior observed in the simulations at around $f_{mod} \approx 43$ Hz is seen in the simulations at $f_{mod} \approx 50$ Hz. We examine the 2DFFT of the monochromatic initial excitation in Fig. 5.8(d), observing that while the lattice response is centered at the desired wavenumber, the trace is relatively broad, and appears to encompass at least the nearest two. It is possible that the $f_{dr} = 19.7$ Hz initialization is exciting q_6 instead of q_5, and therefore we do not observe the near-upper-band-edge trends in amplitude and HWHM until a higher modulation frequency. This occurs around $f_{mod} \approx 50$ Hz, which is very near the analytical prediction of the intersection of q_6, $f_{mod} \approx 49.3$ Hz. We compare the simulation and experimentally measured breather amplitudes and HWHM relative to the locations of the identified band egdes, denoted Δf_{mod} (see Fig. 5.8(d)). Whether the discrepancy in band edge location stems the accuracy of the wavenumber initialization or other factors leading to differences between the predicted and real band locations, this comparison provides compelling evidence for the existence of wavenumber band gap breathers in this time-periodic nonlinear phononic lattice.

5.5 Summary and Conclusions

In this chapter, we developed analytical conditions for the stability of a temporally layered lattice, and validated them using numerical simulation and experiment. This linear stability analysis, as in Chapter 4, accurately captures the behavior of the real nonlinear lattice. We then presented an initial exploration of the existence of wavenumebr band gap breathers in the nonlinear lattice. While further theoretical development and experimental improvements are needed in future work, the results here provide strong qualitative evidence for the realization of breather or temporal soliton-like effects in phononic lattice systems.

References

[1] F. Biancalana, A. Amann, and E. P. O'Reilly. Gap solitons in spatiotemporal photonic crystals. *Physical Review A*, 77(1):011801, Jan. 2008. doi: 10.1103/PhysRevA.77.011801. URL https://link.aps.org/doi/10.1103/PhysRevA.77.011801.

[2] P. Binder, D. Abraimov, A. V. Ustinov, S. Flach, and Y. Zolotaryuk. Observation of breathers in Josephson ladders. *Physical Review Letters*, 84: 745–748, Jan. 2000. doi: 10.1103/PhysRevLett.84.745. URL https://link.aps.org/doi/10.1103/PhysRevLett.84.745.

[3] L. S. Cao, D. X. Qi, R. W. Peng, M. Wang, and P. Schmelcher. Phononic frequency combs through nonlinear resonances. *Physical Review Letters*, 112(7):075505, Feb. 2014. doi: 10.1103/PhysRevLett.112.075505. URL https://link.aps.org/doi/10.1103/PhysRevLett.112.075505.

[4] M. Centurion, M. A. Porter, Y. Pu, P. G. Kevrekidis, D. J. Frantzeskakis, and D. Psaltis. Modulational instability in nonlinearity-managed optical media. *Physical Review A*, 75:063804, June 2007. doi: 10.1103/PhysRevA.75.063804. URL https://link.aps.org/doi/10.1103/PhysRevA.75.063804.

[5] S. V. Dmitriev, E. A. Korznikova, Y. A. Baimova, and M. G. Velarde. Discrete breathers in crystals. *Physics-Uspekhi*, 59(5):446–461, May 2016. doi: 10.3367/ufne.2016.02.037729. URL https://doi.org/10.3367%2Fufne.2016.02.037729.

[6] S. Flach and A. V. Gorbach. Discrete breathers — Advances in theory and applications. *Physics Reports*, 467(1):1–116, 2008. ISSN 0370-1573. doi: https://doi.org/10.1016/j.physrep.2008.05.002. URL https://www.sciencedirect.com/science/article/pii/S0370157308001580.

[7] P. G. Kevrekidis. Non-linear waves in lattices: Past, present, future. *IMA Journal of Applied Mathematics*, 76(3):389–423, 2011. doi: 10.1093/imamat/hxr015.

[8] B. L. Kim, C. Chong, S. Hajarolasvadi, Y. Wang, and C. Daraio. Dynamics of time-modulated, nonlinear phononic lattices. *Physical Review E*, 107(3):034211, Mar. 2023. doi: 10.1103/PhysRevE.107.034211. URL https://link.aps.org/doi/10.1103/PhysRevE.107.034211.

[9] Y. S. Kivshar and G. Agrawal. *Optical Solitons: From Fibers to Photonic Crystals*. Academic Press, San Diego, 2003.

[10] F. Lederer, G. I. Stegeman, D. N. Christodoulides, G. Assanto, M. Segev, and Y. Silberberg. Discrete solitons in optics. *Physics Reports*, 463(1):1–126, 2008. ISSN 0370-1573. doi: https://doi.org/10.1016/j.physrep.2008.04.004. URL https://www.sciencedirect.com/science/article/pii/S0370157308001257.

[11] O. Morsch and M. Oberthaler. Dynamics of Bose-Einstein condensates in optical lattices. *Reviews of Modern Physics*, 78:179–215, Feb. 2006. doi: 10.1103/RevModPhys.78.179. URL https://link.aps.org/doi/10.1103/RevModPhys.78.179.

[12] A. H. Nayfeh and D. T. Mook. *Nonlinear Oscillations*. Wiley and Sons, Weihheim, Germany, 2004.

[13] Y. Pan, M.-I. Cohen, and M. Segev. Superluminal k-gap solitons in nonlinear photonic time-crystals, Aug. 2022. URL http://arxiv.org/abs/2208.09220. arXiv:2208.09220 [nlin, physics:physics, physics:quant-ph].

[14] M. Peyrard. Nonlinear dynamics and statistical physics of dna. *Nonlinearity*, 17(2):R1, Jan. 2004. doi: 10.1088/0951-7715/17/2/R01. URL https://dx.doi.org/10.1088/0951-7715/17/2/R01.

[15] E. Trías, J. J. Mazo, and T. P. Orlando. Discrete breathers in nonlinear lattices: Experimental detection in a Josephson array. *Physical Review Letters*, 84: 741–744, Jan. 2000. doi: 10.1103/PhysRevLett.84.741. URL https://link.aps.org/doi/10.1103/PhysRevLett.84.741.

[16] Y. Wang, B. Yousefzadeh, H. Chen, H. Nassar, G. Huang, and C. Daraio. Observation of nonreciprocal wave propagation in a dynamic phononic lattice. *Physical Review Letters*, 121(19):194301, Nov. 2018. ISSN 0031-9007, 1079-7114. doi: 10.1103/PhysRevLett.121.194301. URL http://arxiv.org/abs/1803.11503. arXiv: 1803.11503.

Chapter 6

SUMMARY AND FUTURE WORK

6.1 Summary

We have presented here several demonstrations of the fundamental physics of waves in time-varying and nonlinear media for acoustic waves in a discrete phononic lattice. While many of these concepts have been developed and implemented in the electromagnetic domain, we show the novel realization of phenomena such as temporal refraction and wavenumber band gap breathers in a system with time-varying elastic properties. In doing so, we shed light onto how acoustic and elastic analogs of electrical and optical systems provide opportunities as alternative platforms both for basic research and potential applications.

In Chapter 2, we introduce the experimental setup, which, owing to its discrete structure, is an excellent and adaptable platform for implementing time-variations in medium properties. More importantly, we show that our numerical model of the lattice captures the dynamics of the system with remarkable accuracy, making it an indispensable tool for experimental design and concept development.

In Chapter 3, we show the first experimental realization of the refraction of acoustic waves across a temporal boundary. Only recently has temporal refraction been demonstrated for electromagnetic waves [4, 6], and few examples of the refraction of mechanical waves exist [1], none of them acoustic waves. The concept of temporal refraction, or simply discontinuous temporal boundaries, lays a foundation for the understanding and design of time-varying systems beyond the already extraordinary broadband frequency conversion capabilities of the simplest case of a single boundary.

In Chapters 4 and 5, we focus on the dynamics of time-periodic media. First, we consider harmonic modulations, inspired by parametric amplification, but presenting the dynamics in the context of the opening of vertical wavenumber band gaps in the dispersion relation of the phononic lattice, which we are able to measure and reconstruct directly. We characterize stability of the modulation-driven states of the system, as well as their behavior in the presence of external driving. We investigate the nonlinear states in the context of classical nonlinear oscillations to further elucidate the behavior of the real lattice. Similarly, we consider the stability

of a temporally layered phononic lattice, whose solutions give us additional insight into stability, especially with respect to the excitation of wavenumbers inside the gap. Again, we then investigate nonlinear effects, this time focusing on temporally localized solutions, or breathers, permitted by the combination of nonlinearity and time-periodicity.

6.2 Future Work

Extension of experimental setup

Aside from the goal of improving the current experimental setup by reducing dissipation and increasing the length in order to improve observation, there are a number of possible pathways to explore new, more complex phenomena. In particular, one unique feature of the magnet and electromagnetic coil spring system is that the movement of a magnet axially through the coil induces a current, which could be utilized as input in a control loop, with feedback applied to the grounding stiffness of a magnet at a different location in the lattice. A time-varying transfer function may bridge back to some concepts explored here. More generally, if the velocity of a given mass is made to affect the grounding stiffness of another mass far away (i.e., not its nearest neighbor), and there are many of these interactions applied with spatial periodicity, it might be possible to observe exotic dynamics, such as anomalous dispersion, which has been demonstrated in periodic systems with long range interactions [2]. Such long range interactions via the coils could also easily be structured in time by a time-varying transfer function or amplification, allowing even more new dynamics could be observed.

Temporal boundaries

While appealing for their elegant simplicity and exact solvability, temporal boundaries are cannot be realized as perfect discontinuities in real systems; however, this should not be seen as a limitation. Some work has already shown that imperfect, non-sharp boundaries could potentially limit reflections [3, 5], and the study of arbitrary boundary profiles is a promising research direction for the lattice presented here, where arbitrary temporal variations are readily achievable. Beyond alternative temporal profiles, the highly dispersive nature of the discrete phononic lattice, especially in a state with the grounding stiffness turned "on," should be explored further in the context of slowing or trapping waves, with great potential for vibration or impact mitigation, along with signal processing. The application of strongly dis-

persive discrete time-varying to actively controlling the flow of energy in a system would be valuable in many contexts.

Nonlinear phononics

Finally, as we have shown, the nonlinear stiffness in the system from the magnetic repelling force offers a rich set of dynamics to explore, even without time variation. Multistability and switching, as demonstrated in the time-harmonic lattice, could be used in detection devices or memory components. Possibly the most exciting, however, is the potential for the further development of the wavenumber gap breather along the lines of an acoustic frequency comb, which could shed light on new dynamical phenomena and has significant potential for enabling the use of acoustic and phononic systems for high frequency applications.

References

[1] B. Apffel and E. Fort. Frequency conversion cascade by crossing multiple space and time interfaces. *Physical Review Letters*, 128(6):064501, Feb. 2022. ISSN 0031-9007, 1079-7114. doi: 10.1103/PhysRevLett.128.064501. URL https://link.aps.org/doi/10.1103/PhysRevLett.128.064501.

[2] Y. Chen, M. Kadic, and M. Wegener. Roton-like acoustical dispersion relations in 3D metamaterials. *Nature Communications*, 12(1):3278, June 2021. ISSN 2041-1723. doi: 10.1038/s41467-021-23574-2. URL https://www.nature.com/articles/s41467-021-23574-2.

[3] D. Kalluri and T. Huang. Longitudinal propagation in a magnetized time-varying plasma: Development of Green's function. *IEEE Transactions on Plasma Science*, 26(3):1022–1030, June 1998. ISSN 1939-9375. doi: 10.1109/27.700884.

[4] K. Lee, J. Son, J. Park, B. Kang, W. Jeon, F. Rotermund, and B. Min. Linear frequency conversion via sudden merging of meta-atoms in time-variant metasurfaces. *Nature Photonics*, 12(12):765–773, Dec. 2018. ISSN 1749-4893. doi: 10.1038/s41566-018-0259-4. URL http://www.nature.com/articles/s41566-018-0259-4.

[5] J. Zhang, W. R. Donaldson, and G. P. Agrawal. Impact of the boundary's sharpness on temporal reflection in dispersive media. *Optics Letters*, 46(16):4053, Aug. 2021. ISSN 0146-9592, 1539-4794. doi: 10.1364/OL.432180. URL https://www.osapublishing.org/abstract.cfm?URI=ol-46-16-4053.

[6] Y. Zhou, M. Z. Alam, M. Karimi, J. Upham, O. Reshef, C. Liu, A. E. Willner, and R. W. Boyd. Broadband frequency translation through time refraction

in an epsilon-near-zero material. *Nature Communications*, 11(1):2180, Dec. 2020. ISSN 2041-1723. doi: 10.1038/s41467-020-15682-2. URL http://www.nature.com/articles/s41467-020-15682-2.